The University Of Sheffield.

Raman analysis of tissue engineered normal skin and melanoma

By:
Ceyla Yorucu

A thesis submitted in partial fulfillment of the requirements for the degree of Doctor of Philosophy

The University of Sheffield
Faculty of Engineering
Department of Materials Engineering

Submission date:
August 2015

Dedication

This thesis is dedicated to my family.

Abstract

The usefulness of Raman spectroscopy for inspection of the human skin, engineered normal skin and melanoma models and the quality of its data for utilisation in dermatological research has been studied.

Raman signatures of human and tissue engineered normal skin (frozen and wax embedded) were investigated to determine if the layers have distinct spectral regions which can be used for identification, and for the monitoring of the formation of these layers in engineered human skin equivalents in culture. Several spectral regions, including those associated with lipids and some protein markers, were isolated and shown to be features that can be used to monitor skin maturation.

Raman signatures of engineered normal and melanoma models (frozen) were investigated to determine how the biochemical profile of melanoma tissue differs from engineered normal tissue which were used as a baseline. Changes were found in protein conformations and tryptophan configurations across the entire samples, in tyrosine and in more fluid lipid packing in tumour dense areas of melanoma, and in increases of glycogen content in the peri-tumour areas.

These findings suggest Raman spectroscopy may be helpful to theoretical and experimental research on melanoma progression and clinical treatments.

Acknowledgements

The author is indebted to:

Prof Sheila MacNeil and Dr Ihtesham ur Rehman for their supervision and guidance.

Chandra Talari and Salman Mian of the Spectroscopy group who constantly encouraged and motivated me during this PhD. Saad Qasim and Dr Vanessa Hearnden for their support.

Dr Shweta Mittar, Ahtasham Raza and Dr Nicola Green for their lab support.

Dr Katherine Lau of Renishaw Plc. for her continued support and practical advice both during and after my visits to their site. And everyone involved with my short project in their Raman division for their support.

David James of Thermo for his help and guidance with the Raman instruments in the KRI.

Dr Honza Pokorny for the pleasure of all RS related conversations.

The KRI Tissue Engineering Group and co-habitants of LG50 for making daily life pleasant.

The Instrument Loan Pool (EIP) for loaning out their Raman system and Dr Richard Brownsword for managing the process so efficiently.

The EPSRC and DTC TERM for the financial support which made this work possible.

Contents

List of Figures

List of Tables

Abbreviations

AA	Amino acid
ABCDE	Asymmetry, Border, Colour, Diameter and Elevation of lesion
AK	Actinic keratosis
ALI	Air Liquid Interface
ALM	Acral Lentigo Melanoma
BCC	Basal Cell Carcinoma
BM	Basement Membrane
BRAF	B-raf proto-oncogene, serine/threonine kinase
CA	Cluster Analysis
CARS	Coherent anti-Stokes Raman Scattering
CCD	Charge Coupled Device
DED	De-Epidermised Dermis
δ	Bending Vibrations
DMEM	Dulbeccos modified eagle's medium
DMSO	Dimethyl sulphoxide
DCS	Differential scanning calorimetry
EGF	Epidermal growth factor
EMEM	Eagle's modified essential medium
FCM	Fibroblast culture medium
FCS	Fetal calf serum
FT	Fourier Transform
FWHM	Full Width At Half Maximum
Glyc	Glycogen
H&E	Haemotoxylin & Eosin
HSE	Human Skin Equivalent
Hyp	Hydroxyproline

IDO	Indolamine 2,3-dioxygenase
IMS	Industrial methylated spirits
KCM	Keratinocyte culture medium
KIT	v-kit Hardy-Zuckerman 4 feline sarcoma viral oncogene homolog
LDA	Linear Discriminant analysis
LMM	Lentigo Maligna Melanoma
LWD	Long working distance
Melan-A	Melanocytic differentiation marker (Protein Melan-A)
MMP-2	Matrix metalloproteinase-2
MRI-MTC	Magnetization Transfer Contrast in Magnetic Resonance Imaging
MVA	Multivariate Analysis
NA	Nucleic acid
NIR	Near Infrared
NM	Nodular Melanoma
NRAS	neuroblastoma RAS viral (v-ras) oncogene homolog
OCT (Chapter 1)	Optical Coherence Tomography
OCT (Chapter 3)	(from OCT compound) Optimum Cutting Temperature
P16	Melanoma marker (cyclin-dependent kinase inhibitor 2A)
PBS	Phosphate Buffered Saline
PC	Principle Component
PCA	Principle Component Analysis
Phe	Phenylalanine
Pro	Proline
PK	Pigmented nevi
REACH	Registration, Evaluation, Authorisation of Chemicals
RGP	Radial Growth Phase
RS	Raman Spectroscopy
S-100	Melanoma marker
SC	Stratum Corneum
SCC	Squamous Cell Carcinoma
Si	Silicon
SK	Seborrheic keratosis
SNR	Signal to Noise Ratio
SRS	Stimulated Raman scattering

SSM	Superficial Spreading Melanoma
TDO	Tryptophan 2,3-dioxygenase
TGF-β	Transforming growth factor, beta 1
TE	Tissue Engineering
Trp	Tryptophan
Tyr	Tyrosine
TWL	Transepidermal Water Loss
υ	Stretching Vibrations
UV	Ultraviolet
UVN	Unit Vector Normalisation
VGP	Vertical Growth Phase
VIS	Visible
WHO	World Health Organisation

Chapter 1

Introduction

1.1 Background

Three dimensional skin tissue models were initially developed as substitutes to improve healing and restore the skin barrier in patients with full thickness burns. From a commercial point of view, the wound sector that it caters for is potentially very profitable. For the treatment of chronic wounds in Germany alone, a European Commision report suggested total annual sales to be in the region of 20 million euros in 2003, with a real market potential of at least six times this value [Hüsing, Bührlen, and Gaisser 2003]. However, from their initial development as substitutes for wounded tissue [Metcalfe and Ferguson 2007], application areas have since widened to testing of toxicity and drug formulations [Netzlaff et al. 2005, Zhang and Michniak-Kohn 2012] to modeling of various disease states such as eczamatous dermatitis [Engelhart et al. 2005] and skin cancer [Carlson et al. 2008, MacNeil 2007]. They have proved good experimental models for studying disease processes as their tissue architecture can mimic those seen in human skin more closely. They are used extensively to improve understanding of wound response through monitoring contraction and collagen production non invasively [Torkian et al. 2004] and study TGF-β function in re-epithelialisation [Garlick and Taichman 1994]. Techniques that can assess the quality of these products during culture, without the need of extensive sample preparation methods or that offer additional, new perspectives are vital for the expansion of this industry. Methods that assess tissue quality mostly either acquire morphological information (e.g. OCT, MRI-MTC) or render the samples non viable through chemical treatments or external labels (e.g. involucrin staining for keratinocyte differentiation status). It is proposed that assessing the molecular nature of the skin with Raman Spectroscopy (RS) may

provide complimentary information to many of the techniques commonly used in this area [Edwards, Williams, and Barry 1995].

1.1.1 Normal skin

Skin is the largest organ constituting 15-20% of the total body weight. Its primary function is to protect against environmental insults. It also possesses metabolic activity, delivers touch, heat and pain sensations via the peipheral nervous system, acts as a thermoregulator and excretes salts and wastes. Homeostasis is maintained through layers that have individual structures and functions, Figure 1.1.

Epidermis

The main function of the epidermis is protection against dehydration and invasion by bacteria and microorganisms. It also provides a degree protection against mechanical, thermal, chemical and UV insults. The zone itself is composed of five cell levels (strata) starting with the stratum corneum at the air/skin interface down to the basal level closest to the basement membrane (Figure 1.1). A fifth level, stratum lucidum, is found only in load-bearing sites such as the palms and soles, known as thick skin. All levels are predominantly composed of keratinocytes with melanocytes, langerhans cells and merkel cells dispersed to varying degrees through the keratinocyte network. A cell maturation gradient is observed within this zone. The basal level sees a continuous proliferation of cells that constantly move upward. The cells start to lose their nuclei and cytoplasmic organelles as they move up through the stratum spinosum and granulosum and finally become the anuclear, keratinized cells of the stratum corneum where they are routinely shed. The tissue turnover takes approximately 25-50 days.

Melanocytes only exist in the basal layer and have the primary function of producing melanin by utilizing tyrosine. Melanin gives colour to the skin, hair and iris of the eye. It is considered a photoprotective substance. Upon exposure to sunlight, it absorbs and transforms photon energy to heat leading to its dissipation. This process causes the pigment to either degrade, photoionize or produce free radicals [Ortonne 2002]. The protection is primarily from the UV range as its absorbing ability decreases exponentially from the UV to the visible range [Sarna and Swartz 1988]. Once produced, the pigments are deposited into the membrane-bound melanosomes and are taken up by keratinocytes, covering the nucleus and shielding it from UV radiation. Langerhan

cells are antigen presenting cells found in the stratum spinosum that facilitate skin allergic reactions. Merkel cells are mostly found in thick skin. These cells are attached to nerve endings and act as mechanoreceptors. Keratinocytes make up >90% of the cell population in the epidermis. They express the structural protein keratin and secrete lipid to form the primary barrier to the outside environment. At the stratum corneum level, the anucleated keratinocytes are embedded in a matrix of lipid by-layers, which act as a water sealant. These cells are also immunomodulators. They secrete inhibitory cytokines in the absence of injury while activating langerhans cells and triggering inflammation in the presence of injury.

Basement membrane

The basement membrane (BM) is a specialized extracellular matrix-protein complex in the form of a semi-permeable membrane. It acts as an anchorage matrix for epithelial cells that binds the epidermal and stromal zones. This boundary restricts transfer of cells and molecules. There is also some opinion that the matrix facilitates repair after injury by functioning as a scaffold for epithelial cells to migrate into. The zone is composed of three layers starting with the lamina lucida closest to the epidermis. An interim layer, lamina densa and the third fibroreticular layer closest to the stroma (Figure 1.1). The four major components of the BM are type IV collagen, laminin, entactin and perlecan. Type IV collagen and laminin are the most abundant proteins making up the matrix. They self assemble into suprastructures bridged with entactin and perlecan giving the protein matrix stability and structural integrity [LeBleu, MacDonald, and Kalluri 2007].

The lamina lucida is composed mostly of laminin. Basal cells are bound to it through focal points and hemidesmosomes. The lamina densa is composed of both laminin and type IV collagen while the fibroreticular layer is composed of anchoring fibrils based on type VII collagen that connect with type I collagen fibres in the dermis via anchoring plaques. Fibrillin microfilaments of the dermis extend to the lamina densa crossing the fibroreticular layer. The fibroreticular layer is composed of three different kinds of fibrous structures: anchoring fibrils, dermal microfibril bundles and collagen fibrils. The first are asymmetrically cross-bonded fibrillar components, which extend the lamina lucida at one end and the dermis at the dermal end, forming an interlocking meshwork. The dermal microfibril bundles pass deeply into the dermis perpendicular to the BM. Collagen fibrils are mostly randomly oriented with no junctional connection points.

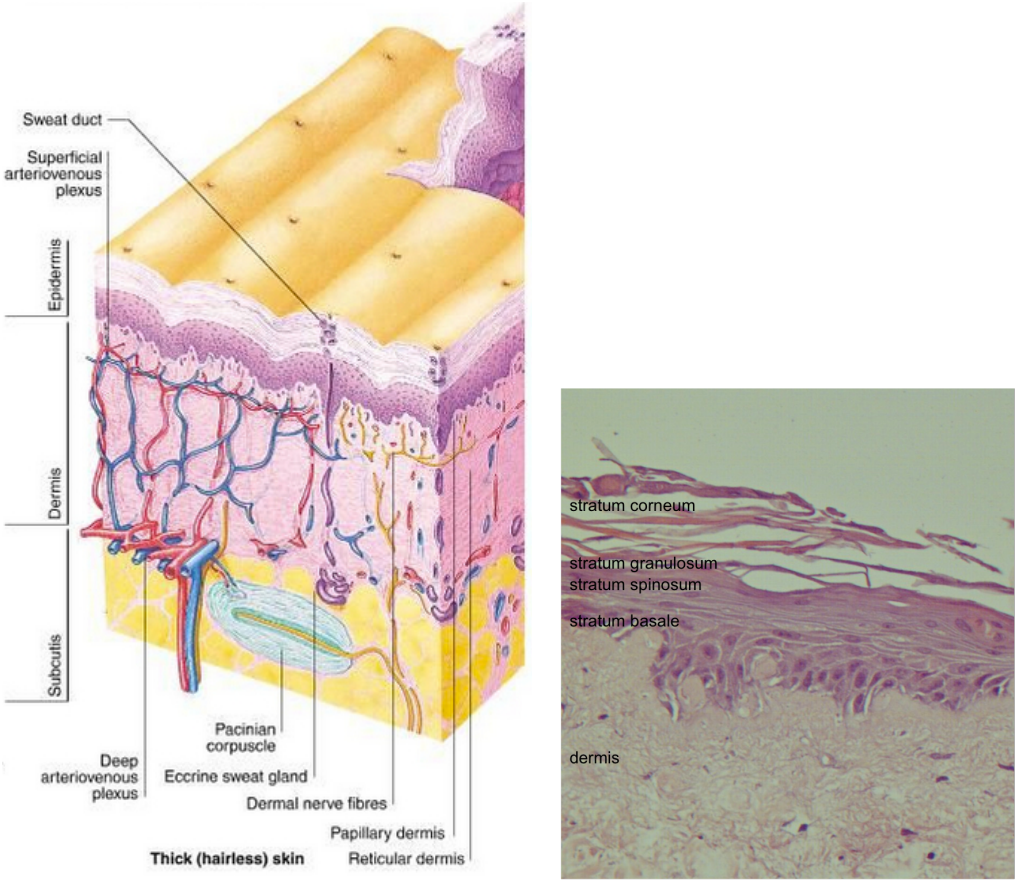

(a) Full-thickness skin diagram (b) H&E epidermis

Figure 1.1: (a) Skin components and structure (from [Gawkrodger and Ardern-Jones 2012) and (b) Epidermis of a tissue engineered skin stained with Haemotoxylin and Eosin.

Dermis

The dermis is the deepest zone of skin supporting the epidermis and gives it mechanical strength. It is an avascular matrix composed of collagen, elastin and proteoglycans. Housing blood and lymph vessels, hair follicles, sweat glands, sebaceous glands and nerve endings, it acts as a thermoregulatory control for the skin and allows sensations (touch, pressure, temperature, pain, etc.). The zone consists of two levels (Figure 1.1). The papillary dermis, closest to the basement membrane, is composed of loosely packed, thin, type III collagen fibres and few cells. Dermal papillae and nerve endings in this level supply nutrients to the epidermis. The reticular dermis is a denser network of closely packed type I collagen and elastin fibres in parallel arrangement to the skin surface. Hair follicles, sweat glands and sebaceous glands are found in this level. The primary cells of the dermis are; fibroblasts, macrophages and adipocytes.

The matrix acts as an active scaffold that helps define phenotypic differentiation of cells residing within it. Fibroblast cells produce interlacing collagen and elastin fibers that are housed in a glycosaminoglycan matrix. The glycosaminoglycans create a hydrated environment and give compressive strength to the matrix. This filling material plays a major role in cell-cell signalling and can enhance or inhibit signalling activity. The structural proteins, collagen and elastin, hold the dermis together. The blood vessels transport nutrients and oxygen to the avascular upper layers of the skin and deliver vitamin D to the rest of the body. Lymph vessels supply infection fighting cells of the immune system whilst sweat glands achieve temperature regulation by delivering water to the surface of the skin. Sebaceous glands secrete oils to waterproof the skin. And nerve endings house touch and pain receptors to transmit sensations.

Tissue engineered (TE) skin substitutes don't always try to mimic the entire skin structure seen in native skins. Instead, the construction varies by application. For toxicological testing, different skin cells are often seeded onto sheets of synthetic (e.g. polyglactin) or natural (e.g. collagen) polymers. For clinical use, they may be designed as single layers, such as dermis substitutes for chronic wound healing (INTEGRA®[Integra 2009]), up to split or full thickness skin grafts (StrataGraft®[StrataTech 2014]). Although they don't usually contain every native skin cell type, they can form appropriate barriers (for microbial defense and to prevent water loss) and even epidermal cell gradients close to native skin. They make good experimental models for diseases such as melanoma.

1.1.2 Melanoma

Incidence and mortality of melanoma is showing a marked increase in all countries [Stewart, Kleihues, Cancer, et al. 2003]. In the UK, incidence rates increased >250% between the years 1975-77 and 2006-08 [CancerResearch 2011]. This rise is higher than any other cancer and has made melanoma the fifth most common cancer in the UK [Globocan 2012]. Part of the increase is attributed to improved awareness, screening and diagnosis of the disease. Although the number of melanoma cases is small relative to the commonest cancer for each gender, incidence rates continue to increase, prognosis remains poor and it affects a young age group (Appendix). It is proposed that: (i) the spectral fingerprints of melanoma may aid in screening the disease and that (ii) Raman data may provide an additional perspective (different scale) in studying melanoma.

Etiology and Clinical features

Melanoma arises from cutaneous melanocytes found in the lower layer of the epidermis and may develop at any body site. The WHO recognizes ten subtypes based on their difference in clinical and pathological growth patterns (Appendix), four of which are considered major, Table 1.1. The subtype classification is not used as an independent prognostic attribute and does not currently affect clinical management decisions. Melanoma may arise de novo or within pre-existing melanocytic neavus [Longo et al. 2011]. Initial symptoms patients are likely to recognize are an increase in size of pre-existing moles or moles arising de novo with a surface area larger than normal. Particularly Superficial Spreading Melanomas (SSM), which grow considerably in size, and acquire irregularity in shape and colour. Acral Lentiginous Melanoma (ALM) presenting as a flat, pigmented lesion on the palm or sole and are more difficult diagnose. Initial symptoms for this type resemble those of an ulcer. Lentigo Maligna Melanoma (LMM) arises from precursor lesions resembling freckles and as such may also go unnoticed by patients. Rapid elevation of moles is a symptom favouring melanoma. This is commonly seen in Nodular Melanoma (NM) as they quickly enter Vertical Growth Phase (VGP). Histopathologically it is hard to discriminate between benign naevus and those of melanoma if developed within pre-existing benign melanocytic naevi. The reported percentage of melanoma cases arising from pre-existing benign naevi versus those occurring de novo vary considerably from 20-30% to 40-50% due to this [Weatherhead, Haniffa, and Lawrence 2007, Bishop et al. 2007]. Pre-existing scars including scars from previous biopsies may also be favourable to melanoma [LeBoit et al. 2006].

Both familial and environmental factors have an effect on melanoma etiology. The major risk factors are summarized in Table 1.2. Exposure to UV radiation is widely considered the major risk factor with an estimated 80% of all melanoma cases being attributed to sun damage to sensitive skin [Gandini et al. 2005b]. Causal pathways appear to be different for the major subtypes. Intermittent exposure particularly in childhood is a major determinant and the risk increases significantly if the individual has immune deficiency or genetic disposition. SSM and NM, the two most commonly diagnosed melanoma types more often present on intermittent sun exposed body sites and largely affect the under 50 age group. LMM presenting on the head and neck region is regularly linked to chronic sun exposure and is more common in the over 50 age group. It is postulated that familial traits alone, independent of environmental factors, may constitute up to 3-15% of melanoma cases [Dêbniak 2004]. And people with a large number of moles have a 10-fold risk of developing melanoma compared to those with few moles.

The clinical approach of detection from either origin is most commonly done through the application of the ABCDE rule and/or 7-point checklist. Uneven symmetry and pigmentation are the leading criteria. Not all melanomas will manifest every ABCDE feature. It is the combination of features that suggest cutaneous lesions most suspicious of melanoma [Rigel, Russak, and Friedman 2010]. The rule is shown to clinically diagnose melanoma with sensitivities between 47-82% [McGovern and Litaker 1992, Wolf et al. 1998, Ebell 2008]. However, the specificity is often much lower as many benign melanocytic naevi may also display such atypical features [LeBoit et al. 2006]. The exception to the rule is regressing tumours, which are observed as whitish, grey or black areas on the lesion. Many of the attributes highlighted by the ABCDE rule are shared by both benign naevi and melanoma. The features therefore have to be correlated with pathological findings and staged (see Appendix for melanoma staging).

Histopathological features I. Architectural

Proliferation of single melanocytes are seen in the earliest stages of melanoma. These cells aggregate and start forming clusters as the lesion diameter increases to around 2-3 mm [Fernandez and Helm 2004]. The most important architectural features are: (i) distribution of melanocytes, (ii) pigmentation, (iii) borders, (iv) confluence in nests and (v) inflammatory infiltrates. These mostly involve assessment of symmetry. Any

Table 1.1: Major subtypes of melanoma (recreated from [LeBoit et al. 2006] and [Bishop et al. 2007])

Subtype	Body site(s)	Growth	Risk groups	Prognosis
Lentigo Maligna Melanoma	Arises on continuously sun exposed sites. Most common in the head and neck region.	Growth is slow at first (may remain in situ for many years), then rapid once it acquires invasive capacity.	Most common in over 60s.	Relatively favourable, chance to diagnose before it becomes aggressive.
Superficial Spreading Melanoma	Arises on intermittently sun exposed body sites. Usually lower limb in women, trunk in men.	Growth is slow at first (lateral growth phase may develop for months), then becomes as aggressive as others of similar thickness.	Most common in young patients. 2/3 of all MMs diagnosed in caucasians.	Relatively favourable, chance to diagnose before it becomes aggressive.
Nodular Melanoma	Arises on intermittently sun exposed body sites. Usually head and neck region, lower limbs or trunk.	Growth is very rapid and vertical from the beginning and commonly develops ulceration.	Most common in older adults. It is the 2nd most common subtype of MM.	Most aggressive form of melanoma, very early detection necessary for favourable prognosis.
Acral Lentiginous Melanoma	On the soles, palms or under nails (thought to be unrelated to sun exposure).		Most common in older adults and heavily pigmented people. 80% of all MMs diagnosed in dark-skinned people.	Prognosis is poor, early detection necessary for favourable prognosis.

Table 1.2: Risk factors of melanoma (recreated from Gandini et al. 2005a, Gandini et al. 2005b, Gandini et al. 2005c, Marsden et al. 2010])

Familial and Environmental Risk Factors
Phenotypic pigmentation traits, e.g. fair complexion
Having clinically atypical or a large number of naevi
Having a history of blistering sunburns
Having a personal or family history of MM
Immunosuppression
Intermittent high-dose or chronic exposure to natural or artificial sunlight

asymmetry in the distribution of melanocytes, pigmentation and lesion borders favours melanoma. This includes whether or not the melanocytes are seen as single cells or nests and their density distribution within the lesion (all on one side of the lesion or scattered throughout). Pagetoid scatter for example usually suggests intraepidermal melanoma. Size and shape of nests in the dermis is also important as well as how they compare with nests in the epidermis. Apart from these, atypical mitotic figures (or ones that are in clusters) and distribution of infiltrates of lymphocytes have diagnostic importance.

Histopathological features II. Cytological

Melanocytes can vary greatly in size, shape and pigmentation between and within subtypes of melanoma. They may be large or small, highly pigmented, oval, spindle-like or dendritic in shape. Because of this, cytological features can be deceptive [McCarthy and Scolyer 2010]. For example, melanocytes found in the dermis of desmoplastic melanoma and epidermis of LMM are typically highly pigmented but large and pale in the epidermis of neavi of the scalp [Massi and LeBoit 2013]. Whereas dendritic melanocytes can be found in a number of different subtypes and skin colours. The width of dendrites may in some cases be indicative of melanoma. Some examples of histopathological features can be seen in Figure 1.2.

Markers

Melanoma markers are broadly divided into two groups: differentiation and progression markers. Differentiation markers identify cells of melanocytic lineage but can be common to benign melanocytic lesions as well as melanomas [LeBoit et al. 2006]. Examples

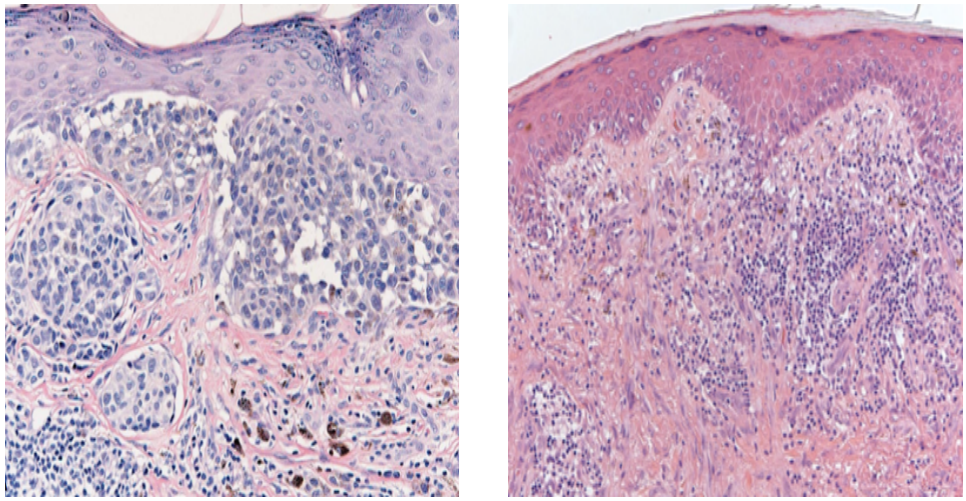

(a) (b)

Figure 1.2: Features of melanoma [LeBoit et al. 2006]. Architectural and cytological features of cells are different compared to normal skin H&E.

include the surface proteins Melan-A and S-100 which play a role in immune recognition. Progression markers identify various molecules involved in pathogenesis. Down or up regulation of their expression and their distribution are indicative of melanoma stage. They include a wide range of molecules associated with proliferation (e.g. p16), signalling (e.g. N-ras) or matrix degradation (e.g. MMP-2). A list of melanoma markers can be seen in Appendix.

Molecular features

Morphological classification of melanoma, in terms of its subtype, mainly defines the pattern of growth. It is considered to have little prognostic value as survival correlations using tumour thickness is much more accurate [Dickson and Gershenwald 2011, Wagner et al. 2003]. However, there is growing consensus that subtype may be correlated with somatic mutation. There are several such mutations identified in melanoma that disrupt downstream expression and activity of proteins that are typically involved with cell proliferation. Three of the classic oncogenes are BRAF, NRAS and KIT though many more are being studied that may be common to types with enhanced metastatic potential as well as subtype [Kunz 2014]. BRAF and NRAS mutations are found in approximately 70% of all melanomas (mutually exclusive) [Broekaert et al. 2010].

Progression

In the majority of melanoma cases, progression follows two stages before metastatic spread: radial growth phase (RGP) and vertical growth phase (VGP). RGP describes lateral expansion of the lesion. Growth is uneven but usually confined within the epidermis. Any atypical melanocytes in the dermis at this stage do not have proliferative capacity: they may survive without proliferating [Elder et al. 1983] or undergo apoptosis [Hsu et al. 1998]. In VGP, atypical cells in the dermis gain proliferative capacity and mitotic figures can be seen. Expanding clusters in the dermis are often larger than intraepidermal clusters. Metastasis is expected after this point. Typically, initial spread is to regional lymph nodes but it is not uncommon to see distant metastasis in other skin sites, lungs or liver in the absence of lymph node involvement.

Prognosis and Recurrence rates

There are several prognostic factors used in conjunction with clinical information, Table 1.3. Of these, ulceration, thickness and mitotic count are the major stage modifying attributes of melanoma up to stage III. Mitotic count largely affects stage I in the classification system and is a strong marker for survival because it indicates the tumours potential for metastasis [Clark et al. 1989]. At stage III, extent of lymph node invasion becomes the major stage modifying factor while the significance of thickness and ulceration decreases. Probability of 5-year survival is very different in patients that are sentinel node negative (90%) versus positive (56%) [Yee et al. 2005]. And after Stage III, the extent of metastases becomes the overriding factor. Significant recurrence rates are observed for all after Stage IB, Table 1.4.

Melanoma invasion in TE models shows some similarities to those seen in native skins. Depending on the type (aggressiveness) of the melanoma cells, the models may exhibit pagetoid scatter in the epidermis, form large tumour aggregates that show both RGP and VGP, or heavy dermal invasion. They are convenient alternatives to biopsies in preliminary studies for new analysis and imaging modalities such as Raman Spectroscopy.

Table 1.3: Prognostic factors of melanoma that need to be included in the histopathological report [Marsden et al. 2010]

Ulceration	Growth phase
Thickness	Regression
Mitotic count	Tumour-infiltrating lymphocytes
Histological subtype	Lymphatic or vascular invasion
Margins of excision	Perineural invasion
Pathological staging	Microsatellites

Table 1.4: Prognosis and recurrence rates for stages of melanoma (recreated from CancerResearch 2011, Marsden et al. 2010)

Stage	5-year survival	10-year survival	Recurrence rate
Stage 0	-	-	No risk reported after surgical excision
Stage 1A	95%	87-89%	<0.5mm has no recurrence
Stage IB	88-92%	78-85%	15-35% mostly within years 2-4
Stage IIA	77-79%	62-66%	15-35% mostly within years 2-4
Stage IIB	61-70%	49-57%	40-70% mostly within years 2-4
Stage IIC	43-47%	31-34%	40-70% mostly within years 2-4
Stage IIIA	57-73%	50-67%	High risk of further metastasis
Stage IIIB	41-57%	29-53%	High risk of further metastasis
Stage IIIC	20-34%	11-20%	High risk of further metastasis
Stage IV	5-22%	-	High risk of further metastasis

1.1.3 Raman Spectroscopy

Raman scattering

The classic model of spectroscopy considers a simple molecule as a harmonic oscillator. Attractive and repulsive forces are balanced in the equilibrium state. Monochromatic radiation (an oscillating electric field) propagates through the sample and exerts a force on the charges. The force deforms the bonds (the spring) pushing the molecule out of equilibrium and inducing an oscillating dipole moment. The Raman effect depends on the change in charge distribution that gives rise to the dipole moment, i.e. the molecules polarisability. The periodic deformations actuate vibrational and rotational transitions of the bond that vibrate at a characteristic frequency, exciting the molecule to a virtual state. A small fraction of photons interacting with the molecule (approx.

1 in 10^6–10^8) will experience an energy transfer and induce a change in the vibrational state of a molecule (Figure 1.3). Radiation emitted from such oscillating dipoles will be of different frequencies [Smekal 1923, Kramers and Heisenberg 1925, Landsberg 1928, Raman 1928].

1. Rayleigh Scattering: Most molecules will feel a restoring force and the displacement due to transitions will be fully recovered. The molecule returns to its original vibrational state after excitation. The frequency of emitted radiation remains unchanged from that of the incident ($v_{incident} = v_{laser}$).
2. Stokes Scattering: If energy is transferred from the photon, the bond displacement is not fully recovered and the molecule is restored to a higher vibrational state. The emitted photon is shifted to a lower frequency ($v_{stokes} = v_{incident}$-$v_{vib}$).
3. Anti-Stokes Scattering: If energy is transferred to the photon, a molecule in an already excited vibrational state is restored to a lower vibrational state. The emitted photon is shifted to a higher frequency ($v_{antistokes} = v_{incident}$+$v_{vib}$).

The intensity of Stokes lines are more intense than anti-Stokes lines as the population of molecules occupying a lower vibrational state will be higher according to the Boltzmann distribution [McCreery 2005]. Energy of each bond/bond group (spring) vibration is dictated by its vibrational force constant and will produce a characteristic shift in frequency. The force constant is dependent on molecular structure and its environment, e.g. atomic mass, geometry, organisation. The shift in frequency is represented by Δv and is termed the wavenumber. It gives the frequency of the scattered radiation relative to that of the incident. It is plotted as a function of intensity to give the Raman spectrum which is composed of all the Raman active bonds within the molecule under investigation.

Atoms in a molecule have a number of modes of vibration. Each mode requires different excitation energies and will thus produce different Raman lines. The number of vibrational modes of a molecule is given by:

$$Modes = 3N - 6 \tag{1.1}$$

Where N is the number of nuclei in the molecule and degrees of freedom for the molecule is 3N. Of these, three account for rotation and three (for non-linear) for translation. This gives an upper limit to the number of Raman lines for a given molecule as some modes may degenerate (have the same energy), may be Raman inactive (due to their

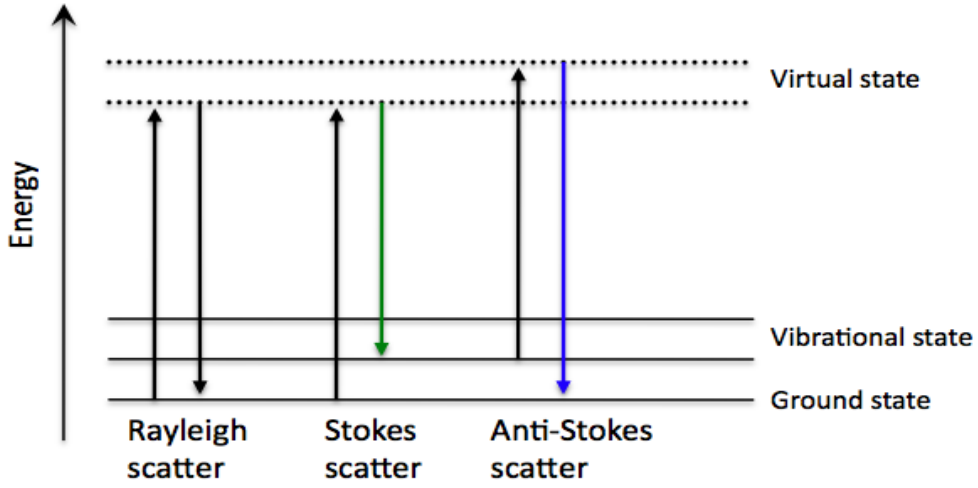

Figure 1.3: Schematic representation of scattering modes after excitation for a simple diatomic molecule: the harmonic oscillator model.

symmetry), or may not produce a line intense enough to be resolved from the background noise.

Consider Carbon Tetrachloride (CCl_4). It is a tetrahedral molecule with four bond pairs, each at a bond angle of 109.5 degrees to the central carbon atom. The molecule has nine normal modes of vibration, of which, only four are Raman active (Table 1.5). The symmetric stretch (1) is the most intense line as this bond has very high polarizability. In comparison, the scissoring (2) and rocking (4) vibrations have lower intensities due to lower vibrational force constants. And the asymmetric stretch (3) appears as a doublet with two maxima at 790.4 and 761.7 cm^{-1}.

Table 1.5: Raman active vibrational modes of CCl_4 and corresponding shift positions [Shimanouchi 1972]

	Vibrational Modes	Raman Lines (cm^{-1})
1	Symmetric stretch	458.7
2	Scissoring	217.0
3	Asymmetric stretch	790.4
3	Asymmetric stretch	761.7
4	Rock/Umbrella	313.5

Interpretation of the spectrum becomes harder with more complex molecules which can assume numerous conformations. For complex molecules, the use of mode frequencies may broadly be put into two categories. Those from localized motions reflecting functional groups (individual peaks) and those from bulk motions/properties, which may be associated to large unique molecules (fingerprint bands). The functional group frequencies may be used to find chemically specific information such as correlations between spectral features and molecular structures. E.g. The 458.7 cm^{-1} band of CCl_4 arises from the combination of C-Cl stretching vibrations. The band can be further resolved to display the ratio of Cl isotopes and give information on *submolecular* components (^{35}Cl or ^{37}Cl). The fingerprint band frequencies by comparison often inform the observer of larger scale properties such as chemical species. E.g. The four peaks that are intrinsic to CCl_4 and can be used to establish the presence of this *molecule* in a mixture.

The Raman effect is extremely weak compared to Rayleigh scattering. Its generation and detection requires monochromatic light sources and sensitive detectors to isolate the much weaker Raman lines from Rayleigh lines. There are two main instrument setups, CCD-based and FT-based. They differ in the way in which the Raman scatter is detected and analysed.

Instrumentation

CCD-based

A typical CCD-based dispersive spectrometer setup is shown in Figure 1.4. Laser light is directed onto the sample. All backscattered radiation is collected through the same path and returns to an optical filter.

Rayleigh scatter is much greater in intensity and will overwhelm the Raman signals if not filtered. Optical filters are used to selectively filter the Rayleigh line whilst allowing the weaker Raman scattered light through. There are two common types of filter used in RS:

- Edge Filters: These can be long or short band pass filters. The filter absorbs all wavelengths up to a specific point including the laser line and transmits all wavelengths above (or below) the threshold point. Anti-Stokes scattered light require short-pass filters, Stokes scattered light require long-pass filters. They

typically have steep edges that can get very close to the laser line.

- Notch Filters: These filters block absorption of a specific wavelength range and are used to absorb only the laser line. All wavelengths above and below the blocked range are transmitted allowing both Anti-Stokes and Stokes scattered light to be measured.

Raman spectrometers are typically setup with a range of lasers. Common laser wavelengths used are 514.5, 532, 633, 780, 785 and 1064 nm. Each laser requires an individual filter designed to block that particular wavelength.

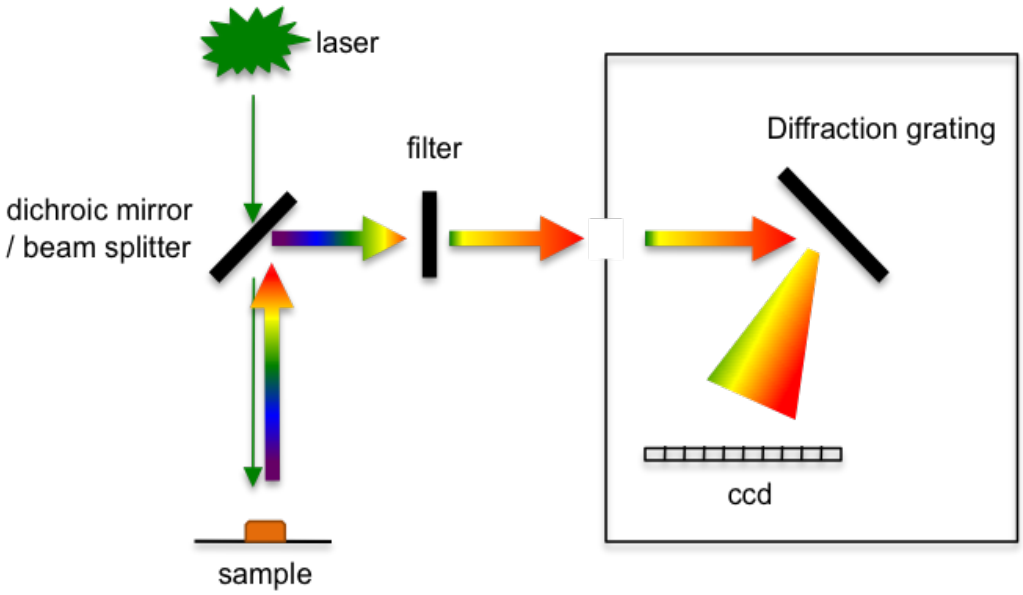

Figure 1.4: Simplified diagram of the main components of a Dispersive RS. This setup displays a system with a green laser and an edge filter collecting Stokes scattered light off the sample.

The Raman light transmitted through the optical filter is directed to a diffraction grating. This separates the Raman light into its composite wavelengths (each composite wavelength is scattered at a different angle), and onto the CCD. The gratings will typically range from 150 l/mm to 4000 l/mm. The CCD chips are two-dimensional arrays of light-sensitive elements (pixels). Each dispersed, composite wavelength is detected by a different pixel (group of pixels). Position and intensity translates into the Raman spectrum.

FT-based

FT-based Raman systems use an interferometer to produce an interferogram of the Raman scattered radiation. After excitation, a beam splitter divides the Raman scattered light into two paths. One travels to and from a fixed reference mirror. The other travels to and from a moving mirror. The two returning beams recombine and interfere constructively or destructively depending on their path lengths. The interference pattern is modulated by the polychromatic radiation. The resulting interferogram contains information about every frequency of the Raman scattered radiation and is transformed into a Raman spectrum. This type of spectrometer typically uses 1064 nm excitation. The longer wavelength excitation decreases the likelihood of sample fluorescence.

There are several practical reasons RS is an attractive technique for studying biological systems: (i) It does not require any dyes or probes so samples may be used for other purposes after RS analysis. (ii) It requires minimal sample preparation. Many of the tissue preparation methods used for other types of analysis can usually be adapted for RS analysis easily. (iii) Raman spectra are information-rich. The chemical fingerprint may be used to quantify multiple components of the sample using the same data set: potential for fewer tissue sections to measure several different components. (iv) It is also insensitive to water and can be coupled with fiber optic probes for remote and no-contact analysis. This is useful in skin analysis as it means data can be collected *in situ* from patients as well as from tissues in culture.

1.2 Aims

The aim of this project was to determine the potential value of Raman spectroscopy, specifically the type of quantitative and qualitative information that may be extracted from Raman analysis of 3D skin models and tissue engineered models of melanoma. Experimental objectives were as follows:

1. Determine the influence of different sampling methods of skin tissues on the Raman data obtained.

2. Determine the applicability of RS data for the identification and evaluation of the different layers of skin based on a study of intact skin and tissue engineered skin models.

3. Determine how useful RS data is in studying the interaction between melanoma cell lines and adjacent normal tissue using 3D tissue engineered models of melanoma.

Chapter 2

Literature Review

2.1 Introduction to the medical and biological applications of Raman Spectroscopy

A Raman spectrum is composed of all the Raman active bonds within a sample under investigation (Chapter 1). The spectrum is like a fingerprint which holds true for every identical sample under the same defined conditions. Changes to composition or in conditions that alter a physical property (e.g. crystallisation) result in changes to the spectrum as the type or environment of bonds change. Disease states, hydration/dehydration, trauma of the skin all cause changes to its biochemistry from normal state which are reflected in the spectra. To date, RS has been used to successfully differentiate tissues from different organ sites and a wide range of cancer types. Spectral differences between lung, liver and kidney tissues obtained from rats and pigs can be used to not only identify organ type but the species from which the samples were taken [Lorincz et al. 2004]. Lipid and protein content of breast tissues were found to be markers for benign and malignant states [Chowdary et al. 2006], keratin and tryptophan to be sensitive to separating normal and SCC tissues [Devpura et al. 2012] whereas differences to protein conformations and phospholipids were used to classify tissues of the stomach [Teh et al. 2008]. The applications are far-reaching and extensive due to flexibility in choices for sampling. Spectral features detectable in high resolution RS also offer information at the cellular level. Cells undergo specialized differentiation in order to perform specific functions, and produce specific biochemicals. B-cells secrete insulin, melanocytes produce melanin and neurons produce neurotransmitters. RS can be used to measure the different cell lines without the use of an external label and potentially, non invasively. It can be used to detect changes arising due to cell

differentiation [Swain and Stevens 2007], drug interactions [Owen et al. 2006] and as alternatives to conventional cell biology assays [Pascut et al. 2013, Pudlas et al. 2011]. The specificity of RS is also shown to be sensitive enough detect many cellular components within single cells. For example, the distribution of proteins [Uzunbajakava et al. 2003], lipid deposits [Wood et al. 2008] and organelles [Krafft et al. 2005].

2.2 Raman analysis of normal skin tissues

Raman bands corresponding to components of the skin have been assigned from studies using a variety of laser wavelengths and with skins that have been processed differently [Edwards, Williams, and Barry 1995, Barry, Edwards, and Williams 1992, Shim and Wilson 1996]. Spectra have been documented from sebaceous glands, nails, hair and sweat ducts [De Faria and De Souza 1999, Caspers et al. 1998]. It has potential in both extracting explicit information from the skin regarding molecular composition and using the spectra as highly specific fingerprints to identify or classify the tissue. For example, it has been used to detect changes in carotenoid concentrations in actinic keratosis [Hata et al. 2000] and to show that keratin is not structurally altered in hyperkeratotic conditions such as psoriatic plaques [Edwards, Williams, and Barry 1995]. Layers have been identified by comparing skin spectra at different depths to spectra collected from components that are known to be abundant in each layer. Lipids in the stratum corneum [Chrit et al. 2005, Gniadecka et al. 1998, Tfayli et al. 2013] and collagen in the dermis [Flach and Moore 2013, Ali et al. 2013c].

Lipids of the stratum corneum have been studied extensively with Raman spectroscopy. Lipid composition is important for SC function and regulation [Silva et al. 2006]. And the order of lipid packing determines SC permeability. Raman spectroscopy has been used to determine composition, such as the relative proportion of the major SC lipids: ceramides, cholesterol and fatty acids [Percot and Lafleur 2001]. Raman spectra of these components have also been studied under different experimental conditions that alter their lamellar structure. Lipid phase dependence on temperature has been shown both in mixtures [Wegener et al. 1996] and in mixtures supplemented with additives to lower phase transition temperatures [Neubert et al. 1997]. It is reported that relative population of trans and gauche phases can be determined as accurately as differential scanning calorimetry using the raman regions 3200-2800 (υCH_2) and 1150-1050 (υCC) cm^{-1}. A lateral packing value based on the (υCH_2) vibrations has been accepted and used for some time [Gaber and Peticolas 1977, Gniadecka et al. 1998]. The value is

based on the ratio of intensities for peaks at 2880 and 2840 cm^{-1} and produces a calibration chart from 0 (liquid state) to 1 (crystal state). Measurements of the lateral packing order gives an indication as to the barrier function of the SC and its capacity to prevent water loss.

Water content of the SC and underlying epithelial layers maintain SC flexibility and barrier properties. In this regard, water content is thought to be more important than oil content [Blank 1952]. As it has a direct effect on barrier function, water loss increases with skin damage. Transepidermal water loss (TWL) measurements are used in dermatological research to evaluate the rate of water loss, and by relation, barrier function. One of the most interesting applications of Raman spectroscopy on skin is the measurement of water profiles across skin layers. The ratio of the water band (-OH) at 3250 cm^{-1} to the overall protein band at 2930 cm^{-1} gives a value for the amount of water present per amount of protein. The method has been used to produce profiles for water concentration down to 250 μm below the skin surface [Caspers, Lucassen, and Puppels 2003, Caspers et al. 2001]. It shows water content to be low in the SC but much higher in the epidermis. Water holding properties of the viable epidermis is different enough to use this ratio to determine borders of the SC [Caspers, Lucassen, and Puppels 2003]. The same method has also been shown to measure water content of the dermal layers in patient forearms at up to 175 μm below the skin surface [Nakagawa, Matsumoto, and Sakai 2010], who detected higher amounts of dermal water in elderly patients. This sort of measurement is important in assessing skin conditions in patients (e.g. much greater water loss with eczema) but in particular, it has great potential in assessing new artificial skins and testing efficacy of new products to improve skin hydration.

Research into tracking various topical formulations into skin with Raman spectroscopy is also increasing. As the formulations are typically strong Raman scatterers, tracking their penetration has often been shown to be fast and reliable [Förster et al. 2011, Tosato et al. 2012]. A practical example is evaluation of the efficiency of delivery vehicles for trans-cinnamaldehyde which used their Raman signatures to trace their penetration into skin over time [Bonnist et al. 2011a]. Where Raman based values for the rate of transport were found to be quite accurate. Another study looked into conditions that increase absorption of toxic chemicals into skin [Broding et al. 2011]. This study monitored absorption of 2-butaxyethanol in water and ethanol on patients skins. Depth profiling approaches have also been compared to drug permeation into tissue sections to up to 50 μm depth [Tfayli, Piot, and Manfait 2008]. This type of study appears

currently to be limited to tracing products only. However, there is great potential in using Raman data to determine effects said formulations have on skin biology. Raman spectra are already being used to study changes to the composition of skin layers with some skin conditions such as hyerkeratotic psoriatic plaque [Edwards, Williams, and Barry 1995] and atopic dermatitis [O'Regan et al. 2010]. And the effects of external insults such as radiation damage from sun exposure. Radiation damage induced onto artificial skins have shown an increase in lipid signatures of the SC and protein damage early on followed with loss of DNA bands later [Ali et al. 2013a]. It is reported that the effects can be observed in Raman spectra at earlier time-frames compared to MTT assays.

2.3 Raman analysis of skin cancer

Skin cancer diagnosis and classification remains to be based on visual observations. Sensitivity and specificity of screening varies depending on the experience of the dermatologist. As it is subjective, excessive biopsies are taken in many cases. It is suggested that up to 80% of biopsies taken by non dermatologists turn out to be benign [Jones, Boiko, and Piepkorn 1996]. Histological classification, though very accurate, is intrusive, time consuming and requires expertise. RS has been recommended for the pre-selection of samples prior to excision, during surgery to ascertain tumour borders, and in studying localised effects around tumour borders *in vitro*. These altogether encompass both clinical (screening, diagnosis) and research areas of skin cancer making RS a potentially fruitful endeavour.

The commonest type of skin cancer is basal cell carcinoma (BCC) followed by squamous cell carcinoma (SCC). They account for approximately 75% and 20% of all reported skin cancer cases respectively [CancerResearch 2011]. BCC originates from keratinocytes, and typically grows slowly. It is not often associated with metastasis but it can cause local tissue damage if left untreated. Clinical diagnosis accuracy is only around 65% for practicing dermatologists [Gniadecka et al. 1997]. Several groups have shown various predictive classification methods can separate whether or not Raman spectra are collected from BCC or normal tissue. In these papers, BCC is identified with accuracies sometimes exceeding 90% both *in vivo* and *ex vivo*. Some major findings as to the origin of spectral differences and classification accuracies for BCC, SCC and normal tissues are presented in Tables 2.1, 2.2, 2.3, 2.4. Most of these studies report differences in the Amide bands and in the region 1000-600 cm^{-1}.

The skin cancer with the highest mortality rate is melanoma. Several groups have shown the Amide I band is reduced in intensity and broadened for melanoma samples. Changes to the amide bands in fact appear to be a common feature for most skin cancers and some benign conditions (Table 2.1). Authors mostly attribute spectral changes that are similar between for example normal to BCC and normal to melanoma to malignant transformations that are independent of tissue type. That the transformation is likely to trigger some similar molecular changes in tissues. But despite some similarities between different types of skin cancer spectra, BCC, SCC and melanoma, classification models setup for two or more of these types are able to discriminate malignant tissues from both normal tissue (quite accurately), and from each other (somewhat less accurately). For example, melanoma has been identified with a sensitivity 85% and specificity of 99% using neural networks in a data set collected from BCC, melanoma, seborrheic keratosis (SK) and normal skin [Gniadecka et al. 2004]. Differential diagnosis of melanoma has in fact been shown in several large data sets comprised of various skin lesions often confused with melanoma [Zhao et al. 2008, Lieber et al. 2008b]. And features from spectra of tissue components such as melanin, type I and III collagen, actin, triolein and nucleic acid DNA were also used to setup models in order to compare their sensitivity toward separating BCC, melanoma and normal tissue [Silveira et al. 2012]. Type III collagen and actin were found to perform well in separating BCC from both normal tissue and melanoma. Features of DNA were of higher intensity for BCC compared to normal tissue, and even higher for melanoma. This is expected in malignant transformation due to increased cell replication rates. The skin cancer studies also reveal differences in optical properties between cancerous and normal tissue. Cancerous lesions show much higher absorption and less scattering compared to normal skin [Rajaram et al. 2010, Fendel and Schrader 1998] and pigmentation is found to correlate with higher backgrounds but are reported to be easily handled [Philipsen et al. 2013].

Collection of Raman data from intact samples remains difficult but has greatly improved over the last decade. *In vivo* studies often lacked the higher SNR and resolution seen in spectra collected from fixed tissue sections before the advance in fiber optic probes. While they may still result in more intense processing of the spectra, tissue type differences in some cases, remain large enough for accurate and reliable classification. Raman spectra have previously been collected in vivo from lesions suspected of non melanoma skin cancer at depths of 40 μm below skin surfaces [Lieber et al. 2008a]. Where four types of tissue, SCC, BCC, scar tissue and normal tissue, were

correctly identified with an accuracy of 95% using only the Raman spectra. Interestingly, a punch biopsy was taken from each lesion after Raman measurements and it was noted that 40% of the lesions biopsied (as part of the treatment determined by the clinician) were actually scar tissue. Another study was able to discriminate BCC from surrounding tissue in vivo with similar accuracies using only the high wavenumber band of lipids between 2800 and 3100 cm^{-1} using LDA [Nijssen et al. 2007]. It is also suggested that this region may perform well in discriminating different cancer types [Gniadecka et al. 2004]. One large *in vivo* study included 518 samples of melanoma, BCC, SCC, actinic keratosis (AK), atypical nevi, melanocytic nevi, blue nevi and SK [Lui et al. 2012]. Skin cancers were separated from benign lesions with a sensitivity of 90% and specificity of 64%. Raman spectra were also used to accurately separate inflammatory skin conditions eczema and psoriatic skin from kaposi sarcoma [Fendel and Schrader 1998].

From a clinical point of view, apart from screening, accurate and reliable detection of tumour borders has significant impact on the success of treatment. Inaccurate determination of tumour borders causes high 5-year recurrence rates for primary BCC. This is reported to be as high as 10% with conventional surgery versus 1% with Mohs micrograph surgery [Rowe, Carroll, and Day 1989]. This type of surgery removes the tumour layer by layer whilst analysing each removed layer under a microscope simultaneously. Tumour margins are much more accurately determined compared to wide excisional surgery. There is increasing research into collecting Raman data from large areas to optically locate non-disease borders. Raman profile maps of BCC tissue sections have been shown to not only differentiate between normal and malignant areas [Baek et al. 2006, Choi et al. 2005] but also show that the spectra collected from dermis near tumour borders differ from the bulk dermis spectra [Nijssen et al. 2002, Nijssen et al. 2007]. The spectra reveal clear differences in the Amide I region, which shifts to a lower wavelength and becomes broader. Whilst the protein and lipid mode at 1454 cm^{-1} and Amide III regions are of much lower intensity for normal tissue. Cancer field effects have also been studied on tissue rafts. Dermal tissue on rafts seeded with fibroblasts and fibrosarcoma cells were found to differ in the vicinity of the tumour at 855 cm^{-1} (amino acid peak of tyrosine and proline) and in the Amide III band between 1340 and 1250 cm^{-1} [Lieber, Nethercott, and Kabeer 2010].

As for the use of RS in pure cancer research, the weakness lies in the inevitability of mode mixing as many tissue constituents have overlapping peaks/bands. RS can

detect C-C, C-N and C=O vibrations of all proteins within the tissue. The overlap of these vibrations for the large protein mix result in broad features and makes it difficult to identify individual proteins against a background of many other proteins. In tissue, the overall protein (or lipid, or DNA) contents are more often used to ascertain information on these species. For example, Amide I band between 1710-1620 cm^{-1}: the main contributor to the band is the C=O vibrations of protein peptide groups which represents the protein backbone geometry. For healthy normal tissue, in the absence of any external irritant, proteins are expected to have particular conformations and hence a specific Amide I position that represents normal function. In pathological tissue, expression of numerous proteins may be disrupted (upregulated, inhibited, etc.) or result in abnormal conformations. Changes in protein geometry or concentration will be reflected in this band (as shifts or changes to bandwidth etc.) allowing its detection. But, while an overall observation can be made of some change in protein products, it is very difficult to assign the change to an individual protein. Whilst many of the papers listed in Tables 2.1, 2.2, 2.3, 2.4 mention some change to the Amide I and III bands, conjectures about any reasons as to the cause of change is only moderately attempted. Raman spectroscopy papers handling skin cancer samples therefore appear to often focus on classification for screening purposes.

2.4 Emerging Raman techniques and their applications in life sciences

Stokes line intensity is proportional to laser intensity, and inversely proportional to excitation wavelength (I_{stokes} $1/\ \lambda^4$). Choosing a shorter wavelength increases Stokes line intensity, however, fluorescence is also wavelength dependent and typically increases with shorter wavelengths. This requires a trade-off between obtaining higher signal intensities at shorter wavelengths versus lower background at longer wavelengths. Sample concentration also has influence over line intensity. And choice of wavelength can change depending on factors such as sample thickness, phase, required measurement depth and the substrate on which the sampling is made. There are a number of emerging Raman setups that can increase line intensity using resonance effects.

For example, Resonance Raman Spectroscopy (RSS) occurs when the excitation frequency matches that of an electronic transition of an analyte. The transition increases the magnitude of the oscillating dipole moment. The resonance, when combined with

the freqeuncy of the laser generating the Raman signal, can result in line intensity increases in the order of 10^6 [McCreery 2005]. It is an alternative to **increasing concentration**. The method has been used to detect carotenoid concentrations in human skin stratum corneums non invasively [Ermakov et al. 2005]. Carotenoid levels were shown to correlate well with oxidative stress levels in subjects independent of dietary consumption. Haemoglobin oxygen saturation has also been measured in rats with deep violet excitation [Ward et al. 2007] and in single trapped blood cells [Gessner et al. 2004]. Interference from fluorescence is often a problem and may overwhelm the Raman signal making detection of the RRS signals over the background difficult for many samples. Also, the technique works only on spectral regions where the laser matches the appropriate electronic transition wavelength, limiting applicability (E.g. resonance of carotenoids closely matches 488nm excitation).

Surface Enhanced Raman Scattering (SERS) enhances Raman signals of analytes when they are absorbed onto or near the surface of certain noble metals. Collective oscillations of the conduction electrons (plasmons) move freely within the metal. The surface plasmons resonate upon excitation and are coupled with the energy of the incident radiation if the frequency of the excitation laser matches that of the plasmons. The effect is typically confined to local fields but the raman signals may be amplified by 10^3-10^7. It is an alternative to **increasing laser intensity**. The technique allows a wide range of inorganic and organic analytes, including single molecules, to be observed with much lower acquisition times and laser powers. It also greatly improves the detection limit of low concentration solutions. Classical Raman setup is able to detect Adenine in solution at down to 10^{-3} M concentrations, while with SERS the detection limit is increased to concentrations as low as 10^{-8} M [Kämmer et al. 2014]. Many groups have combined this technique to make use of the SERS enhancement in microfluidic devices to detect single cells and create rapid cell sorting assays for bacteria [Li et al. 2012]. SERS has also been used to create cellular pH maps within pH limits between 2 to 8, allowing the detection of cell reactions to external stimuli [Wang et al. 2008, Bishnoi et al. 2006]. Functionalizing the nanoparticles to detect specific molecules of interest is worth particular mention. The potential for combining substrate particles with various tumour-targeting antibodies is an exciting area gaining rapid interest. Oral cancer cells were found to align to gold nanorods containing antibodies targeting epidermal growth factor [Huang, Ernberg, and Kauffman 2009] and liver cancer cell were targeted with silver nanoparticles containing antibodies HER2 and CD10 [Kim et al. 2006]. The enhancement effect decays considerably with increasing distance form the metal surface,

which poses a limitation for this technique. Reproducing surfaces with identical states of aggregation and roughness is also difficult and requires highly controllable deposition methods. The typical metals used also photodecompose giving the produced substrate limited operational time.

Raman signals may also be enhanced via nonlinear excitation as seen in coherent anti-Stokes Raman scattering (CARS) and stimulated Raman scattering (SRS) that are beyond the scope of this review. Briefly; they involve a pump and Stokes laser that are incident on the sample. When the frequency difference between the pump and Stokes beams matches the Raman transition of a chemical bond, the molecular oscillations are coherently driven. In CARS, a second pump laser further interacts with the now excited chemical bond to give rise to an anti-Stokes signal several orders of magnitude greater than spontaneous Raman signals. In SRS, the enhancement arises from an energy transfer from the pump to the Stokes beam when the frequency difference matches a Raman transition. The techniques are chemically specific as only selected molecular vibrations are amplified. This brings some particular advantages including faster data acquisition (by focusing all energy to track a single bond) and also in cases where two components have Raman peaks in the same position, it may be possible to differentiate each component by shaping the pump pulse to each component. They have been used for video-rate imaging of tissues and to monitor drug delivery into skin [Saar et al. 2010, Belsey et al. 2014, Mansfield et al. 2013, Galli et al. 2014, Friedrich et al. 2015, Evans et al. 2005].

Table 2.1: Summary of RS-based findings from skin cancer papers

Author	Main features identified	Other significant	Number of samples	System
[Silveira et al. 2012]	800-1000 cm^{-1} and 1250-1300 cm^{-1} regions higher for BCC indicating higher protein content. 1620 cm^{-1} peak of haemoglobin lower for BCC.	ANOVA algorithm for classification was able differentiate BCC from normal tissue with sensitivity and specificity of 88% and 83% respectively.		830 nm laser up to 350 mW power
[Martin et al. 2004]	1200-1400 cm^{-1} Amide III band: 1270 cm^{-1} peak is lower for BCC, 1333 cm^{-1} peak is higher for BCC. 800-970 cm^{-1} band attributed to collagen, proline and hydroxyproline: shows general reduction in BCC.	Tissue type discrimination using PCA with sensitivity and specificities over 83%	21 x BCC sections, 18 x normal tissue sections	1064 nm laser, 300 mW power
[Nijssen et al. 2002]	Significant differences in lipid and nucleic acid content for BCC compared to dermis. Significant difference in DNA content for BCC compared to epidermis.	Raman mapping study. Performing KCA over the map clearly separated BCC from dermis. Classification sensitivity and specificity was 100%, 93% for BCC vs dermis. BCC vs epidermis was harder.	15 x BCC cryo sections	850 nm laser, 100 mW
[Lieber et al. 2008b]	1542-1556 cm^{-1} region for tryptophan, 807-821 cm^{-1} region (unassigned) and 758-772 cm^{-1} trytophan regions were considerably different between normal and bcc tissue.	This study was done in vivo!	21 suspect lesions, each	825 nm laser, 40 mW power

Table 2.2: Summary of RS-based findings from skin cancer papers *continued*

Author	Main spectral features identified	Other significant	Number of samples	System
[Gniadecka et al. 1997]	1680-1640 cm^{-1} Amide I band: 1650 cm^{-1} peak intensity is lower for BCC, this might indicate disturbance of α-helix structure. 1300-1230 cm^{-1} Amide III band: 1270 cm^{-1} peak is lower for BCC. Ratio of 1290-1220 cm^{-1} vs. 1360-1290 cm^{-1} peak areas are found to discriminate BCC from normal. 1000-800 cm^{-1} region: significant differences between BCC and normal. Ratio of 900-830 cm^{-1} vs. 990-900 cm^{-1} peak areas are found to discriminate BCC from normal. These peaks are attributed to proline, valine and polysaccarides.	ANN modelling over the 3500-400 cm^{-1} region confirmed visual observations.	16 x BCC sections, 16 x normal tissue sections	1064 nm laser, 300 mW power
[Choi et al. 2005, Baek et al. 2006]	1656cm^{-1} Amide I band is shifted to 1589 cm^{-1} for BCC 1302 cm^{-1} Amide III band is shifted to 1328 cm^{-1} for BCC. 1085 cm^{-1} phospholipid and nucleic acid peak is shifted to 1048 cm^{-1} for BCC. 1441 cm^{-1} lipid and protein peak is shifted to 1450 cm^{-1} for BCC.	Band shifts instead of intensities were used to discriminate tissue types with PCA, MAP, fuzzy and SVM. Discrimination accuracies were over 96%.	10x biopsies (Spectra for both BCC and normal skin were obtained from each biopsy)	514.5 nm laser 20mW power

Table 2.3: Summary of RS-based findings from skin cancer papers *continued*

Author	Main features identified	Other significant	Number of samples	System
[Pereira et al. 2004]	Amides I and III were significantly different between SCC and normal indicating changes to protein structure. 860, 939 cm^{-1} peaks higher in normal and assigned to collagen. Peaks associated with nucleic acids higher in SCC (1555-1560, 1244-1272 cm^{-1}.	-	8x intact SCC and normal skin samples	1064 nm laser, 200mW power
[Philipsen et al. 2013]	Looked at ratios: I_{3250}/I_{2930} - water bad higher in PN, BCC and MM. I_{1660}/I_{1450} - no significant difference. I_{1250}/I_{1450} - higher in normal compared to all. Ratio different enough for PN, BCC and MM to separate each. I_{1250}/I_{1310} - PN, MM >BCC.	This study was done in vivo. Also included classification. Sensitivity and specificity for: MM 93.3 and 96.4%. For BCC 88 and 85.5%. For PN 87.8 and 84.2%.	x55 normal, x25 BCC, x41 Pigmented nevi, x15 melanoma	1064 nm, 120 mW
[Fendel and Schrader 1998]	Collagen related bands lower, Histone, DNA, RNA bands higher in kaposi sarcoma. Higher lipid content in eczema samples.	Melanin fluorescence reported very high in melanoma.	Intact 9x eczema, 1x psoriatic skin, 4x kaposi sarcoma, 4x normal skin, ? melanoma samples.	1064nm, 300 mW power
[Lui et al. 2012]	Used PCA, LDA and PLS to separate i.skin cancers from benign lesions, ii.melanomas from non melanomas, iii.melanomas from non melanoma pigmented lesions. Found 1055-1800 cm^{-1} regions optimal for separating, iii. and 500-1800 cm^{-1} for separating cancer and precancers from normal.	Sensitivity and specificity for i, ii, iii varied from 90-99% to 15-68%.	In vivo study on 518 samples of melanoma, BCC, SCC, AK, nevi and SK	785 nm

Table 2.4: Summary of RS-based findings from skin cancer papers *continued*

Author	Main features identified	Other significant	Number of samples	System
[Gniadecka et al. 2004]	Amide I flattened for MM. Amide I and 1450 cm^{-1} protein bands shifted significantly in MM, BCC and SK but not in PN.	Neural network analysis on all samples. Sensitivity and specificity: For MM 85 and 99%, For BCC 97 and 98%, For SK 96 and 100%, For PN 78 and 97%. SK most commonly misdiagnosed with BCC.	x22 melanoma, x41 PN, x48 BCC, x23 SK, x89 normal.	1064nm, 300mW power
[Larraona-Puy et al. 2009]	788 cm^{-1} peak of DNA considerably higher for BCC (the intensity of this peak was also found to vary between epidermis and dermis lower in dermis-. Attributed to higher cell densities in BCC tissue.Significant difference in 1093 and 1350 cm^{-1} type I collagen peaks for BCC compared to dermis.	Raman maps of the tissue sections showed clear separation of epidermis, dermis, BCC and hair follicles.	20 micron tissue sections	785 nm laser power unknown
[Bodanese et al. 2012]	1271-1333 cm^{-1} Amide III/CH_3CH_2 twisting band: 1271 cm^{-1} peak is lower for BCC, 1333 cm^{-1} peak is higher for BCC. 800-1000 cm^{-1} region of C-C vibrations attributed to lipids and proteins: shows general reduction in intensity for BCC.	Tissue type discrimination power of two methods is compared. 1- PCA discrimination with sensitivity and specificities over 90%. 2- Biochemical model based discrimination on collagen content had sensitivity and specificities over 83%.	25 x BCC sections, 25 x normal tissue sections	830 nm laser, 80mW power

Chapter 3

Materials and Methods

The research described in this thesis has been carried out on fresh skin and engineered 3D models of normal skin and melanoma. Freshly isolated primary keratinocytes and fibroblasts were used to make up normal skin models. In addition to the normal skin cells, two melanoma cell lines were used to construct models for A375SM and C8161 type melanoma. The composites were set up sporadically over a 3 year period. Most of the normal skin cells were therefore cryopreserved in liquid nitrogen following isolation and expansion, then thawed as required. The melanoma cells were kindly donated by other staff in the laboratory who were expanding them, Ahtasham Raza and Shweta Mittar (see Section 3.1.2 for origin). The complete process for the construction of the models is depicted in Figure 3.1. All samples were fixed in formaldehyde and embedded in preservation media for subsequent histological investigation and Raman spectroscopic analysis. The method of processing depended on whether or not they were wax-embedded or cryo-embedded. The only exception to this was *in vivo* measurements on intact skin where an extra set of Raman measurements were carried out on fresh tissues (native or HSE) before formaldehyde fixation.

A full list of all cell and tissue culture consumables can bee seen in Appendix.

3.1 Cell and Tissue Culture

3.1.1 Fresh skin samples

Fresh skin samples were obtained during routine plastic surgery breast reductions and abdominoplasties from the Royal Hallamshire Hospital (Sheffield, UK). All skin samples were taken with written patient consent, for research purposes -only- and kept

anonymous. Samples were handled under the Human Tissue Authority (HTA) license 12179. The skin supply was split into three and used for: 1- Raman measurements on native human skin as is, 2- isolation of primary skin cells and 3- preparation of De-epidermised Dermis (DED). The skin samples for cell isolation and DED preparation were processed within 24 hours. Samples for native skin measurements were kept in PBS at 4°C until required.

3.1.2 Cell culture

All cell culture work was carried out in Class II Microbiology Safety Cabinets. The cabinets and surgical items used within were sterilised with 70% (v/v) Industrial Methylated Spirit (IMS) or by autoclave sterilisation. All cell culture media was warmed to 37°C in a water bath before use. All cell and tissue cultures were incubated at 37°C in humidified incubators with air containing 5% CO_2. Cells were always thawed from frozen, expanded in a flask and then added to composites. This was to ensure the cells seeded onto composites were all viable.

Passaging and storage

Passaging cells

Cells were passaged when they reached approximately 70-80% confluence to allow healthy proliferation to continue. To passage, cells were washed with PBS and detached using 0.1% (w/v) trypsin (keratinocytes were detached using 0.02% (w/v) EDTA followed by trypsin). The cells were suspended in cell culture media and spun down in a centrifuge at 1000 rpm for 5 minutes. The supernatant was discarded and the pellet was resuspended in cell culture media. A cell count was carried out using a haemocytometer and the appropriate number of cells were either: i. seeded onto composites, ii. passaged into new cell culture flasks, or iii. frozen down.

Freezing cells for cryopreservation

For cryopreservation, cells were treated as for passaging. After the cell count, the cell suspension was spun down again and the cellular pellet was resuspended into cryopreservation media. This media consists of 90% fetal calf serum (FCS) and 10% dimethyl sulphoxide (DMSO). The volume of cryopreservation media was made up so as to give a concentration between 2-3 million cells per ml of suspension. 1 ml of this suspension was pipetted into each cryovial and placed into a Nalgene Cryo freezing container. The container was placed in a -80°C freezer overnight. Cryovials were then transferred into

a liquid nitrogen dewar.

Thawing frozen cells
Cryovials were removed from liquid nitrogen and quickly thawed in the palms of the hand. The cells were diluted in cell culture media and centrifuged at 1200 rpm for 5 minutes. The supernatant was discarded and the cell pellet was resuspended in cell culture medium.

Human keratinocytes

Keratinocyte culture was carried out in Keratinocyte Culture Medium (KCM). This medium consists of Dulbecco's modified eagle's medium (DMEM) and Ham's F12 medium in a 3:1 ratio supplemented with 10% FCS, 5 ml glutamine, 5 ml Penicillin/Streptomycin solution, 1.25 ml fungizone, 2 ml adenine, 2.5 ml Insulin, 500 μl triiodotyronine, 80 μl hydrocortisone, 2.5 ml EGF and 500 μl cholera toxin.

Their isolation followed a previously described protocol [Eves 2001]. Briefly: split thickness skin grafts were obtained from theatres as previously described. Samples from this skin were cut into 0.5 cm^2 pieces using a scalpel blade and were incubated overnight at 4C in a universal with Difco Trypsin (DT). Skin pieces were then placed into a KCM containing petri dish and the epidermal layer from each piece was gently peeled off using a pair of forceps. A scalpel blade was used to gently scrape basal keratinocytes from the undersurface of the epidermis and from the papillary surface of the dermis. The de-cellularised epidermal parts were discarded and the de-cellularised dermal parts were put aside for fibroblast isolation. The cell suspension was transferred into a universal container and centrifuged at 1000 rpm for 5 min. The cells were resuspended in fresh KCM. 3-5(10^6) freshly isolated keratinocytes were seeded onto a feeder layer of irradiated 3T3 (i3T3) cells in a T-75 flask. They were incubated until approximately 80% confluent with a media change every 2-3 days. When passaging, the flasks were incubated in 0.02% (w/v) EDTA to detach i3T3s and then 0.1% (w/v) trypsin to detach keratinocytes. These cells were frozen down at passage 0 or 1 and only used to seed onto composites up to a maximum of passage 3. For composite experiments, they were suspended in KCM and seeded at a density of 3(10^5) cells per composite.

Human fibroblasts

Fibroblast culture was carried out in Fibroblast Culture Medium (FCM). This medium consists of DMEM supplemented with 10% FCS, 5 ml Penicillin/Streptomycin solution, 1.25 ml fungizone and 5 ml glutamine.

The dermal parts were collected as described in the previous section. These dermal samples were washed several times in PBS and then finely minced with a scalpel blade. The mince was incubated at 37C overnight in Collagenase A solution. The following day, the collagenase digest was spun down in a centrifuge at 1000 rpm for 10 minutes, the supernatant was discarded, and the pellet of cells was resuspended in FCM. Fibroblasts were seeded into T-25 flasks in the first instance and then T-75 flasks thereon. Cells were passaged when fibroblasts reached 80% confluence using 0.1% (w/v) trypsin. They were frozen down between passage 3 and 6 and seeded onto composites up to a maximum of passage 9. For composite experiments, they were suspended in FCM and seeded at a density of $1(10^5)$ cells per composite.

Human melanoma cells

A375SM

The A375SM cell line was obtained from Professor I J Fidler via M J Humphries (University of Manchester) [Eves 2001]. It is from lymph node metastasis of a 54 year old female. These cells were maintained in Eagle's modified essential medium (EMEM) supplemented with 10% FCS, 2uM l-glutamine, 100 IU/ml penicillin and 100 ug/ml streptomycin, 1.2 ugml(-1) fungi zone, 1.5% (100x stock) vitamin concentrate, 1mM sodium pyruvate, 10% non essential amino acids and 0.187% sodium bicarbonate at 37C. They were passaged using 0.1% (w/v) trypsin. For composite experiments, they were suspended in KCM and used at a density of $5(10^4)$ cells per composite.

C8161

The C8161 cell line was a gift from Professor F Meyskens via M Edwards (University of Glasgow) [Eves 2001]. It is from an abdominal wall metastasis from a woman with recurrent malignant melanoma. They were maintained in supplemented EMEM as for the A375M cell line. They were passaged using 0.1% (w/v) trypsin. For composite experiments, they were suspended in KCM and used at a density of $5(10^4)$ cells per composite.

3.1.3 Tissue culture

Preparation of De-epidermised dermis

Skin pieces approximately 1.5 cm^2 in size were cut using a surgical blade and immersed in 1M sodium chloride overnight at 37°C. The epidermis was then peeled away from the dermis using forceps. The piece of dermis left behind is referred to as DED. It is a structurally intact dermal component that retains basement membranes. For storage, the DED was washed in PBS several times and kept in KCM at 4°C until required.

Composite construction

The DED were prepared as described previously and placed into a six well culture plate with the papillary surface uppermost. Sterile stainless steel rings (0.8 cm inside diameter) were placed on top of each DED piece and gently pushed down to form a liquid tight seal between the ring and the DED. The well surrounding the ring was flooded with FCM, keeping the inside of the ring empty, and incubated for several hours to check a liquid tight seal had formed. Upon confirming a seal had formed, fibroblasts were added to the inside of each ring at a density of $1(10^5)$ cells per composite. The rings allowed a cell suspension volume of approximately 300 μl. After 24 hours of incubation at 37C, the FCM surrounding and within the ring was carefully removed. For melanoma models, melanoma cells suspended in KCM were added inside the ring at a density of $5(10^4)$ cells per composite. The well surrounding the ring was re-flooded with fresh KCM and the composites were incubated for a further 24 hours. On the third day, the media inside the ring was removed and replaced with keratinocytes at a density of $3(10^5)$ cells per composite. The media surrounding the ring was also replaced with fresh media. After another 24 hour incubation, the rings were removed and the composites were transferred onto stainless steel grids in a fresh six well culture plate. KCM was added into the wells so as to cover the edges of the grids where the bottom surface of the composite was in contact with media while the top surface was exposed to air. In this way the grids supported the composites at an air-liquid interface (ALI). The melanoma composites were then incubated at ALI for 14 days with a media exchange every 2-3 days. For normal skin models, keratinocytes were added following the first 24 hours incubation with fibroblasts. Normal composites were incubated at ALI for either 7 or 14 days. All completed models were fixed in 3.7% formaldehyde for a minimum of 24 hours before further processing.

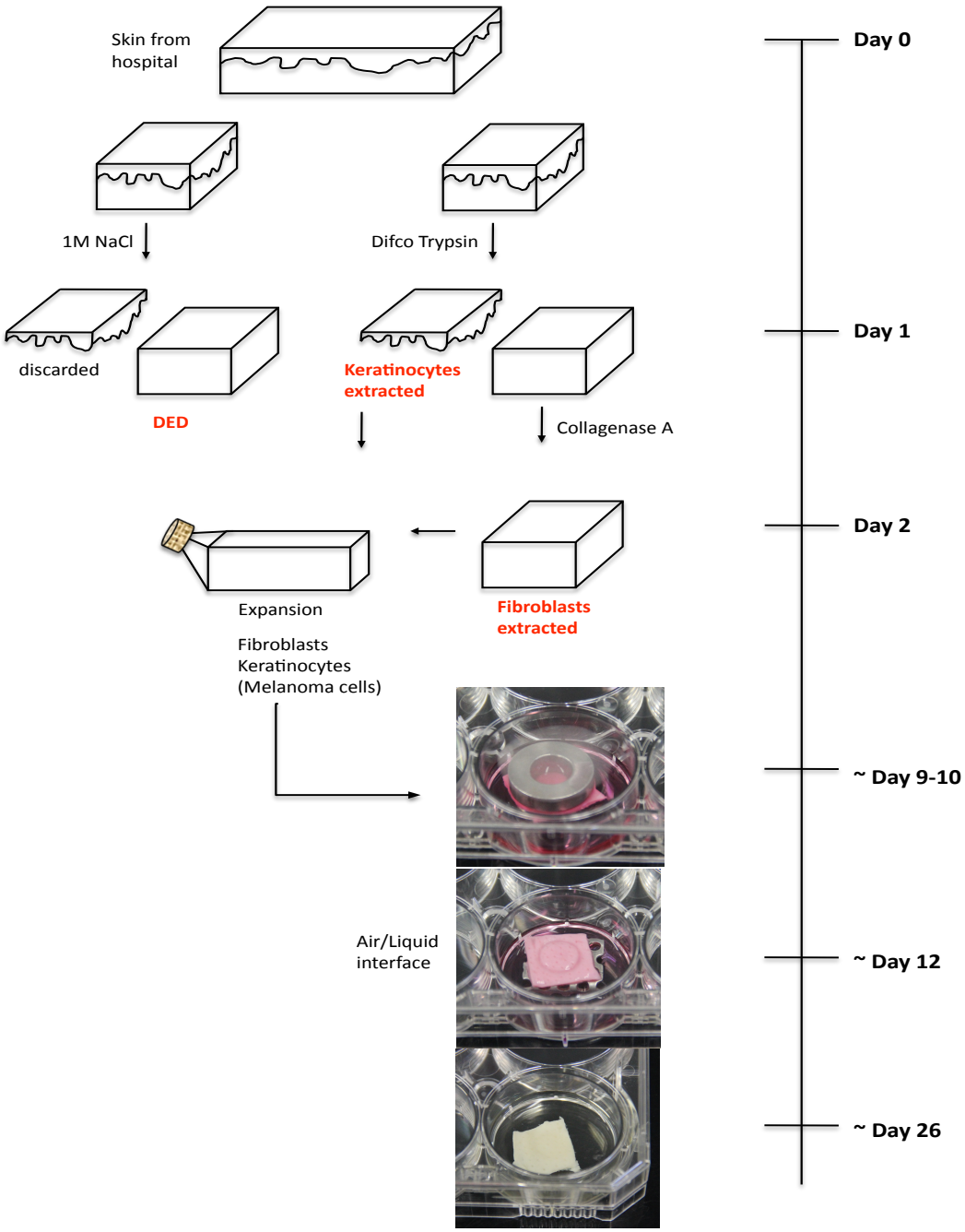

Figure 3.1: Diagram highlighting the steps of construction for tissue engineered skin models. It takes approximately one month to produce a skin model.

3.1.4 Preserving models

Wax embedding

Following fixation in formaldehyde, these samples were placed flat in tissue cassettes and processed overnight in a Leica TP1020 bench top tissue processor. The full list of solutions tissue is processed through can be seen in Appendix. Samples were then embedded in wax (Leica EG1160 embedding centre), cooled on ice blocks and stored at -20°C until required. 6-10 μm (H&E) and adjacent 10-25 μm (RS) thick sections were cut from each sample block using a microtome (Leica RM2145 microtome).

Cryo embedding

Following fixation in formaldehyde, samples were placed in 30% (w/v) sucrose in PBS for a minimum of two hours. The samples were then sandwiched between layers of Optimum cutting temperature (OCT) compound (Leica biosystems, UK) inside cryomoulds. The cryomoulds were gently lowered into a bath of liquid nitrogen. Once frozen through, the samples were stored at -80°C until required. A Leica cryostat (Leica CM1860 UV) was used to cut adjacent sections to a thickness of 6 μm onto glass slides for H&E staining, and to 20-25 μm onto either glass, quartz or CaF_2 for Raman analysis.

3.2 Tissue characterisation

3.2.1 Haemotoxylin and Eosin staining of tissue sections

All skin samples were stained with Haemotoxylin and Eosin. Paraffin embedded samples were washed in xylene and alcohol, followed by staining then repeat washes in reverse order. Cryo sections were first washed in PBS, stained and then dehydrated in alcohol. Full details of the staining steps can be seen in Appendix. Stained sections were allowed to dry for 10 minutes and sealed off with cover slips.

3.2.2 Sample preparation for Raman analysis

Intact skins

For Raman measurements on intact native skin, fresh skin samples from theatres were cut into 0.5-1 cm^2 pieces with a scalpel blade. The pieces were placed in a custom made stainless steel well block and enough PBS was added inside of the well so as to

keep the underside of the skin hydrated. A sapphire window of 2.5 cm diameter and 0.5 cm thickness (UQC Optics, UK) was used to seal off the well. The same procedure was also followed for some intact HSE measurements though approximately half of all HSE profiles were performed as is in their cell culture plates: Raman depth profile was collected with the lid off just before fixing in formaldehyde. 785 or 633 nm lasers and a x50 long working distance (LWD) objective (Olympus, N.A. 0.50) was used for all intact skin measurements. Collection times varied from 3x50 s per point to 1x60 s per point with total map times ranging from 120 minutes to 44 minutes. Typically three profiles were collected from three random locations on each skin sample.

Tissue sections

Data from tissue sections were collected using 532, 633 and 780 nm lasers and a 50x LWD objective. A 50-μm pinhole aperture was used for most of the data except for occasional thin sections (10 μm) which often benefitted from a 25-μm pinhole aperture. Collection times varied from a single 30 s exposure to 5x60 s exposures depending on sample, substrate and laser. For normal skin samples, spectra were collected from random points on each of the tissue layers: SC, epidermis and dermis. These layers were easy to identify on white light images and then confirmed from the adjacent H&E stained sections. On average, 5-10 spectra were collected from each layer of 2 to 3 sections of three samples. For melanoma samples, location of every sample point was recorded on the white light image of the sample area. These points were then compared to adjacent H&E stained sections to determine the corresponding tissue type/layer (e.g. tumourous or normal looking, melanoma invaded versus non invaded dermal components). Melanoma samples were divided into areas of different categories (Chapter 6) with a minimum of 30 spectra collected from each area.

3.2.3 Raman instruments

Instrument 1: Thermo DXR Raman Microscope equipped with a 532 nm diode laser, a 633 nm HeNe laser and 780 nm diode laser. Spectral resolution was 6 cm^{-1} for each laser setup.

Instrument 2 (EIP Loan Pool): Renishaw InVia Raman Microscope equipped with a 785 nm diode laser. Spectrometer aperture was set to 64 μm. The grating was 1200 lines/mm producing a reported maximum spectral resolution of up to 2 cm^{-1}.

3.2.4 Processing and Analysis of Raman data

Substrate subtraction, fluorescence correction and peak position measurements were done on OMNIC and TQ Analyst (Thermo, U.S.A.). Substrate spectra were subtracted from almost 90% of the sample spectra collected from tissue sections on glass and quartz. Polynomials were subtracted from all spectra collected with the 633 nm laser (Chapter 5, Section 5.2.2) to correct for baseline distortions. Degree of the polynomial used varied from 3 to 6. Peak positions were measured as the position of maximum height of a peak within a defined range (e.g. Max height in the range 1520-1360 cm^{-1} gives Amide II position.).

Unscrambler X (CAMO, Sweden) was used for the MVA methods Cluster Analysis (CA), Principle Component Analysis (PCA) and Linear Discriminant Analysis (LDA). The data were first baseline corrected and Unit Vector Normalised (UVN). Wards method of clustering was used for CA. This method computes the difference between (i) each sample in a group and (ii) between each sample to the groups centroid. The parameters for PCA setups varied. Every PCA was setup with a minimum of 12 orthogonal variables depending on the spectral region used, where the number of PCs chosen for each setup described >99% of the variation. All LDA models were setup over the full spectral range. In each LDA, five random spectra from the data set were left out of the training models at each run. Each set of five -unlabelled- random spectra were tested against the corresponding training model until 20 such spectra were tested. Model sensitivity and specificity were calculated by comparing predicted class to the official class obtained through H&E staining.

Peak height measurements were done on OriginPro (OriginLab), TQAnalyst (Thermo, U.S.A.) and WIRE (Renishaw, UK). Measurement of Phenylalanine intensity was done on OriginPro. Spectra were normalised to Amide I, one peak was fitted to a fixed position of 1002 cm^{-1}, and height was measured from the baseline. Signal loss versus depth for intact skin was presented as the percentage loss from the maximum intensity point (Chapter 4). Height measurements of the high wavenumber region (3200-2600 cm^{-1}) of tissue sections were performed on TQAnalyst. WIRE or OriginPro was used for intact skins. For tissue sections, the height of peaks at the fixed locations of 2930, 2880 and 2840 cm^{-1} were measured from the baseline. Charts that track the protein to lipid content in sectioned skin layers (Chapter 5, Section 5.2.1) use these measures. For intact skins, 5 peaks were fitted to this band (fixed centres at 3047, 2980, 2930,

2880 and 2840 cm^{-1}). Lipid profiles through intact skin layers (Chapter 5, Section 5.2.2) use the intensities of these component bands. OriginPro was used to measure the intensity of the Tryptophan doublet (Chapter 6, Section 6.2.3). This was done by fitting two peaks with fixed centres representing the 1360 and 1340 cm^{-1} peaks to the first derivative spectra.

Chapter 4

Raman Spectroscopy methods

4.1 Introduction

Comprehensive guides for using RS on skin tissues are not available. Many sample preparation details such as preferred substrates or tissue preservation methods are passed on within research groups as know-how. This is not altogether unexpected as many of the tissue preparation methods are sample and application specific. For example, dewaxing medium and times are not the same across samples or groups. Dewaxing efficiency can be different on even tissues of the same type: brain tissue containing tumour retains more wax than normal brain tissue with the identical dewaxing protocol [Fullwood et al. 2014]. It is important to understand the effects these procedures have on Raman signatures because research using a very wide-range of protocols are referred to for the assignment and interpretation of peaks. It is also often much easier to make changes to the sampling aspects in order to make data collection more straightforward instead of extensive data processing afterwards. Whilst the following results chapters deal with collected information, this chapter outlines the effects of some skin sampling methods on data collection and processing.

4.2 Results

4.2.1 Backing substrates for tissue sections

All HSEs in this thesis were constructed using DED scaffolds made with excess skin from surgeries or cadaveric skin. The use of these scaffolds means either a reliance on hospitals which can be infrequent/unreliable or that great expenses are amassed buying cadaveric skin from the euroskin bank. It restricts the number and size of HSEs

produced and make the samples valuable. This often constrains the thickness to which samples may be practically sectioned (<20 μm). Thin sections are practicable also, because it keeps Xylene washes to manageable time-scales for wax-embedded samples and allows cryo-embedded samples to dry more uniformly. At unit thicknesses of 20 μm or less, it is important that backing substrates for the sections do not have intense Raman signals that will interfere with tissue signals. Figure 4.1 shows the Raman spectra of some commonly used substrates across three wavelengths.

Several substrates produce Raman bands in regions overlapping tissue peaks, Table 4.1. CaF_2 and MgF_2 slides seem ideal as: i. their respective peaks at 320 and 405 cm^{-1} can easily be truncated with no effect to the integrity of tissue data and ii. the peaks are consistent for all wavelengths. Quartz slides have a particular signature that is also consistent for all three wavelengths but it spans across a large spectral range from around 900 to 200 cm^{-1} and overlaps tissue regions. Stainless steel slides by comparison do not feature prominent bands but the largest baseline offset is observed with these slides. Glass slides produce intense and broad bands that interfere with large portions of tissue signals with all wavelengths. This makes substrate choice a limiting factor for the Raman analysis of tissue sections. The extent of this limitation will theoretically be minimal as long as tissue thickness exceeds the axial resolution of the setup: either by increasing section thickness or by using higher N.A. objectives. Axial resolution of a typical setup with 50x lwd objective often used in this thesis is shown in Figure 4.2. Where depth of collection volume at any given point is approximately 20 μm. This volume is reported to be 7.5 μm with a 50x objective and 25-μm pinhole aperture. For the 50x objective, tissue thicknesses as low as 10 μm may therefore be supported without substrate interference. But this does not always hold true. There are two factors to note. In the first instance, skin tissue is more similar to fabric than to opaque matter. Scattering effects often make substrates raman visible. Secondly, the SC, epidermis and dermis are structurally different with regards density of packing. Spectra from the keratinized SC layers may not show any signs of substrate backgrounds even at <10μm thickness, whereas it is difficult to eliminate substrate background from the epidermis and dermis at the same thickness. This difference between the layers also cause them to dry at different rates leading to a rough surface topography.

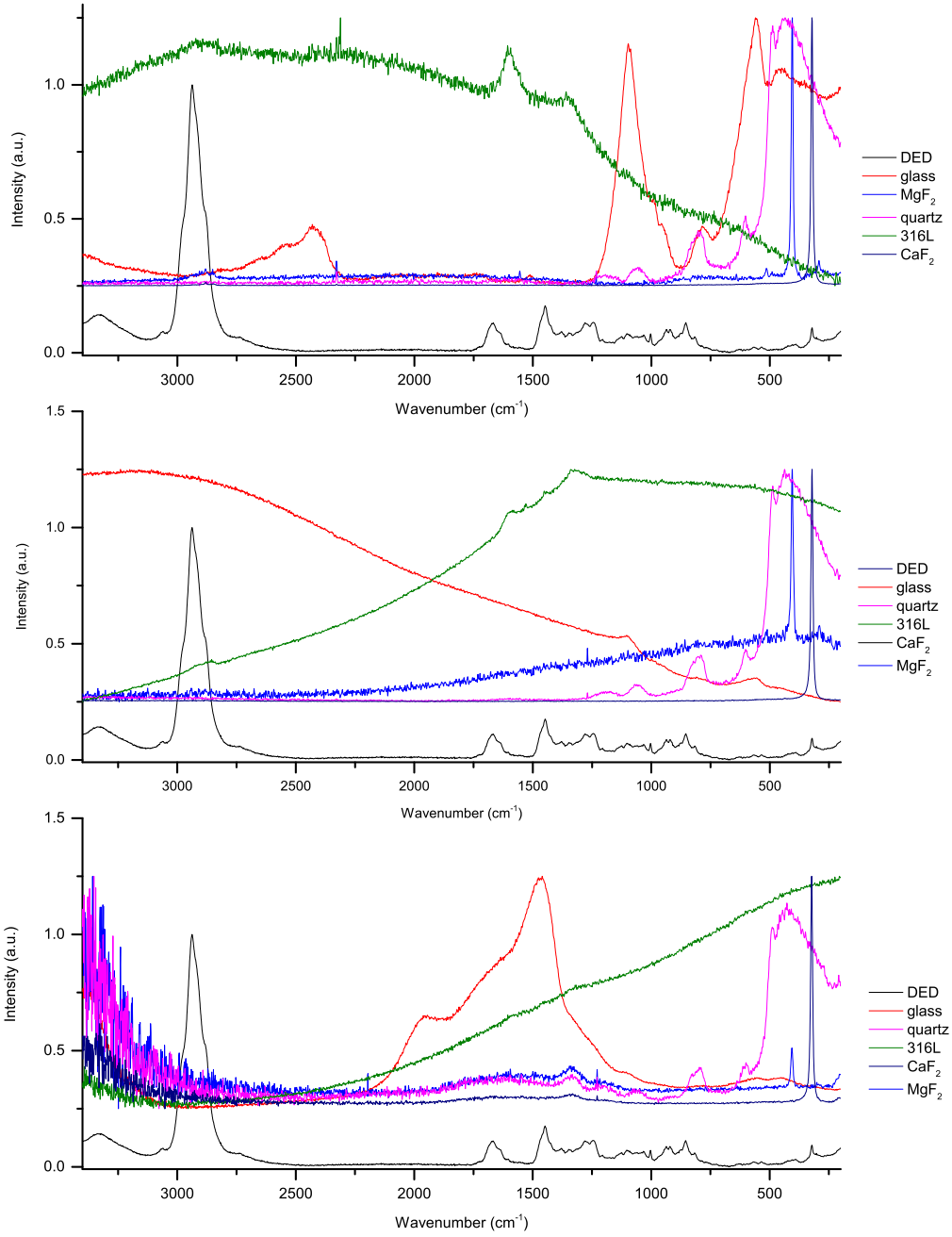

Figure 4.1: Raman spectra of common substrates for tissue sections using 532 (top), 633 (middle) and 780 (bottom) nm excitation. The measurements were taken off clean substrates and using identical collection parameters for each laser wavelength (25 s, two accumulations). The substrate spectra are offset to the Raman spectrum of a DED cryo section to highlight overlapping regions.

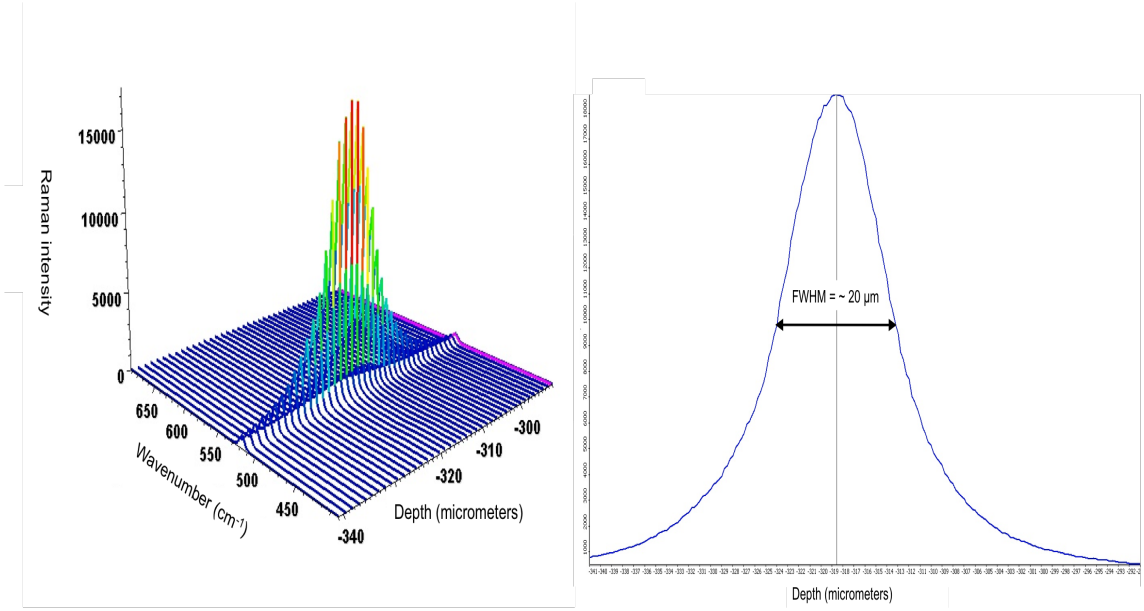

(a) (b)

Figure 4.2: Axial resolution of the system setup used for intact skin profiling (50x lwd objective (N.A.0.50), 50 μm-pinhole aperture). The resolution was measured by profiling 25μm above and below a Si surface. The 520 cm^{-1} peak was tracked to determine the full width at half maximum (FWHM). (a) 3D profile of Si surface versus depth. (b) Intensity of the 520 cm^{-1} Si peak plotted against depth. The FWHM is measured as 20 μm. Actual/real axial resolution in skin will not be exactly the same since laser attenuation is material dependent.

4.2.2 Choice of excitation wavelength

Restrictions that backing substrates pose depend on the excitation wavelength chosen for the experiment. One can be chosen that gives little interference with a cheaper substrate versus one that gives no interference but is expensive as long as: (i) the substrate signals can be successfully subtracted from tissue signals or (ii) we have several laser options. Figure 4.3 compares spectra with substrate backgrounds and after the backgrounds have been subtracted. This method is found to work well approximately 60% of the time. Choice of substrate is then sufficiently large as long as any laser can be used: if tissue spectra are independent of excitation wavelength. This is also important because research is published using RS on skin tissues using a variety of lasers such as 532 [Talari et al. 2015, Downes and Elfick 2010], 660 [Tfaili et al. 2012, Nguyen et al. 2012] to 1064 nm [Edwards, Williams, and Barry 1995, Barry, Edwards, and Williams 1992]. Peak assignments are made from papers using any number of these options.

Table 4.1: Common substrate materials and their spectral features

Substrate	532 nm excitation	633 nm excitation	780 nm excitation
Glass	Intense background between 2200-3000 cm^{-1} and intense bands below 1250 cm^{-1}	No prominent features, strong background	Broad background between 1000-2000 cm^{-1}
Quartz	Several bands below 900 cm^{-1}	Several bands below 900 cm^{-1}	Several bands below 900 cm^{-1}
Stainless steel	Strong baseline and medium intensity background between 2000-1000cm^{-1}	Strong baseline and medium intensity background between 2000-1000cm^{-1}	No prominent features, strong background
CaF_2	Single intense peak at 320 cm^{-1}	Single intense peak at 320 cm^{-1}	Single intense peak at 320 cm^{-1}
MgF_2	Single intense peak at 405 cm^{-1}	Single intense peak at 405 cm^{-1}	Single intense peak at 405 cm^{-1}

With identical collection parameters, Figure 4.4 shows that strong tissue signals can be obtained with wavelengths 532, 633 and 780 nm. But they differ in the amount signal processing required. For example, 633 nm excitation nearly always required some level of fluorescence correction. 532 nm excitation rarely required any processing but the high wavenumber region between 3400-2600 cm^{-1} often saturated for up to 70% of SC spectra. With regards repeatability, 532 and 780 nm were the most consistent across all layers of skin tissues. The correction protocol per tissue layer differed much more using 633 nm excitation.

Choice of laser becomes more important for intact skin measurements. The structure and composition of skin layers vary with depth. It also contains light absorbing compounds such as melanin. Shorter wavelengths scatter much more efficiently through this densely packed fabric, resulting in high attenuation: depth of penetration varies greatly with different wavelengths. In published works, signal loss due to physical processes has been measured using the Phenylalanine peak at 1002 cm^{-1} [Yu et al. 2013] or the Amide II band intensity at 1443 cm^{-1} [Tfaili et al. 2012]. This is likely because these peaks stand alone and are easily isolated. Figure 4.6 shows signal loss in skin measured against depth using Phenylalanine for 633 and 785 nm excitation. At 76μm depth, 20% of the signal is retained with the 633 nm laser, and up to 50% for the 785 nm laser. In fact, the use of Phenylalanine as a reference point for measuring signal loss is questionable. At 1002 cm^{-1}, the peak represents v(C-C) ring vibrations [Talari et al. 2015] which are abundant in keratins. Keratins are found at much greater concentrations in the stratified layers of skin tissues such as the SC (Chapter 6). And so, a Phenylalanine gradient is observed in even sections of tissue, Figure 4.8. On tissue sections, the intensity of this peak reduces by at least 50-100% between the SC and epidermis and up to 200-250% between the SC and dermis. The Amide II band intensity too is found to vary in layers (Figure 4.8). Signal loss for either of these peaks is unlikely to follow a steady gradient throughout all the layers in intact skin.

Apart from signal loss, in this work, NIR excitation produced good SNR for the fingerprint region, Figure 4.5, and required very little processing post-collection. But for 780 nm there was heavy contribution from the objective lenses that could not be subtracted.

4.2.3 Effects of sample preparation methods

In this thesis, apart from fresh intact samples, tissues were fixed in 3.7% formaldehyde and processed for sectioning using two different methods: cryo-embedding and wax-

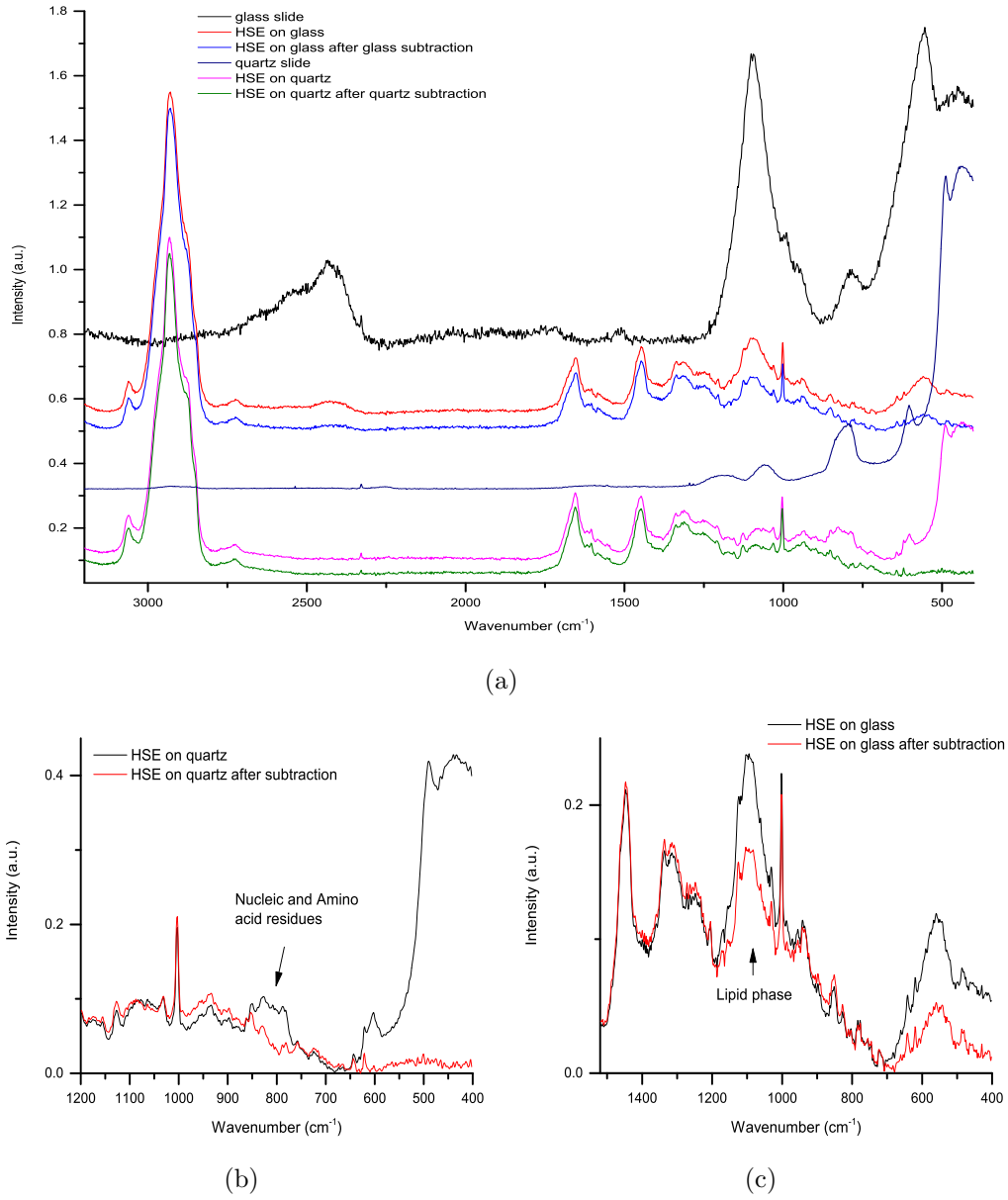

Figure 4.3: Effectiveness of removing quartz and glass substrate contributions post-collection. Unless successfully removed (bottom); quartz can mask a subtle and often underused region between 850-750 cm^{-1} assigned to nucleic acid residues of DNA and RNA, whereas glass can mask the 1200-1000 cm^{-1} region used for lipid phase analysis.

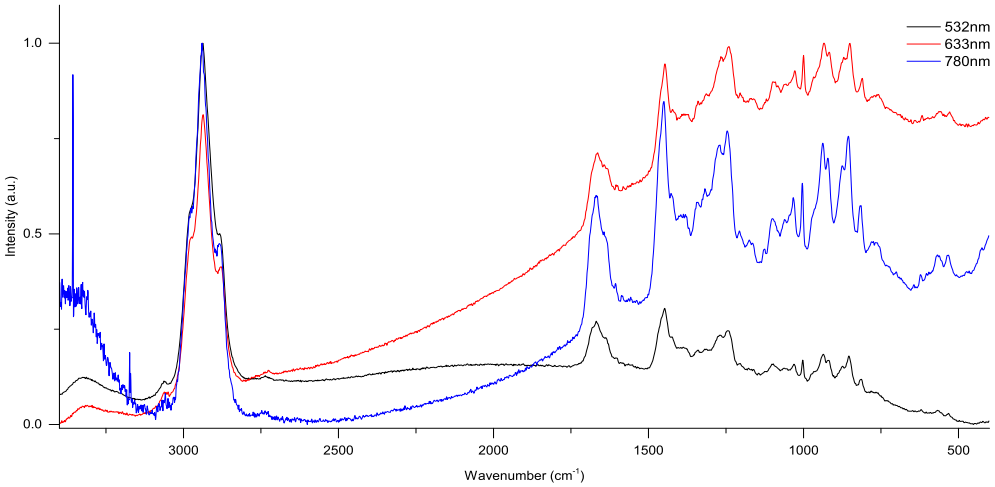

(a)

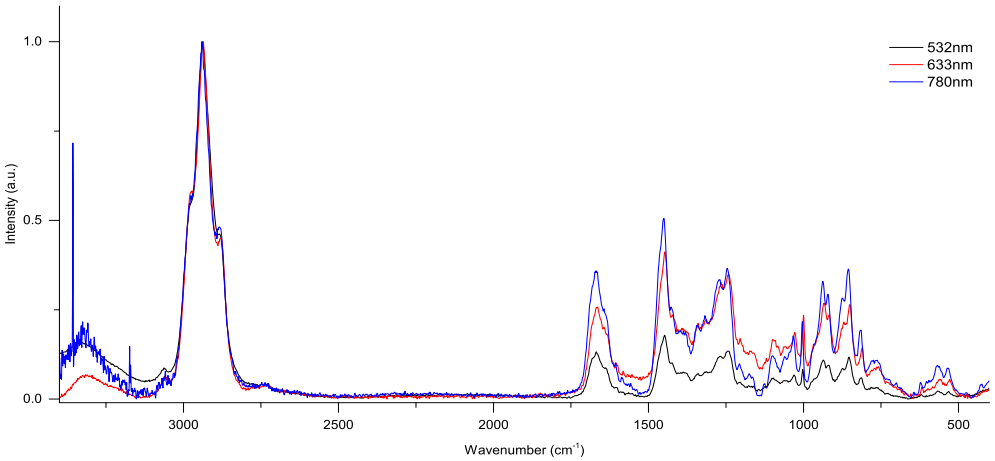

(b)

Figure 4.4: Comparison of the Raman spectrum of a DED cryo section with different laser wavelengths. (a) Raw spectra with identical collection parameters (25 s, three accumulations) and (b) Corrected spectra. 532 nm - baseline correction, 633 and 780 nm - 6th order fluorescence correction followed by baseline correction. The spectra were normalised to the high wavenumber region.

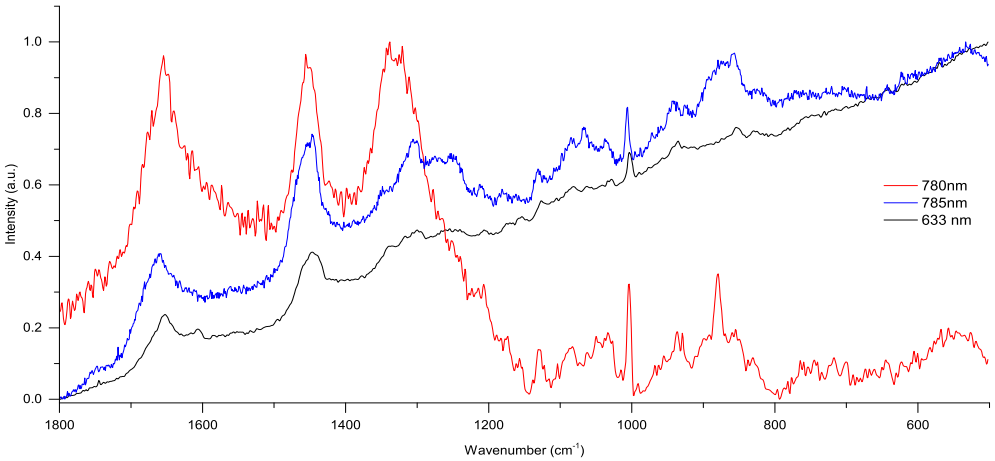

(a)

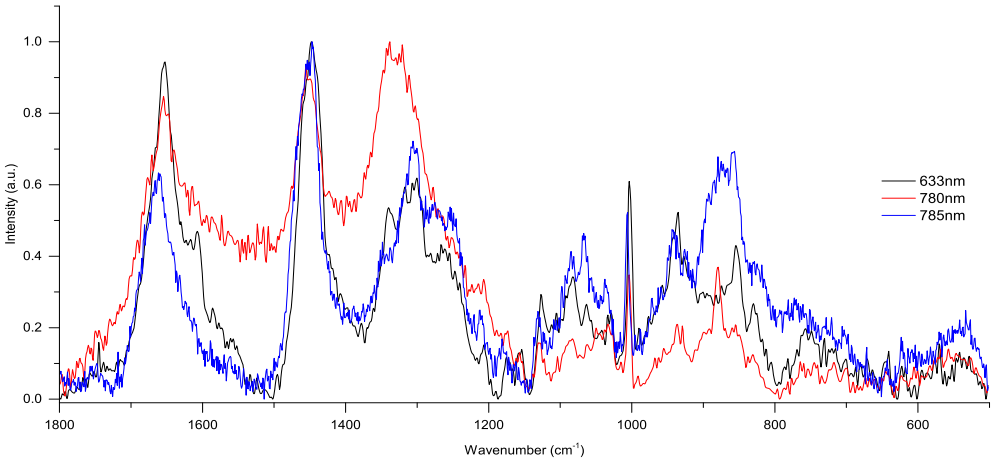

(b)

Figure 4.5: Comparison of the Raman spectra from the surface of intact skin tissues with different laser wavelengths. (a) Raw spectra in the region 1800-500 cm^{-1} and (b) Corrected spectra. 633 and 780 nm - 6th order fluorescence correction and baseline correction, 785 nm - baseline correction.

embedding. Fixation and processing has minor effects on the structures of skin tissues (Chapter 5). Aside from effects on the biochemical integrity of the sample, each method has separate advantages and disadvantages for Raman analysis in terms of practicality. Both methods require the sample to be embedded in a conserving/protective medium that can lead to artifacts. These can contribute to the spectroscopic signature. Cryo embedding involves the use of O.C.T. but this only enwraps the sample. As it does not diffuse through the tissues like wax, it is often an easier choice. The exception is CaF_2, MgF_2 and quartz slides where the wash protocols had to be changed to prevent the sample from sliding off during their submersion in PBS. Wash times were kept to <1 minutes and the number of cycles increased. Wax removal from these slides also had to be modified to prevent tissue slippage. In this case, sections on CaF_2, MgF_2 and quartz slides had to be baked at 60C before Xylene washes (in some cases tissues slipped off quartz despite baking + reduced wash cycles). For signal quality, cryo sections showed higher SNR compared to wax embedded sections under identical collection parameters, Figure 4.7. The spectral features were more defined in frozen samples.

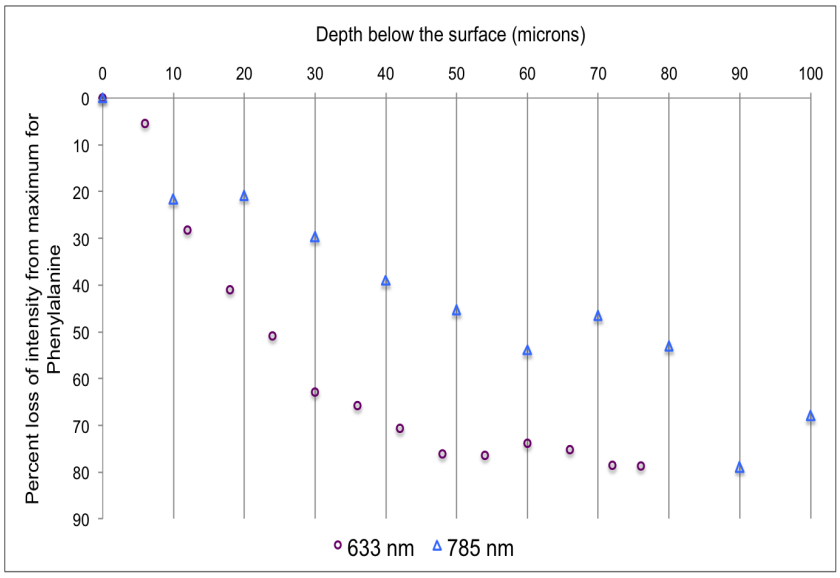

Figure 4.6: Laser attenuation in fresh intact skin tissues plotted against depth for 633 and 785 nm excitation. The signal loss is measured as a percentage loss from the intensity of the Phenylalanine peak at 1002 cm^{-1} at the surface, down to 80 μm and 100 μm depth.

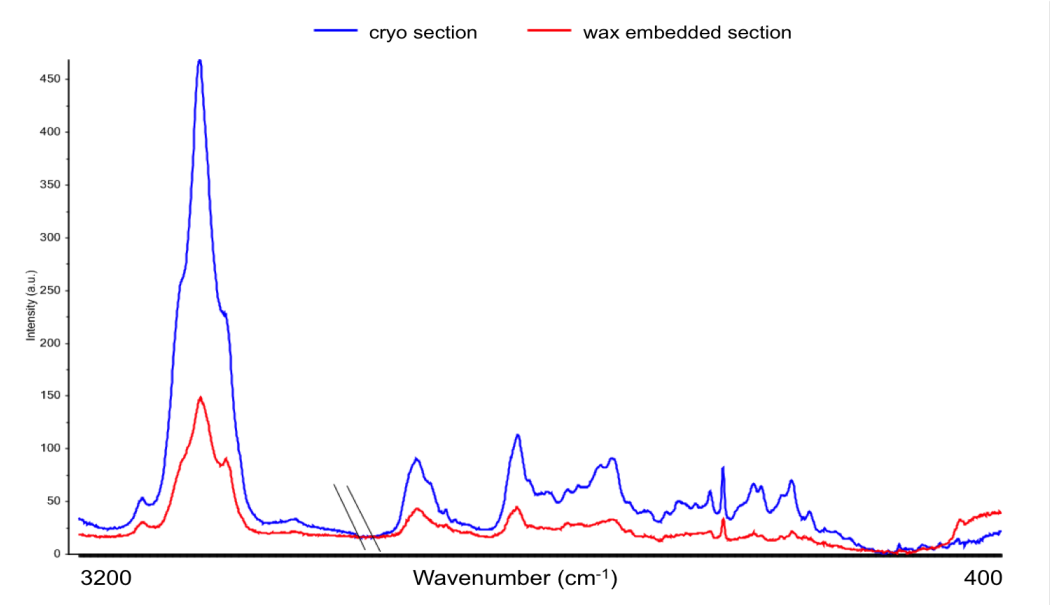

Figure 4.7: Averaged Raman spectrum of wax embedded and cryo embedded DED samples. Collection parameters were kept identical (30 s, three exposures). Spectra with higher SNR and more defined features are collected in shorter times for cryo sectioned samples.

The main problem faced in this work was the removal of wax from wax embedded samples. Despite following an established protocol [Mian 2015], it is to be noted that Xylene washes were not very successful in removing all the wax from samples on any of the substrates. This was likely a user-error as it is a method used often and with very good outcomes. Here, the wax peaks were instead removed digitally, post-collection (Figure 4.9). Whilst the approach was generally successful, many of the wax peak positions are equivalent to positions observed for tissue lipids (Chapter 6). Notably, there is also suggestion that wax embedding and the subsequent processing steps may remove lipid components of skin layers that are structurally similar to wax [Ali et al. 2013b].

4.3 Discussion

Various practical aspects of sample presentation for Raman analyses is given in this chapter. The purpose was three-fold: (i) make data collection easier through changes to sample handling (e.g. increase thickness of sections to avoid substrate subtraction), (ii) consider some instrument-specific conditions (e.g. minimum time for depth profiling)

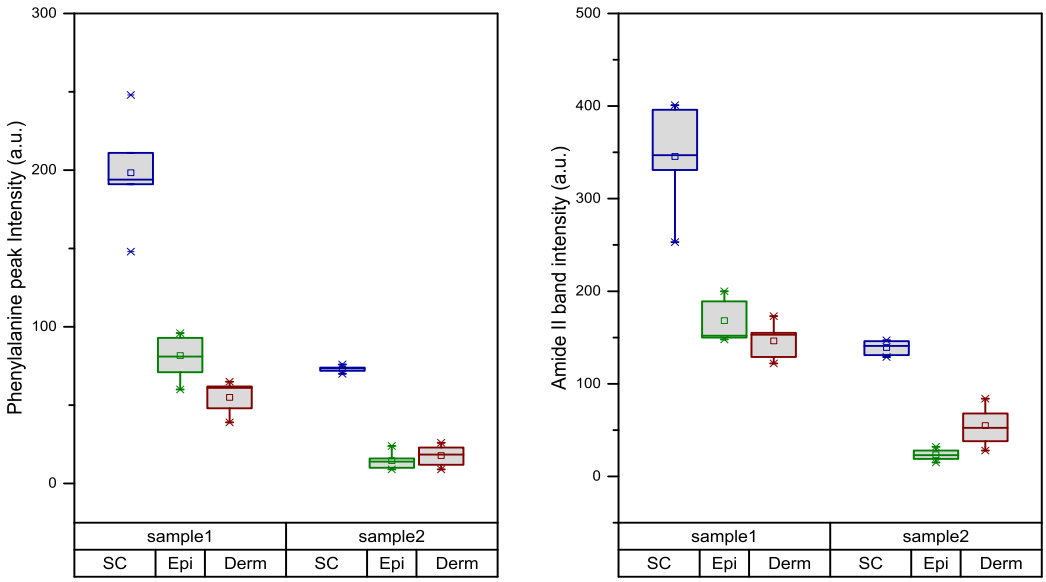

Figure 4.8: Peak intensity of Phenylalanine (left) and Amide II (right) measured from cryo sectioned HSEs plotted against layer. The intensity gradient decreases in the direction from the SC toward the epidermis and dermis. The spectra were normalised to the high wavenumber region and intensities were measured against baseline offset.

and (iii) detail post-collection necessities (e.g. ease of fluorescence corrections).

The thickness to which skin samples need to be sectioned for Raman analysis is an important consideration. Samples used in this thesis tended to be 1.5-2 cm^2 in size. Sections needed to be kept thin so as not to waste samples but thick enough to ensure data collection and perhaps more importantly, data processing was not too difficult or time consuming. Substrate signals can complicate interpretation of tissue spectra if they overlap. Out of several common substrates, CaF_2 and MgF_2 are unparalleled with regards the ease of excluding their Raman signals from that of tissue. Glass generally performed poorly, with quartz and stainless steel only outperforming glass because their signals could be subtracted with greater success. However, the contrast is not so clear when cost and ease of mounting is taken into account. CaF_2 and MgF_2 are expensive substrates. While sections were mounted easily, washing off wax and O.C.T. was difficult. Wax embedded sectioned needed to be baked at 60C before xylene washes to prevent the sections from sliding off the slides (also true for quartz). The washing cycle

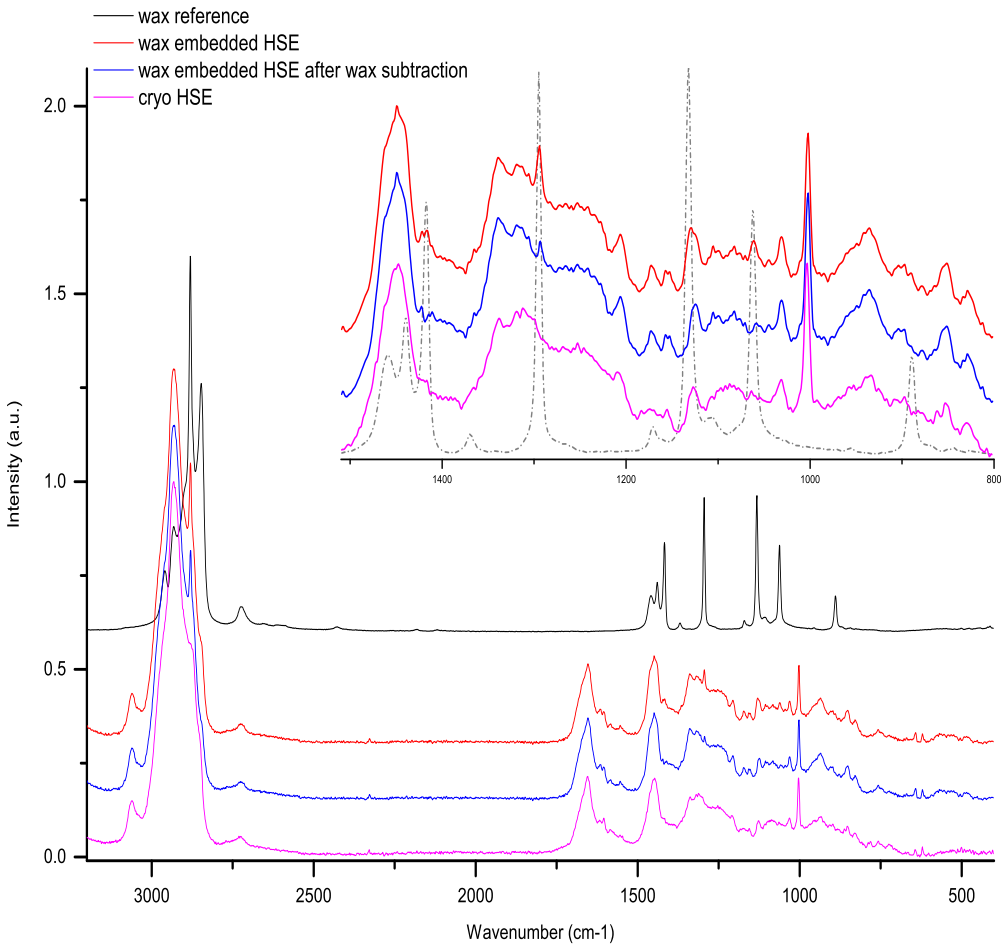

Figure 4.9: Comparison of tissue signals from wax embedded (before and after wax subtraction), and cryo sectioned HSE samples. Raman signature of wax includes peaks at 1062, 1133, 1296 and 1441 cm^{-1}. These peaks are also associated with v(C-C) and $\delta(CH_2, CH_3)$ vibrations of skin tissue lipids [Barry, Edwards, and Williams 1992, Lakshmi, Faoláin et al. 2005]. Subtracting a wax reference spectrum works well but might cause some lipid information to be lost.

needed to be adjusted to multiple <1 minute courses for cryo sections. Stainless steel slides could have been a potential rival but also suffer from the same disadvantages. Out of all the substrates, stainless steel slides were found to retain the most wax after long xylene washes. CaF_2 and quartz have previously been shown to retain more wax than low-E slides by other groups [Fullwood et al. 2014]. Glass slides presented the least concern about sample preparation methods because the wash cycles are already established due to extensive use [Mian 2015]. Still, where available, quartz slides were preferred for subsequent work. Quartz spectra are more easily subtracted from tissue spectra compared to glass which overlaps tissue regions important for lipid phase analysis.

In fact, washing off O.C.T. was problematic for some slides but here, we found wax removal was also problematic. Given the comparative nature of Raman work, any concern over the purity of lipid data would still have been compensated if all samples used in this work were wax embedded. As both cryo and wax embedded samples were used, wax signals had to be digitally removed from nearly all wax embedded sample spectra when comparing data. As for advantages: Wax embedded samples can be preserved for much longer. But cryo sections produced spectra with much higher SNRs compared to wax and O.C.T. was not found to contribute to their spectra. Cryo sections are also thought to compare very well with fresh tissues [Shim and Wilson 1996], except for some differences in the vibrational modes of proteins [Faoláin et al. 2005]. It is suggested that re-hydration of cryo sections in PBS before Raman collection can even further improve signal quality [Bonnier et al. 2012].

Substrate performance and tissue signal strength varied with different excitation wavelengths. There are clear differences in tissue spectra collected using VIS and NIR wavelengths that stem from resonance effects and limitations to the efficiency of CCDs [McCreery 2005]. For example, 488 nm is close to the resonance frequency of carotenoids and is always more intense in lower VIS lasers [Hata et al. 2000]. Whilst the high wavenumber region of tissue spectra between 3200-2600 cm^{-1} is less intense in the NIR compared to VIS due to lower CCD quantum efficiency. This chapter was concerned with the practical implications of using different lasers. Each laser provided spectra with sufficiently high SNR for detailed analysis. Quartz, CaF_2 and MgF_2 were all good substrates to use for all three lasers but stainless steel had intense baselines for all lasers. For tissue sections on glass slides, glass fluorescence was found to overwhelm all biological signals even under highly confocal collection modes for >633nm. This limited work

with glass slides to VIS lasers. Apart from substrates, the lasers had a big difference in signal processing required post collection. Little to no fluorescence is expected with excitation wavelengths over 600 nm [Bonnier et al. 2011] but here, heavy corrections were needed with 633 nm. This was more pronounced in intact skins. Whereas 785 and 532 nm often only needed baseline correction. Processing spectra from different lasers and of different qualities is a big aspect of MVA; where it is critical to reduce variations due to instrument/collection parameters (such as baseline offsets due to fluorescence) in order to focus on biochemical differences.

There are few papers that detail *in vivo* Raman measurements on skin tissues [Gniadecka et al. 1998, Schallreuter et al. 1996, Barry, Edwards, and Williams 1992, Shim and Wilson 1996]. Even fewer that deal with penetration to some tens of microns depth that keep SNR high enough to perform analysis on fingerprint regions. These include reports of profiles down to 48 [Chrit et al. 2005], 60 [Yu et al. 2013] and 85 μm [Caspers et al. 1998]. The profile depths can be up to 200 μm when only looking at the high wavenumber region for measuring water content [Caspers et al. 2001, Caspers, Lucassen, and Puppels 2003]. Only one paper was found to assess penetration depth in skin tissue (pig skin) by looking at the signal loss down to 36 μm [Tfaili et al. 2012]. Where signal loss was measured as a function of the Amide II band intensity at 1443 cm^{-1}. For 633 nm excitation, the loss was nearly 100%, and approximately 80% for 785 nm excitation at the profile limit. Here, the signal loss we report is much lower: approximately 90% loss for 633 nm and 50% loss for 785 nm at 80μm. This is not wholly surprising as collection parameters (objective, laser power, exposure time) and spectrum normalising methods were different. Collection time for each spectrum of the depth profiles using the 633 nm laser were closer to 7 minutes compared to 20 seconds in [Tfaili et al. 2012]. A likely reason for having so few papers detailing signal loss is this: signal loss is both instrument specific and user specific. There also doesn't appear to be an established standard for normalising spectra for penetration studies. As well as the Amide II band previously mentioned, the 2930cm^{-1} protein band [Chrit et al. 2005, Caspers et al. 2001] has been used for this purpose. And works that measure penetration of chemicals into skin often measure this against keratin, assuming keratin content is constant with depth [Bonnist et al. 2011a, Broding et al. 2011]. Many of these bands have natural gradients in skin. In particular, keratin gradients are shown to vary greatly from its expression in all suprabasal layers to only in higher suprabasal layers with different HSE products and culture conditions [Boelsma et al. 2000]. This was also true for HSE samples used in this thesis where we see a 50-100 % reduction

in the intensity of the Phenylalanine peak at 1002 cm^{-1} between the SC and the viable epidermis. Signal loss and penetration of chemicals would be best measured against a peak that remains constant through all the skin layers. Without a constant, it is difficult to determine whether: (i) the chemical concentration is decreasing while keratin stays constant, or (ii) both the chemical and keratin is decreasing -but at different rates. Despite detailed analysis of the spectra from skin layers (Chapter 5), we were unable to find such a peak. Where even the Amide II band was seen to vary between layers of cryo sections of skin tissues. The Amide II band is even shown to be affected by the hydration state of tissues. Its intensity increases relative to the Amide I band as fresh tissues dry out [Shim and Wilson 1996]. Interpreting data that is tracking ratios needs to be done carefully unless one of the peaks can be isolated and measured independently.

4.4 Conclusions

The effects of several sample preparation and presentation methods are explained in this chapter. Substrates and sample preservation chemicals are found to interfere with signals from tissues. Either of these may be prevented by choosing suitable substrates and laser wavelengths or by digital removal post data acquisition. However, avoiding all interference is very difficult because of either the specific application, cost-limitations or the availability of suitable materials. Point in fact, data for this thesis was collected from samples on different substrates, using different wavelengths and preserved with different chemicals. It would be difficult to carry out the necessary analysis in subsequent chapters on spectral regions not affected by these user-dependent variables (there is very little). Instead, the approach has been to study their effects and recognise their contribution while interpreting tissue signals.

Chapter 5

Normal Skin Tissue

5.1 Introduction

Non destructive tissue characterisation methods are not what they should be. Techniques used to describe tissue layers well are invasive, rely on external contrast agents, render the sample non viable or have limited depth penetration [Georgakoudi et al. 2008]. This chapter explores the use Raman spectroscopy to observe biochemical and structural information in engineered human skin equivalents (HSEs).

HSEs have clinical relevance. The European Commissions Cosmetics Directive has recently constrained the testing and marketing of finished cosmetic products and ingredients on animals. Under the REACH legislation, testing of cosmetic products on animals are prohibited where alternatives are available and the sale of products newly tested on animals are banned within Europe regardless of the country the testing was carried out in. This has motivated increasing research into HSEs as an alternative to perform safety tests on a wide range of products including cosmetics and pharmaceutical formulations. Their production requires sterile conditions making in vivo access by standard biological techniques difficult. Monitoring and evaluating the effects of changes in process conditions or tracking the tested formulations are mostly limited to *in vitro* observations. The HSEs are cultured, sacrificed and fixed prior to analysis. This approach has several disadvantages. The fixation steps may lead to artifacts. But in particular, monitoring a parameter at different time points limits the frequency with which observations are made as it requires multiple samples to be made and sacrificed. Accessing and monitoring the HSE products *in situ* under normal growth conditions will be a major advantage to determine the impact of process parameters on living

systems.

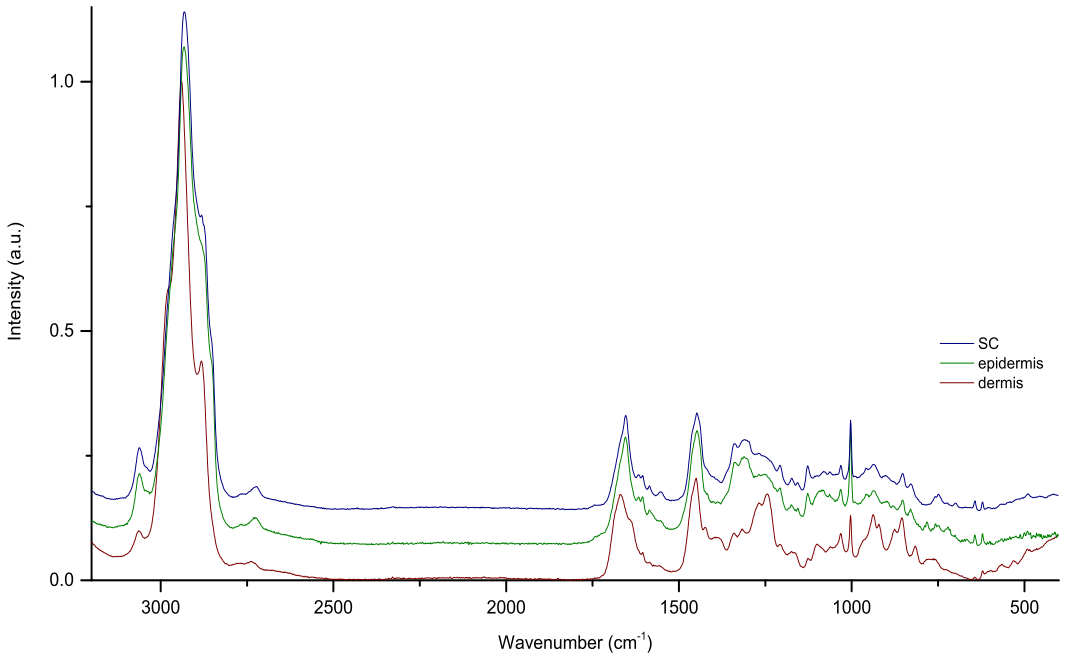

Figure 5.1: Raman spectra of the SC, epidermis and dermis of an engineered skin model.

5.2 Results

5.2.1 Layer characterisation

Skin is a highly heterogeneous tissue composed of layers which are dissimilar in structure, molecular composition and function. The epidermis is comprised of multiple levels starting with the SC at the air/skin interface down to the basal layer closest to the basement membrane. The basal layer sees a continuous proliferation of cells that constantly move upward and become the anuclear, keratinized cells of the SC where they are routinely shed (Chapter 1). At this top layer, the anucleated cells are embedded in a matrix of lipid-by-layers, which act as a water sealant. This forms the primary barrier to the external environment with the keratinocytes also acting as immunomodulators. The epidermis is supported by the dermis which provides mechanical strength to the skin and regulates internal temperature. Each of these layers may be altered

in different ways under disease states [Knudsen, Edwards, Williams, and Barry 1995, Hata et al. 2000] or through the application of cosmetic and drug formulations [Tfayli et al. 2012, Bonnist et al. 2011b, Broding et al. 2011]. There is a need for better ways of monitoring such alterations. This section describes how Raman data may be used to identify and characterise some aspects of these skin layers.

5.2.1.1 Human skin equivalents

Resolving skin layers from lipid-to-protein concentrations: υ(CH) vibrations of lipids and proteins are represented in the region 3200-2600 cm^{-1} (Figure 5.2). The region has prominent features that are protein specific at 2980 and 2930 cm^{-1} representing $\upsilon(CH_3)$ vibrations; and bands at 2880 and 2840 cm^{-1} that originate from $\upsilon(CH_2)$ asymmetric and symmetric vibrations of lipids [Ali et al. 2013b, Gniadecka et al. 1998]. The 2880 and 2840 cm^{-1} lipid band intensities decrease relative to the main protein band at 2930 cm^{-1} as skin is profiled from the surface. Figure 5.2d charts the ratios I_{2930}/I_{2880} and I_{2930}/I_{2840} against the skin layer from which they stem from. The charts indicate a gradient from lipid-rich to protein-rich in the direction of the SC/epidermis to the dermis. The greatest change is in I_{2930}/I_{2840} which increases by at least three-fold between the epidermis and the dermis.

There are two other major bands of lipids at 1438 and 1300 cm^{-1} representing $\delta(CH_2)$ vibrations [Talari et al. 2015]. The peak at 1438 cm^{-1} is masked by Amide II, but a slight decrease in the 1300 cm^{-1} peak is observed between the SC and epidermis with most day 14 HSEs that formed a mature SC layer (Figure 5.2b). Apart from the high wavenumber lipids, the dermal layer may also be identified through three spectral features related to collagen. The 2980 cm^{-1} shoulder band of protein increases as the collection volume reaches the dermal component, Figure 5.3b. This shoulder band is a prominent feature of collagen [Nijssen et al. 2002]. Secondly: the 1267 and 1248 cm^{-1} bands increase markedly relative to the 1400-1300 cm^{-1} band of Amide III, Figure 5.3c. These two represent the υ(C-N) and δ(N-H) vibrations of collagen at 1267 cm^{-1} and 1248 cm^{-1} [Talari et al. 2015]. Thirdly: the 920 and 855 cm^{-1} peaks represent vibrations of the amino acid side chains proline and hydroxyproline and the υ(C-C) backbone vibrations of collagen [Caspers et al. 1998, Talari et al. 2015]. These amino acids makeup nearly a quarter of those found in collagen and the bands representing them show a clear and marked increase in the dermis, Figure 5.3d. Observing these three features of collagen may be used as a marker for the boundary between the epidermal and dermal

layers in skin tissues.

Ascertaining the lipid phases of the Stratum Corneum: The 1200-1000 cm^{-1} region contains information on the order of lateral packing of the acyl chains. Where peaks at 1130, 1080 and 1060 cm^{-1} represent the υ(C-C) vibrations of trans, random(gauche) and trans lipids respectively [Chrit et al. 2005, Gniadecka et al. 1998]. These peaks are characteristic of the Raman spectrum of ceramide which is found extensively in the lipids of the SC [Wegener et al. 1996, Wegener et al. 1997]. In trans conformation the lipids are highly ordered and the intermolecular structure is stable. In HSEs with well-formed SC layers, the lipids were mostly in either a predominantly trans phase or had a mixture of trans and gauche lipids, Figure 5.4. For most cases, the 1080 cm^{-1} gauche peak increased relative to the trans peaks as the collection volume moved into the epidermal layer. This suggests the lipids of the viable epidermis adopting a combination of trans and gauche configuration. This region of lipids was found to be sample specific and showed large regional variations, Figure 5.4.

Conformational differences in proteins of the SC, epidermis and dermis: A noticeable feature observed in the high wavenumber region is a shift of the 2930 cm^{-1} band of proteins to higher wave numbers in dermis spectra (Figure 5.5). It has been previously suggested that this shift likely represents a highly folded and compact protein structure in the SC and epidermis versus a more unfolded structure in the dermis [Gniadecka et al. 1998]. And that the looser form in the dermis exposes and allows the amino acid side chains to interact and bond with water [Verma and Wallach 1977]. The band maxima at a higher wavenumber for the SC and epidermis therefore describe instead a form that is probably hydrophobic to its environment.

There are several Raman vibrational bands in the form of the amide regions which are sensitive to the conformational state of proteins. These bands represent various aspects of the peptide linkage that form the protein macromolecules, Figure 5.6. The proteins' shape in space depends upon the secondary and tertiary structures of the chain, where the secondary structure is formed by folding of the primary chain so as to maximise the number of hydrogen bonds formed between different parts of the chain. There is an interdependency between the hydrogen bonding state of the peptide bonds and the frequency of the amide vibrations [Walsh et al. 2003, Qian, Mirkin, and Krimm 1999]. Because of this, the amount of secondary structures of proteins or any changes thereof may be detected in the amide bands, Figure 5.6.

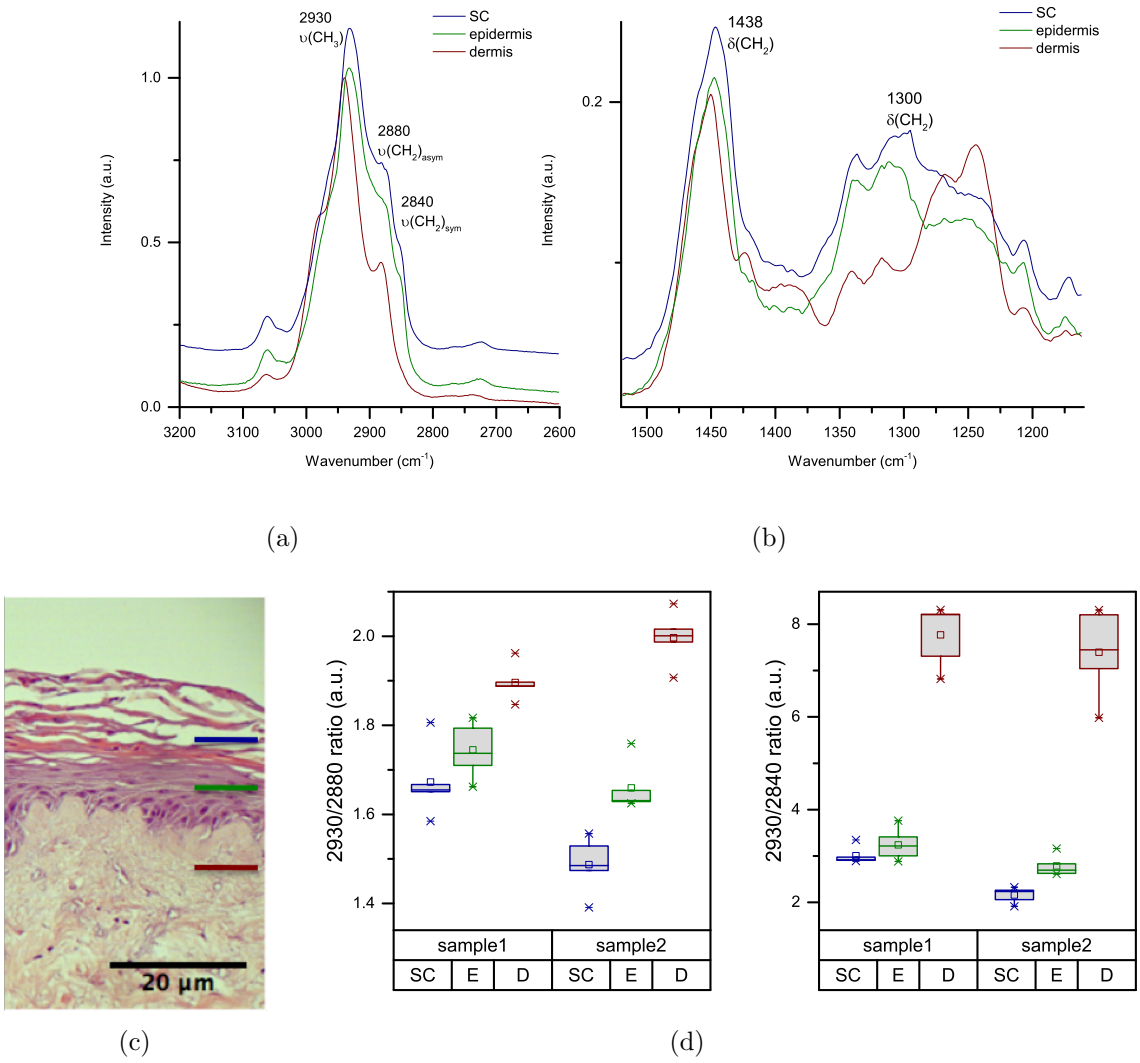

Figure 5.2: Prominent spectral markers of lipids: (a,b) Raman spectrum of SC, epidermis and dermis from a cryo-embeded day 14 HSE in regions. 3200-2600 cm^{-1} (a) and 1510-1140 cm^{-1} (b). The annotations highlight peaks associated with overall protein content (2930 cm^{-1}), and lipid content (2880, 2840, 1438 and 1300 cm^{-1}). (c) H&E stained section of a day 14 HSE. (d) Charts following the ratios $I_{2930/2880}$ and $I_{2930/2840}$ in the SC, epidermis (E) and dermis (D) of two cryo-embeded day 14 HSEs. The peaks intensities were measured as the height from baseline offset for the fixed locations of 2930, 2880 and 2840 cm^{-1}. For both, there is a gradient from high relative lipids to high relative proteins in the direction from SC to dermis.

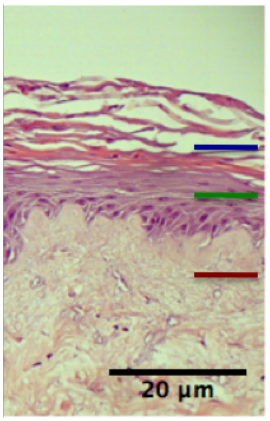

(a)

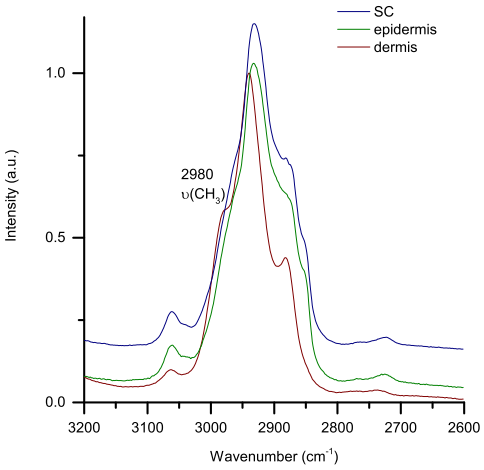

(b)

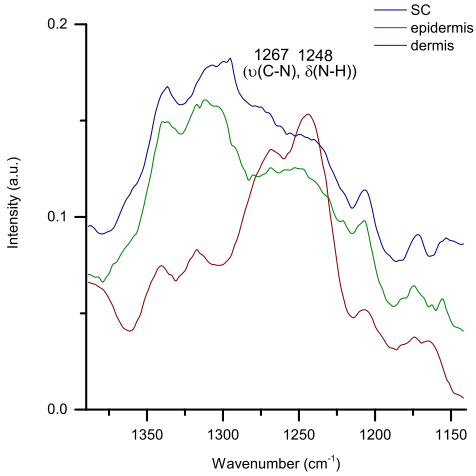

(c)

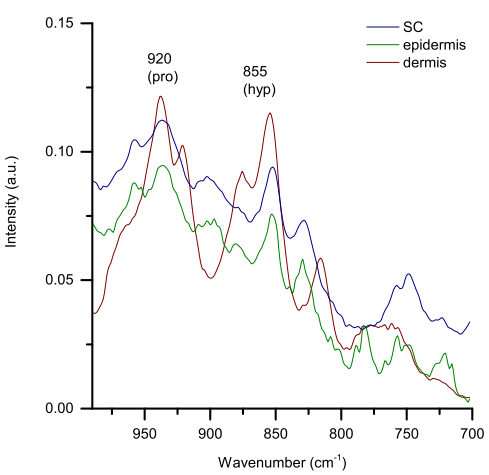

(d)

Figure 5.3: Prominent spectral markers of collagen: (a) H&E stained section of a day 14 HSE. (b) 2980 cm^{-1} shoulder band of $\upsilon(CH_3)$ vibrations. (c) 1267 and 1248 cm^{-1} peaks of υ(C-N) and δ(N-H) vibrations (Amide III). (d) 920 and 855 cm^{-1} peaks of υ(C-C) vibrations for proline and hydroxyproline. There is an abrupt change in all of these bands as the collection volume moves into the dermal component.

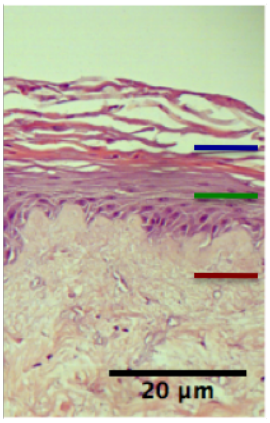

(a)

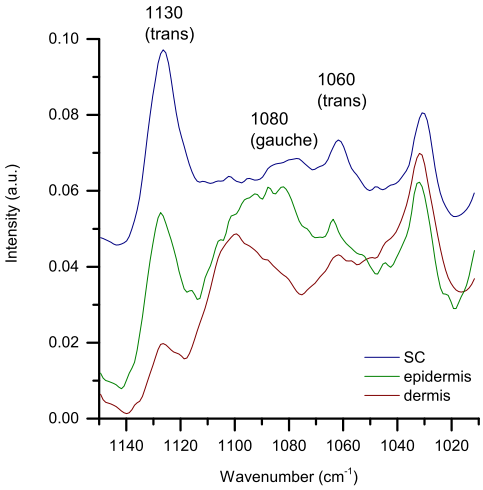

(b)

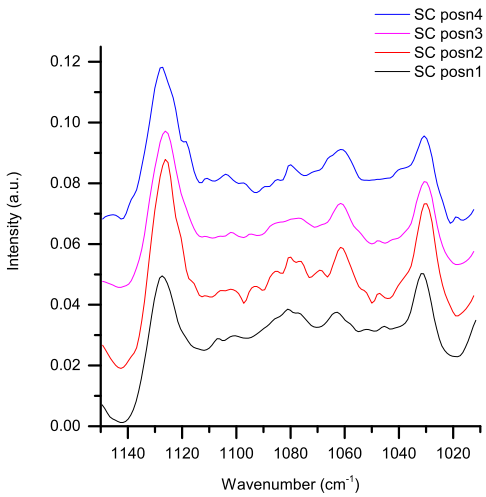

(c)

Figure 5.4: (a) H&E stained cryo section of day 14 HSE. (b) Raman spectrum of SC, epidermis and dermis in the 1200-1000 cm^{-1} region of lipids. Prominent trans lipid peaks in the SC decrease as gauche lipid peaks increase in the epidermis. (c) Raman spectrum of the SC at four random locations on the same cyro section. Relative trans/gauche peak intensities vary across the same samples and between samples.

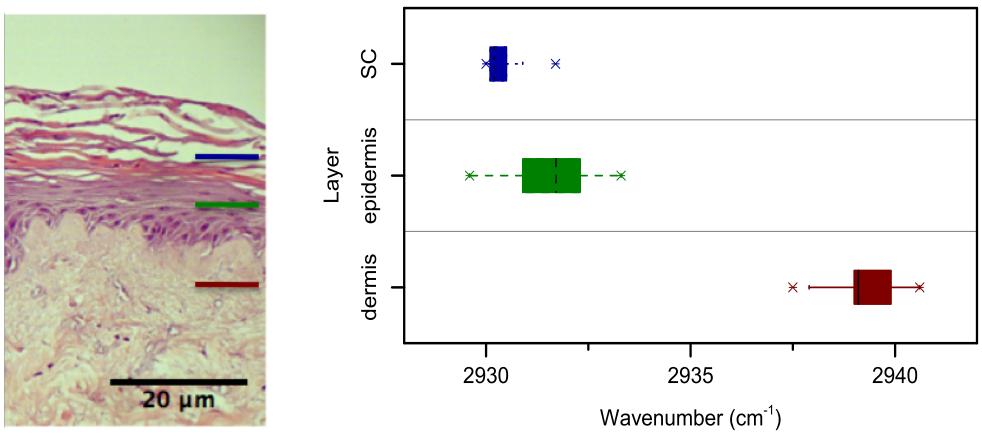

(a) (b)

Figure 5.5: Position of the 2930 cm^{-1} protein band for cryo embedded, day 14 HSE samples across tissue layers. The band position moves by several wavenumbers in the dermis.

The Amide I band in particular is considered to be highly sensitive to the secondary structure of the protein backbone. Estimation of the percentage of secondary structures and conformational alterations under different experimental conditions have shown good correlation between X-Ray diffraction data and RS [Berjot, Marx, and Alix 1987]. The main contributor to the band is the υ(C=O) vibrations of the backbone structure with minor contributions from the υ(C-N) and δ(N-H) vibrations. Amide I is seen to broaden as the collection volume moves down into the dermis, Figure 5.7. This may be attributed to the increased presence of collagen at 1666 and 1631 cm^{-1} [Gasior-glogowska et al. 2010]. As well as broadening, a shift is observed in the band maxima similar to that seen with the 2930 cm^{-1} band. The band may be decomposed into the component Raman peaks for α-helical (1640, 1650-52 cm^{-1}), unordered (1660 cm^{-1}) and β-sheet (1673 cm^{-1}) forms [Berjot, Marx, and Alix 1987]. In the SC and epidermis, the Amide I position suggests the presence of largely α-helical proteins. Large amounts of keratin in this region may account for this. Whereas, in the dermis, an upshift suggests that while some α-helix forms still remain, there is a much higher percentage of unordered and β-sheet forms (Figure 5.7). The band maxima for the dermis more closely resembles those seen in pure type I and IV collagen spectra [Nguyen et al. 2012].

The Amide II band largely represents δ(N-H) and υ(C-N) vibrations of proteins. The band does not alter much between the epidermis and dermis. An occasional exception

is areas that are very high in lipids. A large increase of a component peak representing vibrations of lipids at 1438 cm^{-1} results in a slight shift of the band in some lipid-rich areas.

The Amide III band represents the υ(C-N) and δ(N-H) vibrations (Figure 5.7). In contrast with the other Amide bands, large contributions from the protein side chain vibrations in this band make it difficult to be conclusive about secondary structure. Still, some limited conformational information may be extracted. Characteristic of α-helical conformation is the 1267 cm^{-1} band, the 1248 cm^{-1} band represents an unordered conformation [Gasior-glogowska et al. 2010] and β-sheet forms are represented at 1230 cm^{-1}. Here too, the proportion of α-helix forms are greater than in the unordered and β-sheet conformations in the epidermis and vice versa for the dermis. However; the distribution of these forms varied within cryo embedded and between wax and cryo embedded samples (section 5.2.2).

Apart from the H-bonds that help maintain the secondary and tertiary structures, a more powerful covalent bond is formed in proteins that contain (-SH) groups. Namely; disulphide bridges. Two peaks that represent υ(C-S) vibrations are observed at approximately 640 and 620 cm^{-1}. These peaks are striking in the spectrum of the SC and in the epidermis (to a lower extent) but disappear in the dermis (Figure 5.8). They likely arise from keratins which contain large amounts of Cysteine. The disulphide bridges form keratin into a helical structure imparting a string like function to it.

5.2.1.2 Sampling and source variations

Distinct structural and compositional differences of skin layers impart different functions to each layer. It is important that HSEs mimic these differences as they will dictate the functional state of the composite. Testing products on HSEs that are similar to native human skin will ensure any data resulting from tests carried out on them to be extended to real skin making them clinically relevant. This section describes how closely Raman data of HSEs resemble those from native skin tissues and how dependent layer information is on sampling methods.

Spectral fingerprints for native skins and engineered HSEs grown at the air-liquid interface for 14 days differ in their lipid content. In native samples, I_{2930}/I_{2880} shows a more separate step-wise increase between both the SC and epidermis and the epi-

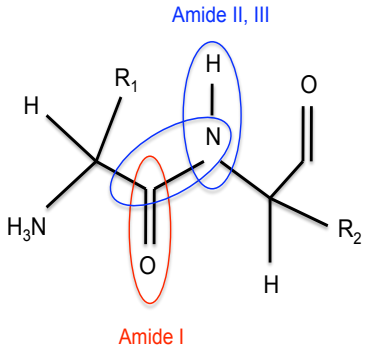

Spectral band	Associated with
Amide I	υ(C=O), δ(CCN)
	υ(NH)
Amide II	δ(NH), υ(CN)
	υ(CC), δ(C=O)
Amide III	δ(NH), υ(CN)

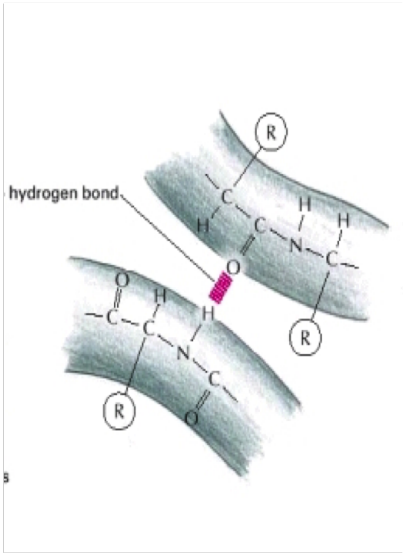

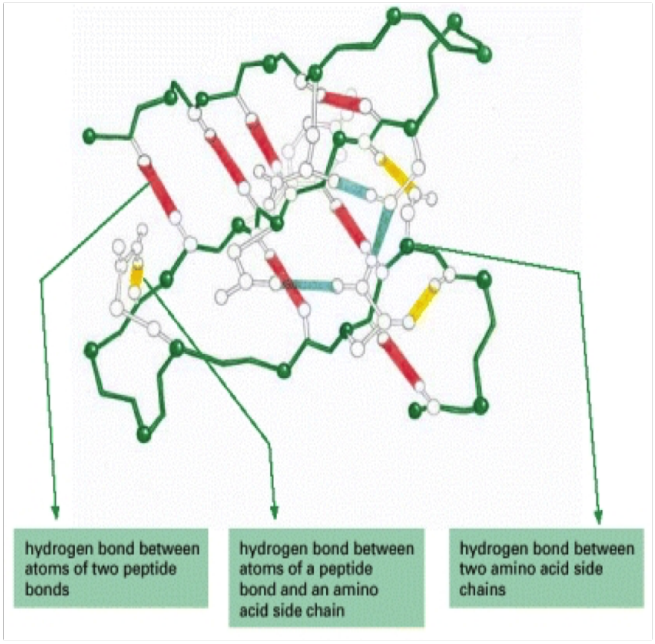

Figure 5.6: Clockwise from top-right: Peptide link of proteins and the raman bands associated with different segments of the link [Barth and Zscherp 2002]. Hydrogen-bonding between peptide chains and hydrogen-bonding between different components of the peptide chain as the protein folds [Alberts et al. 2013].

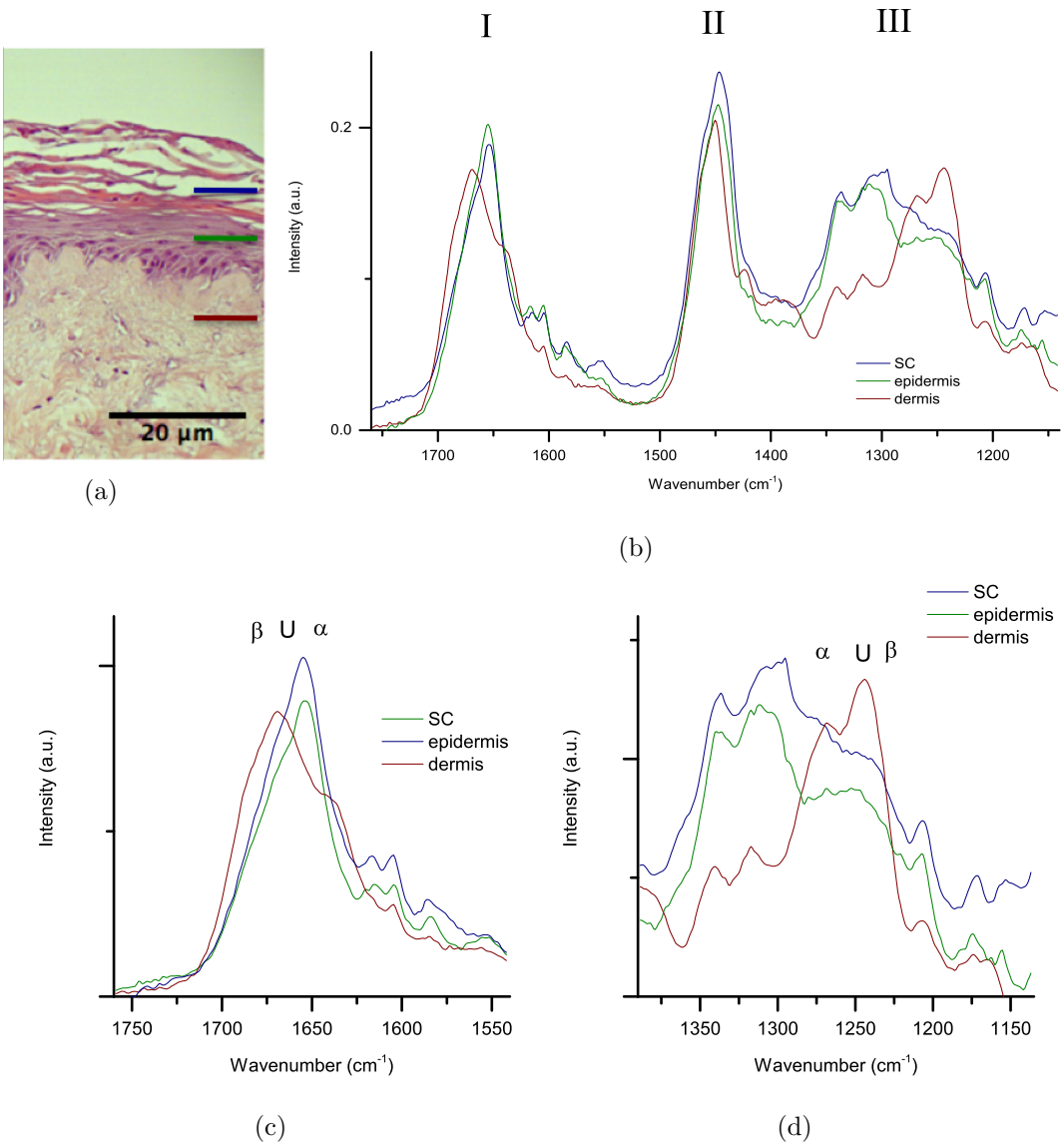

Figure 5.7: (a) H&E stained section of a cryo embedded day 14 HSE and (b) Raman spectra from the Amide regions (1760-1140 cm^{-1}). Amides I (c) and III (d) highlighting differences between the SC, epidermis and dermis in cryo embedded HSE samples. Amide I and III annotations show the protein conformations expected in the respective peak positions.

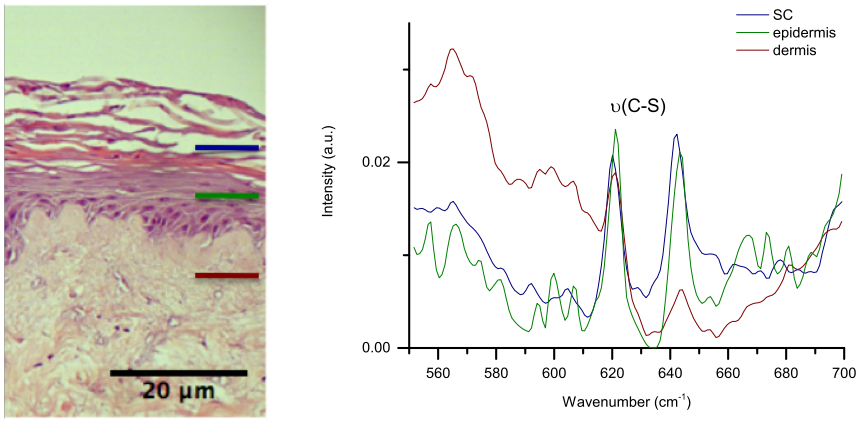

(a) (b)

Figure 5.8: (left) H&E stained section of a day 14 HSE. (right) Raman spectrum of SC, epidermis and dermis in the 800-400 cm^{-1} region. Peaks at 640 and 620 cm^{-1} representing v(C-S) vibrations decrease and then mostly disappear in the dermis. Keratin content is likely a big contributor to these peaks as it contains large amounts of cysteine.

dermis and dermis. 1300 cm^{-1} peak of lipids is also more defined in native skin SCs. These lipid peaks in some cases even allowed a rough estimate on the location of the SC/viable epidermis boundary (section 5.2.2). Other than this, the spectra from both sources visually resemble each other very closely. In section 5.2.1.1, the spectra from each sample were location-labelled based on H&E images (each spectrum was labelled as SC, epidermis or dermis). And several spectral features believed to be indicative of a particular layer were identified in the previous section using a small number of samples and visual observations. As the data set increases, Multivariate Analysis (MVA) methods can in some instances provide more non-subjective measures. It can also allow more of the data within the spectra to be employed in the analysis. This is particularly useful in cases such as this where there otherwise appears to be very little change in the spectra of native skin and engineered HSEs. Cluster Analysis (CA), groups like observations on the basis of the variables defined (the XY data forming the spectrum). The partition of data is unsupervised so it helps discover categories which are implicit in the data themselves. Figure 5.9 shows CA results on a data set comprising of spectra collected form two different layers (epidermis and dermis), and from tissue of two different sources (native and engineered). Here all dermis spectra are assigned to a single cluster, all epidermis spectra are assigned to a separate second cluster. The two clusters separate for tissue layer, but are not indicative of tissue source.

Principle Component Analysis (PCA) is a MVA method that helps visualise data. Data is projected down to a lower dimensional space based on the highest variation. The direction showing the largest variation is the Primary Component (PC1). Then the direction of the second largest variation orthogonal to the first is described by the second PC and so on. Where CA groups like observations, PCA re-expresses the data as a sum of these PCs and groups like variations. It is a purely descriptive technique that gives a view of the systemic variation in the data using fewer variables. In Figure 5.9, PCA was performed to reduce the data, same as used for CA, to a linear combination of 7 orthogonal variables. The scores plots show the distribution of data with respect to the PC it is describing. Here, PC2 is seen to cluster each layer separately whereas PC4 describes a variation between native and engineered samples. This PCA suggests that there is information contained in the data that allows the separation of both tissue layers, and source. But that the variation arising from compositional differences extending from layers exceed the variation due to tissue source (PC2 >PC4).

In fact, performing PCA over a data set of several HSE samples that contain spectra from: (i) three different skin regions (SC, epidermis and dermis), (ii) using two different lasers (532, 633 nm), (iii) on three different substrates (glass, quartz and CaF_2) and (iv) that were preserved using two different methods (cryo and wax embedding) shows that the bands used for layer identification cluster these layers separately despite even sampling variations. The PCAs in Figure 5.10 were setup over the spectral ranges 1760-1180 (Amide regions) and 985-600 cm^{-1}. These regions were chosen as they were sensitive to layer information and because they avoided some regions that show high variation that are due solely to sampling methods, such as substrate and wax interference (Chapter 4). For the amides PCA, PC2 separates the SC and epidermis from dermis spectra. Loadings plot for this PC suggest that bandwidths of Amide I, Amide II and collagen-related region of Amide III all contribute heavily to the separation of the dermis. Separation of the SC from epidermis spectra was not as clear cut. The lipid peak at 1300 cm^{-1} and bands at approximately 1576 cm^{-1} that represent nucleic acid residues appear to have an effect on the minor barrier between the SC and epidermis in PC4. 985-600 cm^{-1} region has little contribution from lipids, but contains large amounts of information on nucleic and amino acid vibrations. This region also gives good separation between the dermis and superficial layers of the skin, but more importantly, in PC3, it describes a variation that clusters the SC and epidermis apart form each other.

Tentatively, the PCA results suggest that the spectral signatures are very layer-specific and that fingerprint regions can identify the layers regardless of source or sampling method. This is tested here with another MVA method: Linear Discriminant Analysis (LDA). LDA is used for predicting classes of unknown samples by testing them against a reference data set whose sample categories are known. Like PCA, this involves reducing the dimensions of the data in directions where the variance is the greatest. But unlike PCA, the search for variation in LDA is supervised by the reference data set: the projection follows the direction that maximises class discrimination. This takes into account the standard deviation within classes and the variation(s) is chosen that projects samples of the same class close together but the means of each class far apart from each other. Table 5.1 shows the results of a LDA model that was built with epidermis and dermis spectra from both native and some HSE samples as a reference set. Several epidermis and dermis spectra from both sources were then tested against this model. The layer from which the spectrum was collected is predicted with 100% accuracy.

Table 5.1: Results of LDA classification. The models first training set was built with 30 spectra (epidermis and dermis) from the same sample matrix used for PCA. Layer assignments from 30 different spectra were removed and tested against this first training model. The sets were then reversed. Initial training set of 30 was de-classed and tested against the second training set built from the first test set of 30. In this way, all 60 spectra were run against the program. Prediction of layer from spectral features is accurate with a model that includes 4 different HSE samples (two wax, two cryo) despite sampling variations.

Predicted **Actual**	Epidermis	Dermis
Epidermis	60	0
Dermis	0	60

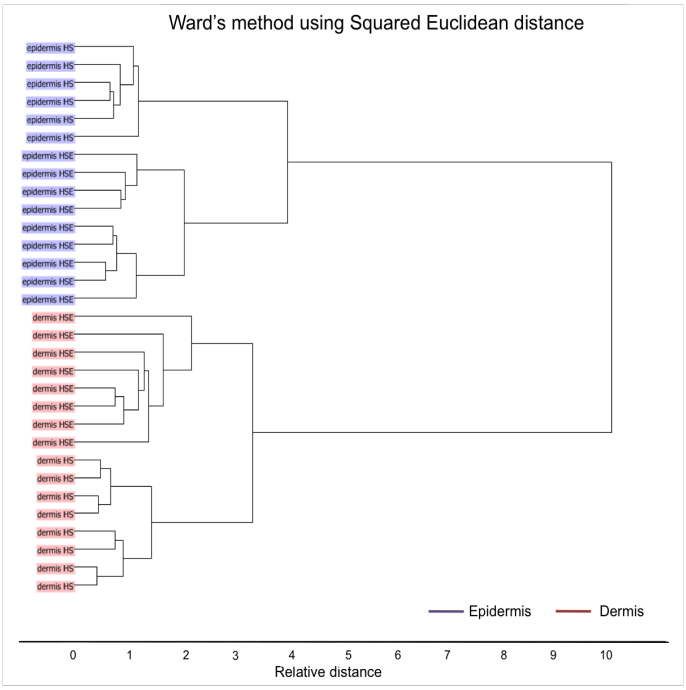

(a)

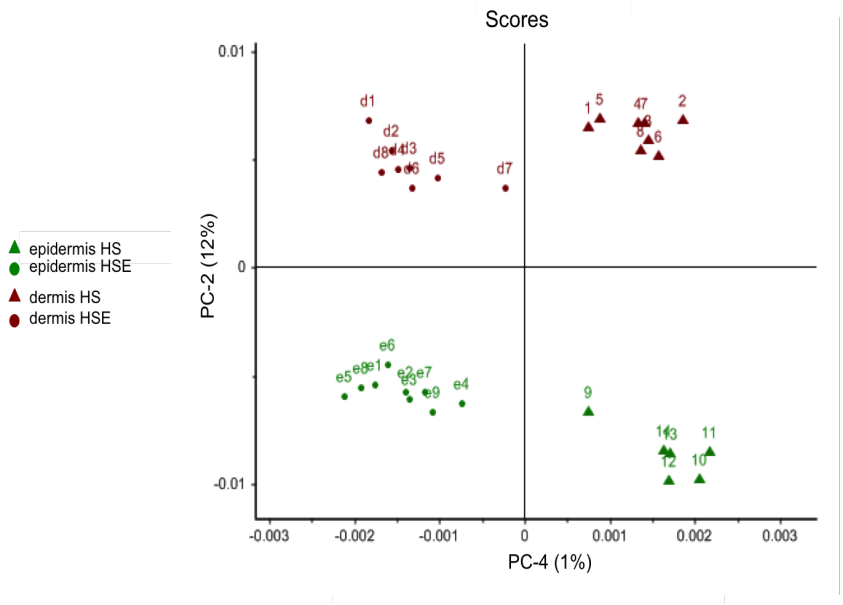

(b)

Figure 5.9: (a) CA results on native (HS) and engineered skin (HSE) samples. Despite two different sources, information contained in Raman spectra separate skin layers perfectly. (b) PCA results on the same data set used for CA. Scores plot highlights two PCs that together describe variations that separate both tissue layers and source. The biggest contributor to the separation of layers is Amide I and III (not shown). Loadings for PC4 is too complex to identify narrow regions that are more sensitive to source discrimination.

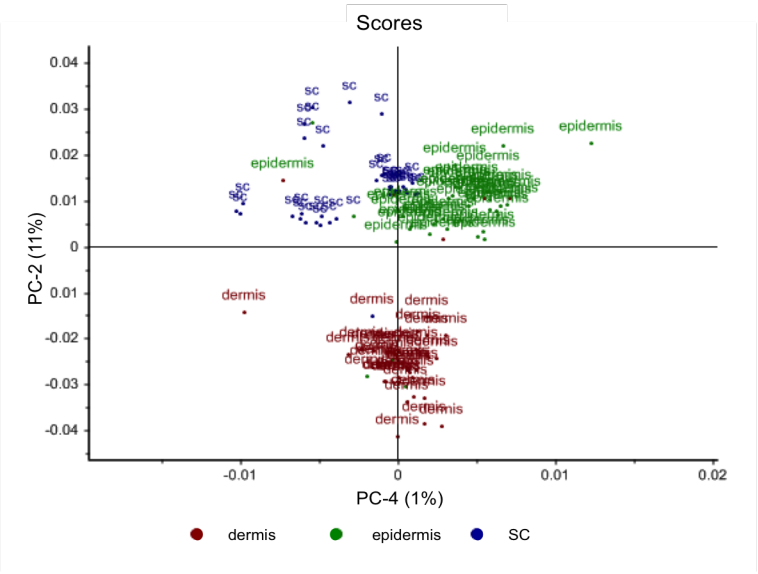

(a)

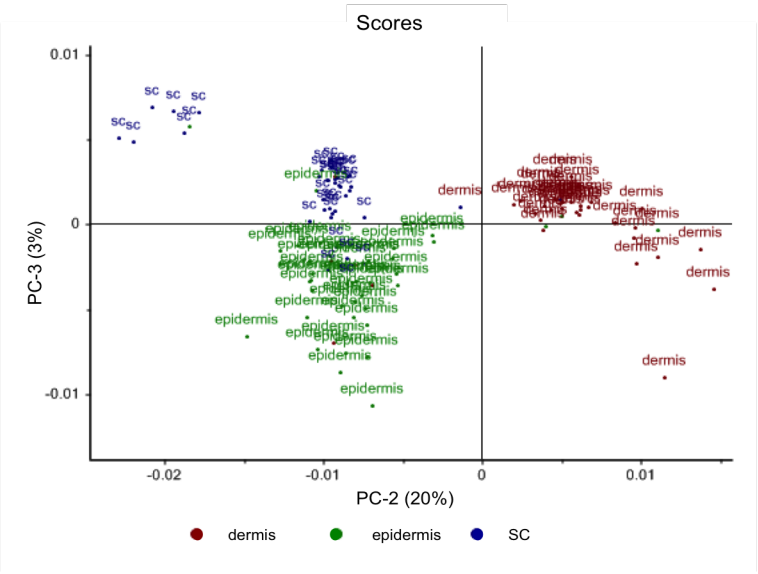

(b)

Figure 5.10: PCA results on data from several HSE samples that were preserved using two different methods (cryo and wax), sectioned onto three different substrates (CaF_2, quartz, glass) and collected using two different lasers (532 and 633 nm). The spectra were all UV normalised before analysis. PCA was performed on the 1st derivative spectra (to remove any baseline effects) and over the regions 1760-1140 cm^{-1} (a) and 985-600 cm^{-1} (b).

5.2.2 *In vivo* property estimation

Reliance on *ex situ* methods for measurements of quality and maturation is limiting: tissue fixation steps (i) can potentially alter microstructures. There are several fibrous proteins found in skin, such as collagen, elastin and keratin, that are highly resistant to acids, alkalis and temperature differentials. This is reflected in their ordered, repetitive structure but such a rope-like organisation also means they can be stretched and contracted. For example, keratin can double in length when soaked in water. The stretching may not only affect mechanical properties but also bond lengths and in turn, Raman signatures. This raises the practical question: how truly does Raman band assignments made through in vitro measurements match those from living systems? (ii) do not allow for kinetic measurements. This is a major obstacle in the automation and scale up of HSE growing processes that are in demand. Tissue culture processes require extensive in-line controls as the growth characteristics of a given cell line may differ significantly as bioreactors are scaled up even under identical process conditions. This section describes how spectral fingerprints differ in hydrated intact samples vs processed sections and how several spectral features identified in previous sections may be used to monitor epithelial layer maturation on HSEs while still in culture.

Some differences in protein structure between intact and sectioned tissues: A large shift is observed in the main protein band at 2930 cm^{-1} between the epidermis and dermis of sectioned tissues. This shift is more prominent in sectioned tissue compared to intact skins, Table 5.2. This might be due to one or more of the tissue processing steps of fixation. And it might be indicative of differences of protein conformation *in vivo* versus *in vitro*.

The position and bandwidth of the Amide bands are found to differ between fresh intact skin versus sections of processed skin. For intact, hydrated skin samples, the Amide I band broadens in the dermis but does not shift to the same scale as seen in sectioned tissues (Table 5.2). Difference in band maxima between the epidermis and dermis is approximately 14 ± 3 cm^{-1} in sectioned tissue compared to 5 ± 2 cm^{-1} for intact tissue. For sectioned tissues, it was hypothesised that the shift reflects a higher percentage of epidermal proteins in α-helical form compared to more unordered and β-sheet forms in the dermis. Along this line of reasoning, a high percent of dermal proteins in unprocessed intact skin are in α-helical form. In Amide III, β-sheet and unordered protein peak intensities were high in the dermis of sectioned tissue. The band

shape is different for intact skin: The relative intensities for 1267, 1248 and 1230 cm^{-1} peaks of collagen conformation are instead suggestive of more α-helical forms in intact skin. A downshift from α-helical to β-sheet may be associated with the stretching or reorganisation of the hydrogen bonded network of collagen [Gasior-glogowska et al. 2010]. And has been reported in collagen fibres under uniaxial stress [Gasior-glogowska et al. 2010]. It is possible that fixing and dehydration of the skin tissue causes a remodelling of the collagen network causing dermal proteins to downshift from α-helical to β-sheet. Amide II position is also of possible note. The position of the band maxima did not alter much between epidermis and dermis of tissue sections. The difference was minor with a shift of 2 ± 1 cm^{-1} between the means but a lot of inner and between sample variation was observed. In contrast to this, the position of this band in the dermis of intact tissue changed to a higher wavenumber, the shift was 4 ± 1 cm^{-1} between the means of each layer, Table 5.2. The difference in Amide positions is also observed between spectra obtained from hydrated DED and from the same DED after it dried out for 24-hours, Figure 5.11.

Table 5.2: Differences in protein band positions between processed and intact skin tissues.

Layer	2930cm^{-1} position	Amide I position	Amide II position
Cryo			
epidermis	2930.4 (2925.1-2931.4)	1654.3 (1651.9-1657.2)	1447.0 (1444.7-1448.0)
dermis	2939.1 (2927.7-2940.6)	1668.1 (1666.3-1670.7)	1448.8 (1446.7-1450.8)
Wax			
epidermis	2931.1 (2931.0-2933.0)	1653.8 (1652.9-1655.1)	1448.2 (1447.3-1448.6)
dermis	2938.2 (2937.0-2939.1)	1666.4 (1664.9-1668.0)	1449.7 (1449.3-1451.0)
Intact			
epidermis	2933.8* (2931.1-2934.8)	1653.9 (1653.2-1654.8)	1448.0 (1446.9-1448.3)
dermis	2938.5 (2938.1-2939.4)	1656.1* (1654.9-1657.0)	1451.6* (1450.0-1452.5)

Surface lipid profiles of intact HSEs: Lipid profiles of intact skin tissues closely match the trend seen in tissue sections. Figure 5.13 shows a depth profile from intact native skin to a depth of 80 μm. The region 3200-2600 cm^{-1} is deconvoluted into its component peaks of proteins and lipids (2980, 2930, 2880 and 2840 cm^{-1}) and the ratios I_{2930}/I_{2880} and I_{2930}/I_{2840} are charted versus depth. In both cases, they reveal a lipid-rich area that remains largely constant that is tens of microns thick (region A).

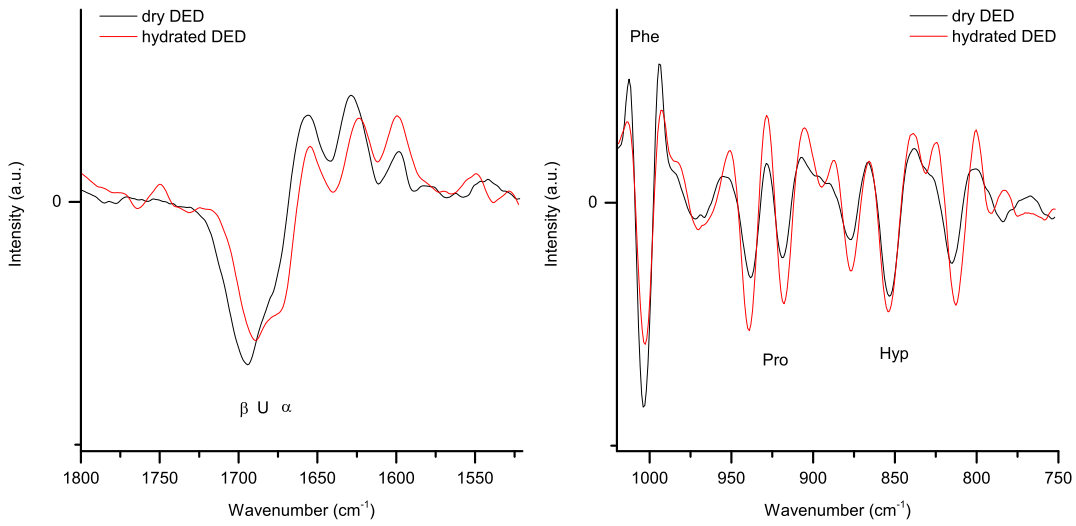

(a) (b)

Figure 5.11: Differences in protein vibrations between intact and processed skin tissue dermis. (a) 1st derivative spectra for Amide I (1760-1160 cm^{-1}) and (b) 2nd derivative spectra for 1015-700 cm^{-1} regions. The spectra were unit vector normalised. Amide I maxima shifts to a higher wavenumber after DED is processed (mixed conformations to predominantly β-sheet). Proline and hydroxyproline vibrations vibrations (920 and 855 cm^{-1}) are also much higher relative to Phenylalanine (1002 cm^{-1}) when DED is processed. Changes are likely due to effects of hydration on dermis structure.

The protein content is seen to increase steadily from this point on (Region B) before it reaches a protein dominant plateau (region C). These regions correlate well to the measured thickness of the SC (A), epidermis (B) and dermis (C) that were obtained using the H&E images of the same sample. The boundaries are readily identifiable in this instance, where SC ends at 12 μm, and dermis begins at approximately 70 μm.

However, lipid profiles from engineered HSEs were not so easily expressed. This is partly due to most of these samples not having SCs that were as well established as those seen in native skin samples. The 2880 and 2840 cm^{-1} lipid peak intensities were not as intense and a transition from Region A to Region B was not always observed. Instead, there was a sudden and sharp increase from an unbroken Region A/B (SC and epidermis) to Region C (dermis). HSEs also showed a lot more regional variation. For example, in some samples, optical microscope images of the HSE surface revealed features which differed in morphology and height. These were labelled as areas rep-

resentative of an abundant smoother surface (position A) and of pockets with a more compact almost aggregate like appearance (position B). Random locations that support both these areas were profiled. Figure 5.12. At position (A), intense peaks in the 2880, 1438 and 1300 cm^{-1} bands characteristic of lipids are absent. Likely indicating a lipid-rich matrix similar did not form in this location. The spectra share a much greater likeness to the Raman spectra of the epidermis compared to the SC. Having no prominent peaks of trans-phase lipids at 1060 cm^{-1} makes it likely that the region has limited barrier properties. At position (B), more prominent bands are observed at 2880 and 1300 cm^{-1}. The spectra in this region show peaks indicative of both trans-phase (1060 cm^{-1}) and unordered (1080 cm^{-1}) lipids. Presence of these peaks suggest a stratified layer that bear a close resemblance to a SC. This points to regional variations in lipid concentrations across the surface of some HSEs even after 14 days at the air/liquid interface. This might be due to culture conditions or under-maturation of the HSE. Maturation of the SC is in fact observed very well in samples that were grown for 7 days at the air-liquid interface versus those grown for 14 days. Figure 5.14 shows surface spectra from a day 7 HSE and a well-established day 14 HSE. In the 1200-1000 cm^{-1} region, a much larger amount of gauche lipids are found in day 7 compared to day 14.

Estimating thickness of the epidermal layer of some HSEs: Epidermis thickness from a day 7 HSE is estimated non invasively using two different spectral regions in Figure 5.15. Tracking two markers of collagen indicated the epidermis is approximately 50 μm thick. In contrast to this, the thickness of the epidermis could not be estimated for many of the day 14 HSEs used in this study. This was because the epidermis thickness exceeded the profiling depth. An example of this can be seen in Figure 5.16 where the dermal component is not reached even at 90 μm depth. And Figure 5.16 examples a profile from native skin. Approximations were easier in native skins as, for the two types of samples used here, the epidermis thickness was less than in-house grown HSEs.

In fact, a cross-sectional 2D plane of intact native skin was mapped successfully to visualise tissue layers. The grid in Figure 5.17 represents a Raman depth slice tracking the increase in the intensity of the area under 1267-1248 cm^{-1} band to the 1400-1300 cm^{-1} band. At approximately 60 μm depth, $I_{1267\text{-}1248}/I_{1400\text{-}1300}$ increases suddenly and sharply indicating a large increase of collagen in the collection volume. This pinpoints the location of the epidermal/dermal barrier.

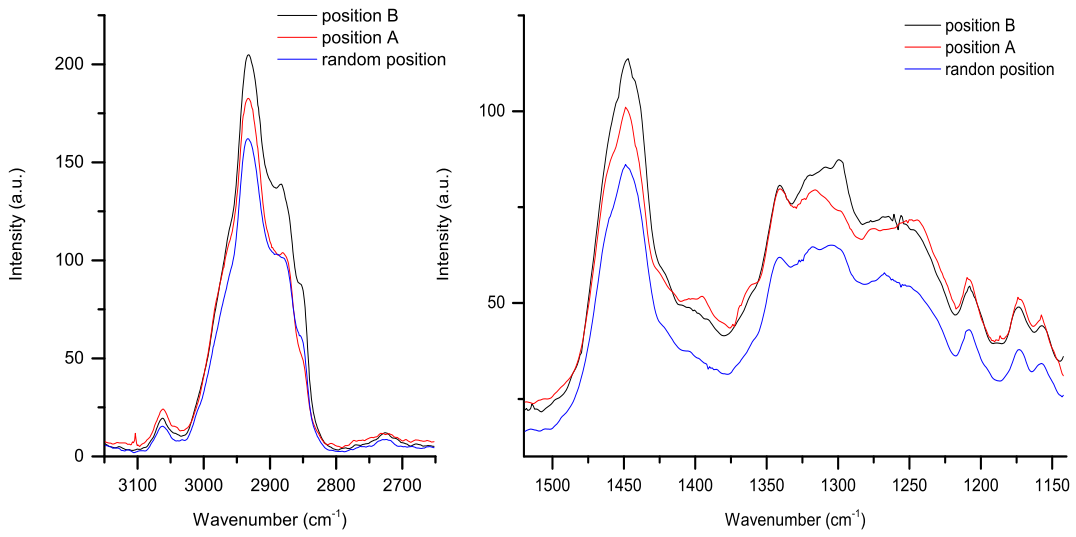

(a) (b)

Figure 5.12: Variations in the surface lipids of some HSE samples. Intact skin raman spectra from (a) High-wavenumber region lipids (3200-2600 cm^{-1}) and (b) fingerprint lipids. Lipid composition is different in two separate regions of the same HSE sample. Compared to position B, lipid content appears to be much lower in position A. A full lipid bi-layer has not formed on the entire HSE surface.

5.3 Discussion

In this study Raman measurements were carried out on intact skin tissue to study the molecular conformation of compounds in their natural micro environment and to see how this correlated with measurement obtained from processed tissue. It was shown that it is possible to obtain information on the lipid and protein structures and use them to separate the skin layers.

Lipids: In native skin and HSEs, measuring the lipid packing within layers is important. It means HSEs can be compared to native skin with regards whether or not a similar barrier is formed and maintained. HSEs which can mimic this property are more useful in the pharmaceutical and cosmetics industries as the way in which some topically applied drug or cosmetic formulations access deeper tissue layers is by altering the lipid packing from trans-gel to liquid-crystal [Förster et al. 2012]. Resolving both the tissue layers and change in lipid packing after application may allow more detailed investigations into how these formulations interact with the skin layers [Bonnist

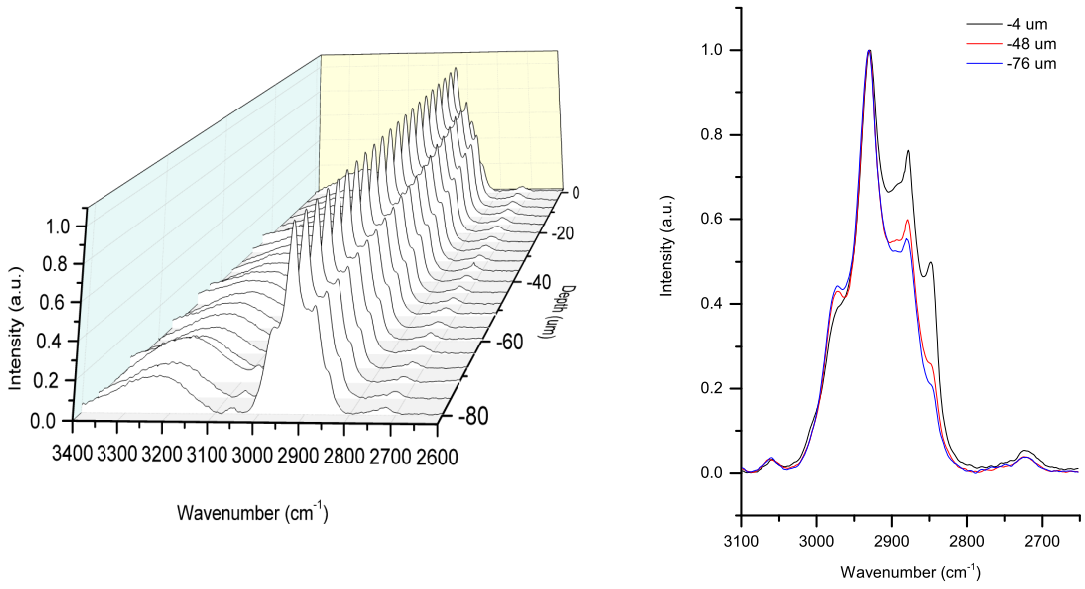

(a) (b)

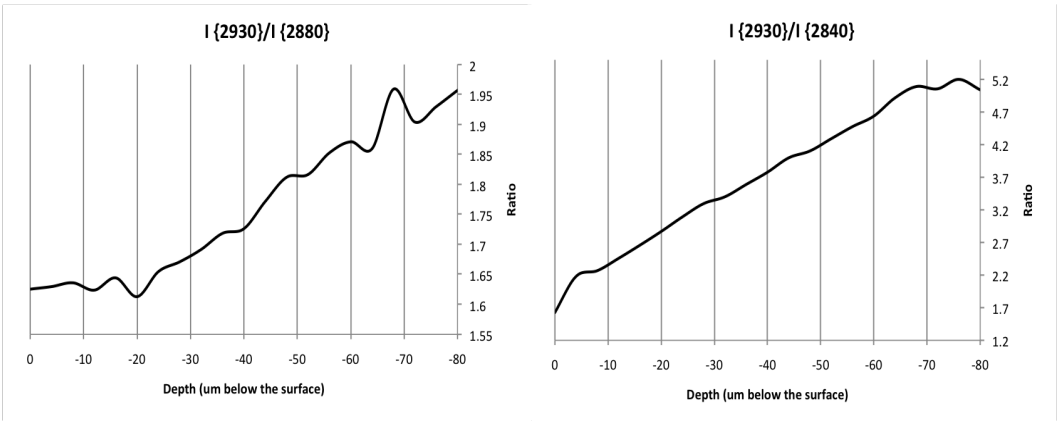

(c) (d)

Figure 5.13: Lipid profile of an intact native skin sample. (a,b) Raman spectra of the highwavenumber region (3200-2600 cm^{-1}) at different depths. (c,d) I_{2930}/I_{2880} and I_{2930}/I_{2840} tracking protein-to-lipid ratio of intact skin down to 80μm below the surface.

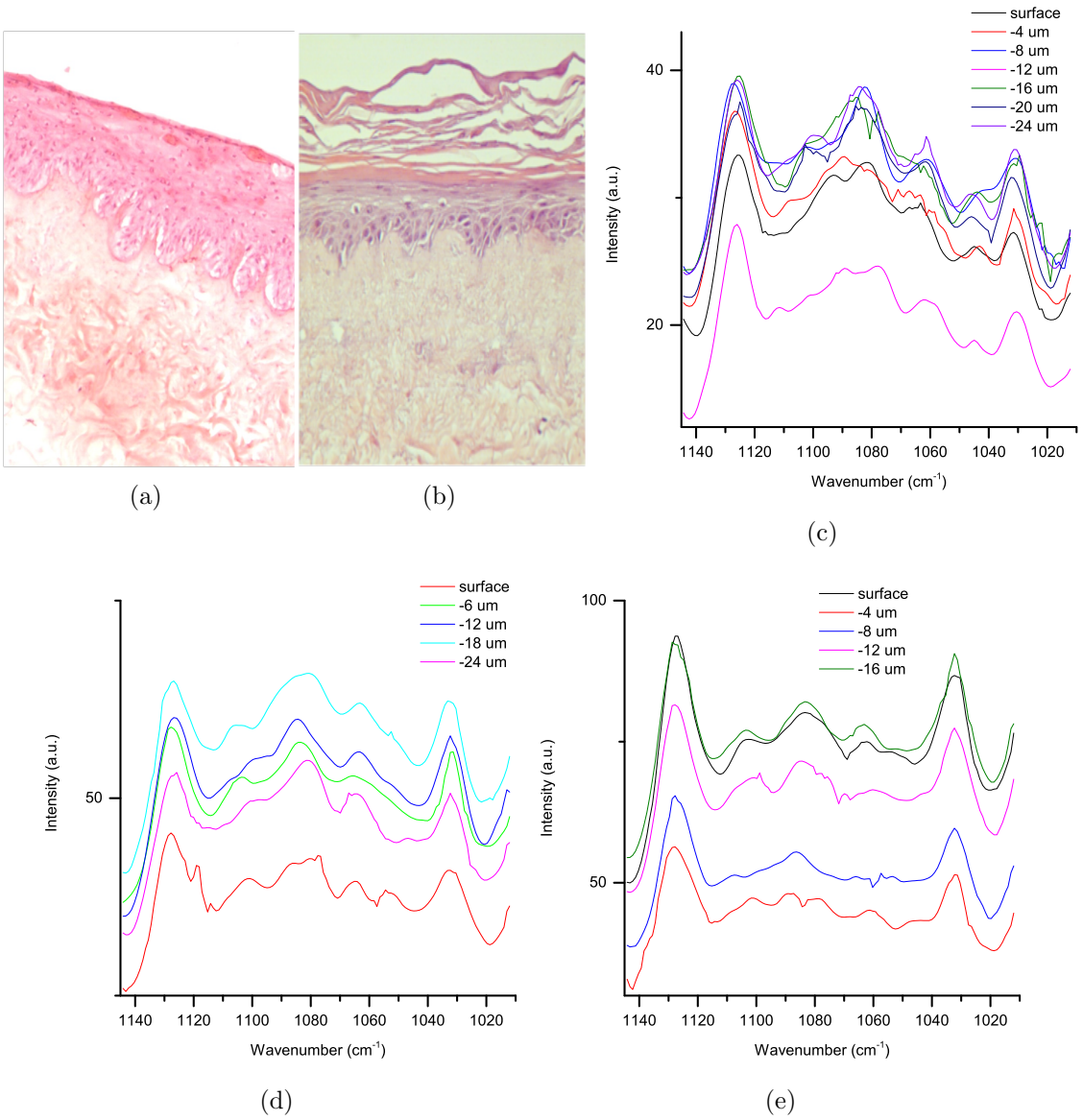

(a) (b) (c) (d) (e)

Figure 5.14: Surface lipids of intact HSEs in culture. H&E stained section of day 7 (a) and day 14 (b) HSEs. (c) Raman spectra from the surface down to 24 μm below the surface of a day 7 HSE. (d,e) Raman spectra from the surface down to 24 and 16 μm below the surface of a day 14 HSE (positions A and B from Figure 5.12 respectively). The profile collected at position A contains more gauche lipids compared to a second position B. The lipid layer has not matured in position A as it bears a much closer resemblance to the lipid phase spectra of day 7 HSEs. Lipid pockets like these were common in HSEs.

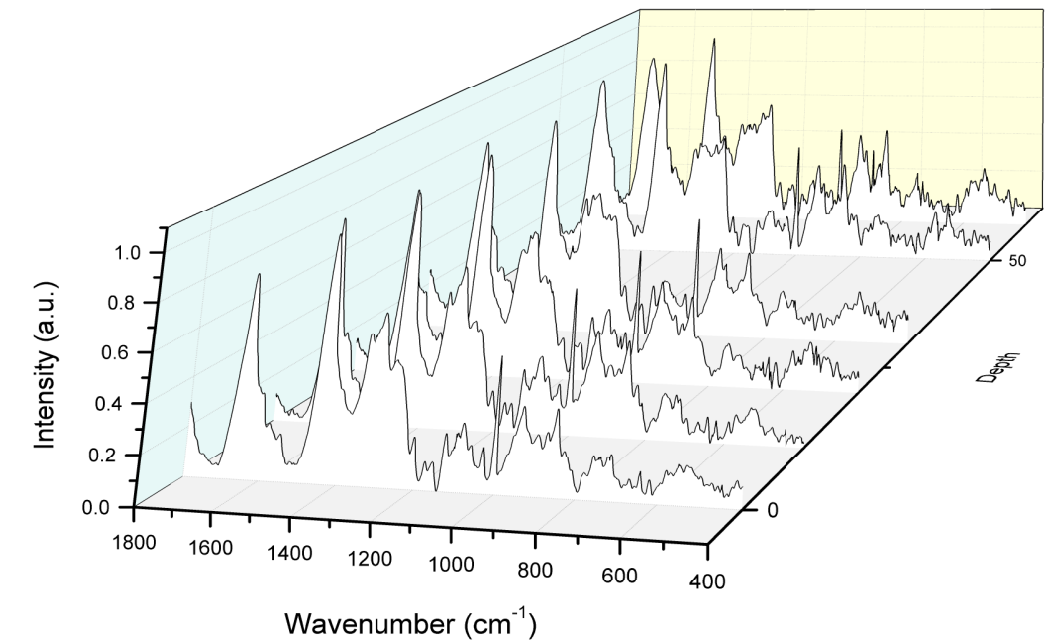

(a)

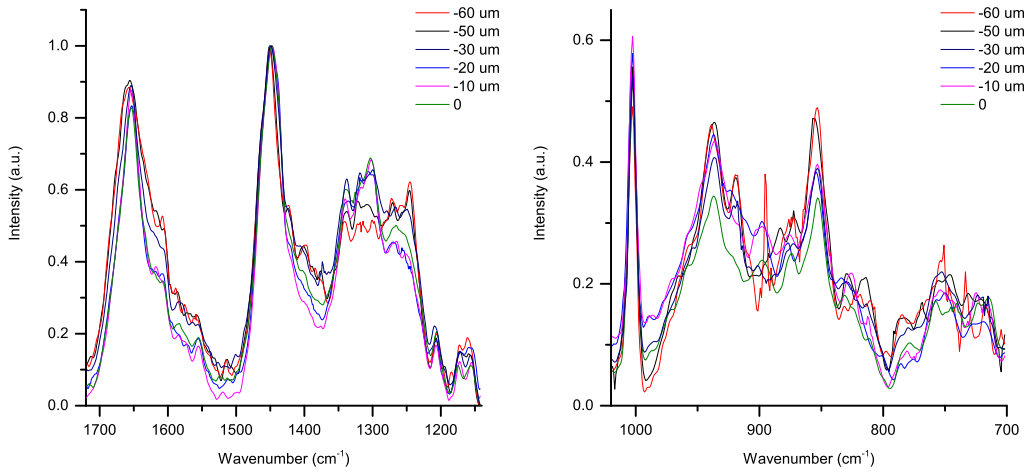

(b) (c)

Figure 5.15: Raman depth profile of a day 7 HSE while in culture. (a-c) Raman spectra from the profile at different depths. Markers of collagen begin to appear at 60 μm below the surface - Amide I widens, collagen peaks of Amide III become more intense compared to 1400-1300 cm^{-1} and proline peaks increase relative to phenylalanine). Epidermis thickness can be estimated to be at least 50 μm from this non invasive profile.

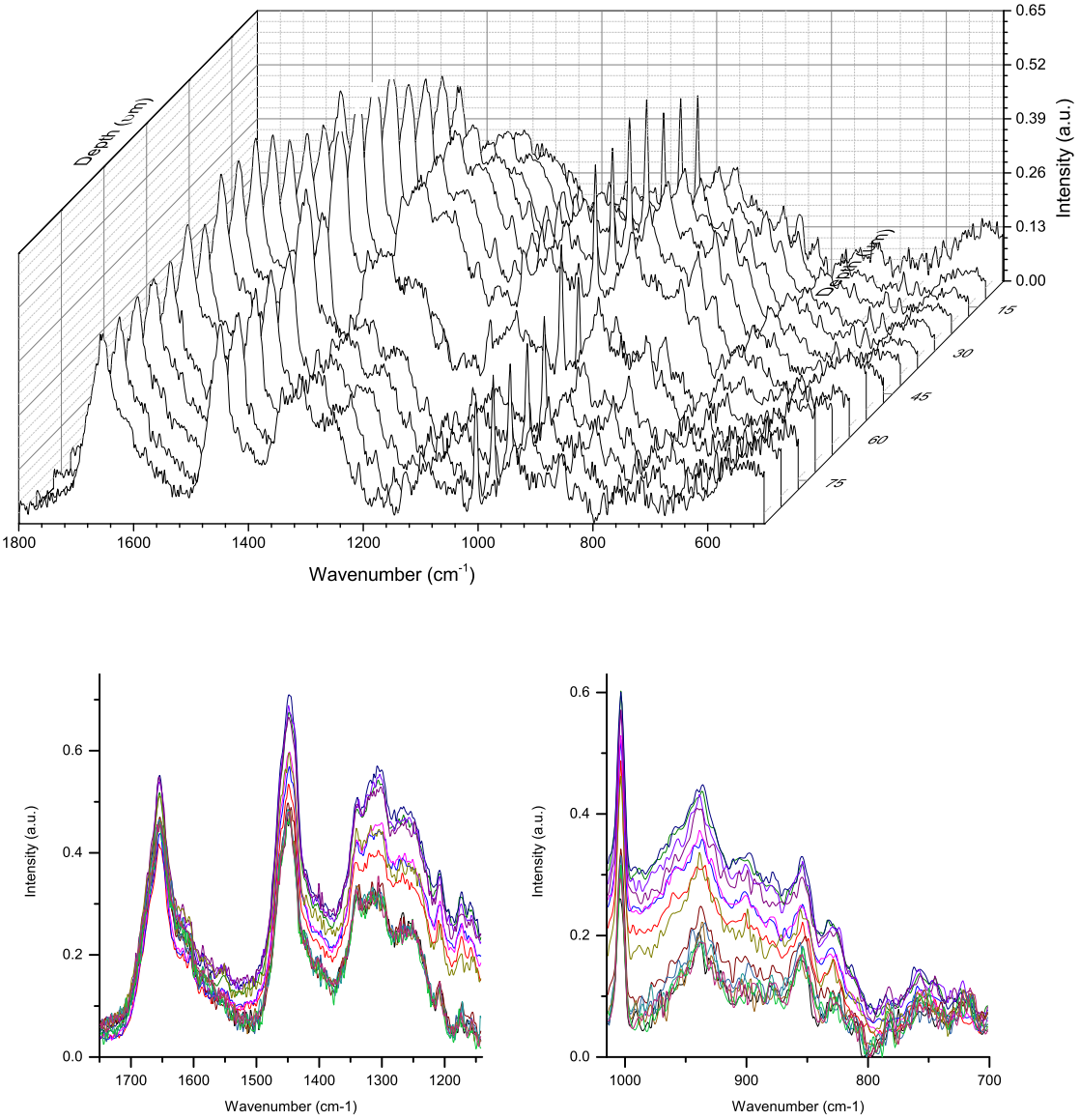

Figure 5.16: Raman depth profile of a day 14 HSE while in culture. (a-c) Raman spectra from the profile at different depths. No markers for collagen are observed at even 90 μm below the surface. The epidermis is estimated to be over 90 μm thick and lipid markers indicate a thick lipid-by-layer has formed.

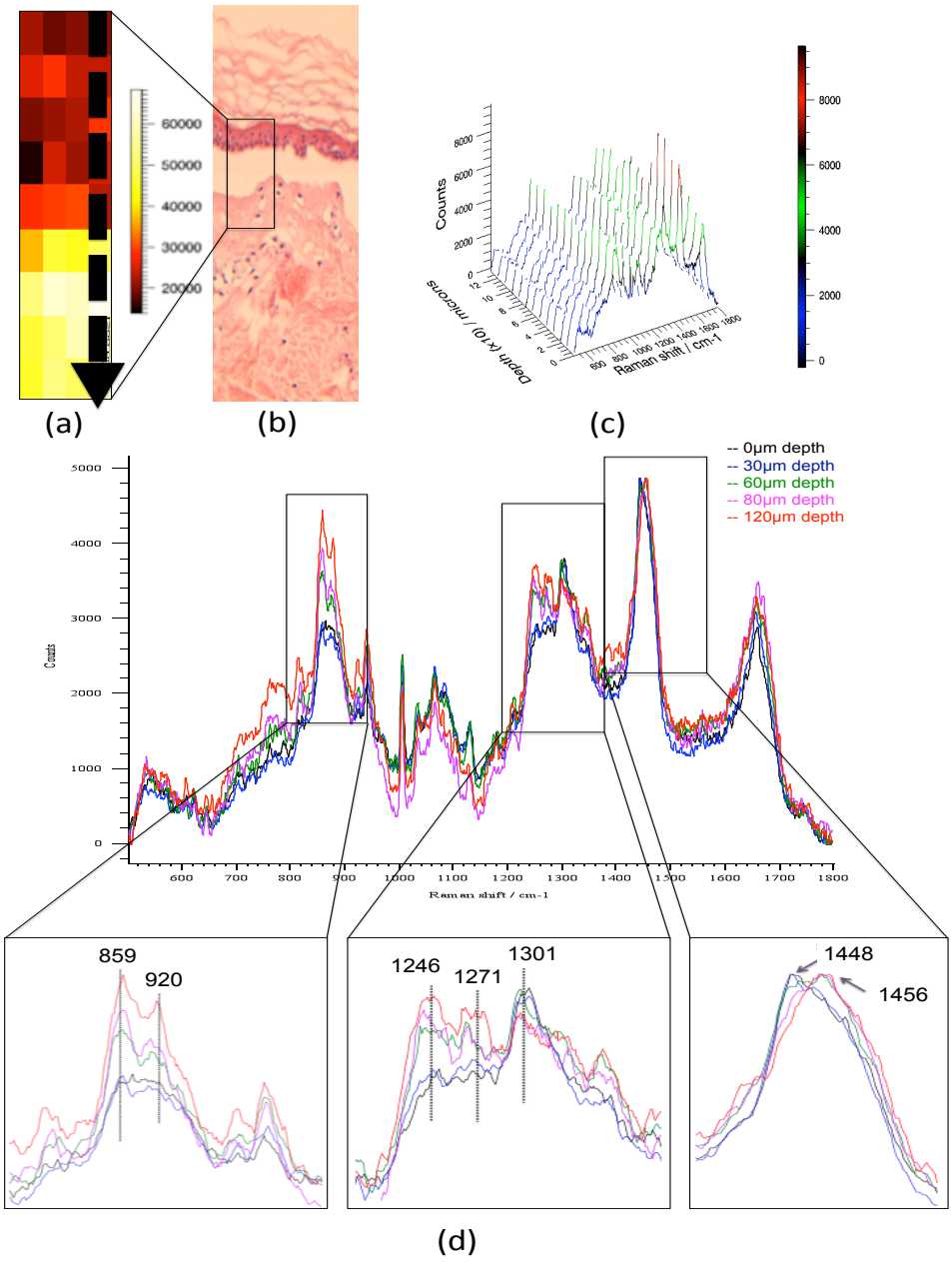

Figure 5.17: (a) 2D depth slice of human skin tracking the change in the 1400-1200 cm^{-1} band of collagen (intensity of area below 1300-1200 cm^{-1} relative to 1400-1300 cm^{-1}). Using only this region, epidermis thickness is estimated to be approximately 60 μm. (b) H&E stained section of the same sample after being processed. (c-d) Height profiles corresponding to the dashed line extracted from the map grid. Collagen markers are apparent between 60 and 120 μm below the surface with 785 nm excitation.

et al. 2011b, Broding et al. 2011]. Pertinent too because many commercially available HSEs are reported to have poor barrier properties, and that factors such as temperature and humidity affect the quality and formation rate of SCs in culture [Hoath, Tanaka, and Boyce 1993, Nolte et al. 1993]. For example, compared to native skin, expression of some differentiation markers such as involucrin, and keratins 6, 10 and 16 have been shown to be different in HSEs. Involucrin was found in all suprabasal layers instead of only in granular layers. Whereas keratin varied from its expression in all suprabasal layers (previously associated with wound healing [Mansbridge and Knapp 1987]) to gradients along the thickness of the epidermal layer [Boelsma et al. 2000, Banks-Schlegel and Green 1981]. It is suggested that these markers indicate an activated epidermal layer, and normalising its expression might improve barrier properties of the SC [Thakoersing et al. 2011]. The percentage of each of the three lipid classes of the SC, ceramides, cholesterol and free fatty acids, are also different in HSEs. The percentage distribution of these lipid classes can be altered with additional ingredients in the cell culture media to allow optimisation of barrier forming abilities. Vitamin C for example has been shown to increase the amount of ceramides and form lamellar structures more closer to native skins [Ponec et al. 1997]. Conditions that may improve SC properties and tools that can measure them command attention.

There are several methods employed in the study of SC lipids. Many of which require isolation of the SC from intact skins for lipid composition and organisation (e.g. High Performance Thin Layer Chromatography). Or immunohistological analysis for studying differentiation markers. Here, using RS, spectral ranges between 3400-2800 and 1200-990 cm^{-1} were used to study the lipid content and phase. We were able to establish the presence (or lack thereof) of a lipid-bi-layer on HSE surfaces both *in vivo* and *in vitro*. And based on the conspicuous lipid peaks between 3400-2800 cm^{-1}, that lipid content between native and HSE tissues are different. This is despite the HSEs being made from cells isolated from the same native skins. The region 1200-990 cm^{-1} revealed the surface of day 7 HSEs are dominated by gauche phase lipids compared to mature day 14 HSEs which had a combination of both trans and gauche lipids. However, while the method is very descriptive for small collection volumes, measurements made from a single location did not always hold true for the entire sample because lipid packing within HSEs showed a lot of regional variation. For example, some day 14 HSEs had localised lipid pockets instead of a continuous lipid layer. Gauche lipids are associated with increased permeability. HSEs in general are found to be more permeable, sometimes by a factor five [Thakoersing et al. 2011], compared to native skins.

Ability to ascertain the presence and phase of the SC on these mixed surfaces or its transition (from gauche in early-stage to trans/gauche) while in culture is an advantage. In fact, it is suggested that correlation between the ratio I_{2880}/I_{2840} and phase transition is comparable to differential scanning calorimetry (DSC) [Wegener et al. 1996]. DSC gives very detailed information on the phase transition temperature, its rate of change and the magnitude of transition but requires SCs to be separated and/or use of solvents to extract lipids for analysis. Results from extracted lipids do not always agree with isolated thin SC layers [Silva et al. 2006]. Whilst RS data is not as detailed, the measurements were taken in-line, from SC layers still in their natural state. And due to high spatial resolution, lipid profiles across epidermal layers are measured. This does not give an actual quantitative value for lipid content at each point, but allows relative concentrations to be tracked against depth. Profiles from native skin samples with confirmed, water-tight barriers can then be used as baselines from which the quality HSEs may be assessed.

Proteins: In the high wavenumber region (3200-2600 cm^{-1}), the proteins of the SC and epidermis were found to be highly folded compared to the dermis. For intact skin, the unfolding in the dermal layers seemed to correlate with the increase in hydration. The less hydrated upper layers function as the primary barrier to the environment which might explain the design of the highly folded protein structures. In such conformations, the proteins can form little interaction with external compounds forming an effective boundary. In the dermal layer the protein is freer to form bonds with other molecules such as water. The bonding with water strengthens and stabilises the layer due to the network of hydrogen bonds created.

The amide bands were found to have considerable differences between layers of the skin (epidermis and dermis) and between intact and sectioned skin. Interpretation of these changes is difficult due to mode mixing as many of the tissue constituents have overlapping peaks and bands here. Amide I position suggests that proteins of the SC and epidermis are predominantly in α-helix form, both *in vivo* and *in vitro*. But individual proteins can rarely be identified against a background of other proteins. Instead, the bands are used to ascertain information on the overall protein content. An exception is perhaps the dermis. Over 75% (wt) of the dermis is collagen. So changes in the dermis spectra are tentatively assigned to collagen related effects. For example, here, the shift observed for Amide I in sectioned tissue is thought to point to a large portion of dermal proteins taking Unordered and β-sheet form. The big difference in

the position between intact and sectioned dermis is a shift toward lower wavenumbers suggesting that *in vivo*, a high percentage of dermal proteins are in unordered and α-helix form. This is perhaps indicative of a dependency of hydration on collagen conformation because the effect is also observed in the spectra collected from hydrated DED samples versus from dried DED samples. This is also observed in some Amide III bands where the percentage distribution of α-helix, unordered and β-sheet peaks vary between intact, wax embedded and frozen samples. Assuming hydration is the main cause of this effect, a clue also comes from the Amide II band. This band is not seen to shift to a statistically significant extent in sectioned tissues (position shift is close to system resolution) compared to intact samples where the shift is 4 $\pm$1 cm^{-1}. Seen altogether, in hydrated samples Amide I shifts to a lower wavenumber while Amide II shifts to a higher wavenumber. Downshifts in Amide I position are reported in proteins as they become more stable [Myshakina, Ahmed, and Asher 2008]. Backbone stability would decrease the frequency of υ(C=O) vibrations (Amide I) but increase the frequency of δ(C=O) vibrations (40% Amide II). More importantly, stiffness of the backbone would increase the frequency of vibrations from side chains as their conformational freedom is not restricted. Collagen is mainly made up a sequence of glycine, proline and hydroxyproline. Glycine is a big part of the backbone accounting for every third amino acid in the sequence. It is neutral compared to proline and hydroxyproline which are hydrophilic. The structure of collagen is very sensitive to hydration because it depends on water bridges formed between hydrophilic counterparts to the peptide links [Bella, Brodsky, and Berman 1995]. Water molecules are trapped within the helical lattice effectively holding the 3d structure by binding the triple helices. Based on the spectral features just mentioned, an ad interim theory might be that: frequency of collagen backbone stretching vibrations (υ(C=O)) decrease in water bound collagen (stiffer structure) but the frequency of bending vibrations of the carbonyl oxygen atoms (δ(C=O)) that are close to water molecules and the bending vibrations of the peptide-peptide hydrogen bonds (δ(N-H)) increase (assuming these arise from side chains whose conformational freedom is restricted due to water bonding). To note also is the increase in proline and hydroxyproline peak intensities (920 and 855 cm^{-1}) relative to phenylalanine in hydrated samples. This altogether makes sense as in hydrated samples, more of these hydrophilic side groups are probably revealed.

Layer characterisation: Here, PCA showed that variations due to layer composition is greater than both source and sampling variations. In both the 1760-1180 and 985-600 cm^{-1} regions, the variations described by the PCs cluster each of the tissue layers

(epidermis and dermis) separately. In the amide region, it was noticed that lipid and nucleic acid residues contributed to a slight separation between the SC and epidermis. Lipid content was found to vary within and between samples with separate analyses. The PCA for 985-600 cm^{-1} was set up because of this as the region has little contribution from lipids. As such, the clustering in the scores plot is almost entirely due to differences in nucleic and amino acid vibrations in the layers. Very little work is done on this region making it difficult to attribute this separation to any particular NA or AA. However, that SC spectra can be dissociated from epidermis spectra suggests the composition of NAs and AAs in SC maybe used to detect SCs layers even in the absence of mature lipids.

In vivo profiling: This work has presented some structural information of proteins and lipids extracted only from Raman data. The information is not as detailed as those that maybe obtained through techniques that are established in the study of these biological materials. A big drawback is that for much of these materials, Raman data has not been correlated with particular states, it still requires complementary tests to be carried out in order to be more descriptive for studying individual species such as proteins or lipids. An advantage lies in its ability to provide little information on *all* of these species by itself without dyes and in their natural state. This makes it a great tool to adapt for monitoring tissues for general quality purposes. Here, using 2D cross-sectional Raman maps with 785 nm excitation and single point depth profiles using 633 nm excitation, the boundaries of the epidermal layer were identified under both sterile conditions and reasonable time-frames. This might prove invaluable in monitoring the maturation of HSEs in culture and in assessing how culture conditions affect the formation of each layer. In applied research, ability to measure the thickness of the epidermal layer would be useful for any topical application that must diffuse into the dermal layer. Such as tracking the absorption of trans-dermal pain creams. Or fewer samples would need to be sacrificed for time-resolved studies of factors affecting growth patterns. In clinic, estimating the thickness of epidermal layer would be useful in so far as a particular thickness can be linked to successful graft adherence. For example, the point at which a graft has a significantly better percent chance of taking when grafted onto patients. Whereas in manufacturing (large-scale HSE production), product consistency is dependent on the ability to control reactor environments to suit the conditions optimal for each new batch. Particularly because cell behaviour can be different even under identical process conditions. Batch turnaround times can be improved upon with measures from which rates of skin maturation can be obtained.

As well as the product, there are several examples where RS has been used to measure various rate limiting factors in bioreactors. For example, it has been used successfully for in-line monitoring of mammalian cell culture bioreactors over long reactor runs [Moretto et al. 2011, Li et al. 2010] and over different sized calibration sets [Abu-Absi et al. 2011]. In most cases, predicted glucose, lactate, glutamine, glutamate, ammonium and viable cell densities compared well to ex-situ measurements. Despite the potential, several obstacles remain for any of these advancements to be made. Sample-to-sample variation remains large. Dermal components are identified with ease in all samples but profiles from each sample required different types of processing: there was no standard setting that worked for all samples. The spectral features are also only shown to work for normal skin samples (native or HSE). Namely, markers for collagen and relative lipid-protein concentrations. Many disease states of the skin cause changes to these structures.

5.4 Conclusions

Several spectral features that provide some indication as to the quality of HSEs *in vitro* and in culture are explored in this chapter. Spectral differences arising from compositional and structural differences between skin layers are found to be sufficiently large to outweigh sampling variations (between HSEs, or HSEs and native skins) in normal skins. Layers are identified, barrier properties are assessed and some effects of hydration are observed on dermis structure. Prospects for monitoring (these features) maturation of HSEs in culture are good, but reproducibility of *in vivo* profiles were lower compared to those obtained from tissue sections. These were only successful 50-60% of the time. However, the quality of spectra obtained from the successful profiles were almost comparable to *in vitro* data.

Chapter 6

Melanoma

6.1 Introduction

Features used to diagnose and study melanoma varies greatly in scale from tissue level properties down to DNA level (Chapter 1). Type and drawbacks also vary. For example, sensitivity and specificity of histopathological features can change depending on several factors such as subtype and lesion size [Urso et al. 2008]. Overall, using a combination of features is typically very accurate in identifying subtype and in prognosis. But it is also subjective. In any given sample set, there may be no unanimous agreement by pathologists on up to 40% of melanoma samples [Farmer, Gonin, and Hanna 1996]. Melanoma markers are as variable. Some are more accurate in certain subtypes or locations (e.g. Melan-A is not as sensitive to non-cutaneous melanoma). Many of them are used in conjunction with histopathological features as very few markers have prognostic significance independent of factors such as thickness (e.g. p16, MMP-2). Markers are particularly useful in evaluating patients that need aggressive treatment who otherwise might be considered low-risk based on histopathological features alone [Larson, Konat, and Alani 2009]. For example, 5-year survival can decrease significantly for patients who are MMP-2 positive (<34%) versus negative (>34%) [Väisänen et al. 1998]. Increasingly, a number of oncogenes are being studied to refine classification and for their prognostic value. The activation of mutations cause disruptions to downstream proteins (e.g. uncontrolled receptor tyrosine kinase activity with BRAF mutations) which also make them suitable for targeted therapeutics.

Promising treatment options are emerging with the increase in trials for targeted therapies (e.g. BRAF inhibitors) and immunotherapies. Still, there is much to learn about

the mechanism of progression. For example, the prevalence of BRAF mutations in melanoma lead to trials with BRAF inhibitor drugs that in some cases have been very successful. And yet, as many benign nevi (80%) have BRAF mutations [Uribe, Wistuba, and González 2003]. Transformation into malignant state involves multiple (likely concurrent) steps including strong non-genetic components [Huang, Ernberg, and Kauffman 2009]. It is suggested that changes to the microenvironment may direct initial transformation as well as promote progression and invasion following transformation [Bissell and Radisky 2001, Tlsty and Coussens 2006]. Compositional and structural information from RS data may provide some information on aspects of tissue change during these stages that may compliment other data used in melanoma research. This chapter outlines some preliminary observations made on the differences between tissue engineered normal skins and tissue engineered melanoma models made with A375SM and C8161 melanoma cell lines.

6.2 Results

6.2.1 A375SM type melanoma composites

Sample features of A375SM models were divided into three categories based on the commonest morphological feature, Figure 6.1. These were: (1) areas with clusters of assumed A375SM cells encapsulated within epidermis, (2) areas with assumed A375SM cells spread over the composite surface and (3) areas bearing close resemblance to normal skin. A375SM cells have been reported to present as balls of cells within the epidermis of TE models previously [Eves et al. 2003].

6.2.1.1 Regional variations in Category 1 areas using PCA

Five large areas from three A375SM samples were picked to study compositional differences in clustering regions. The areas were around 200-300 μm^2 in size. Each area included a tumour cluster with defined borders that could be separated from surrounding tissue. Every spectra from these areas were location-labelled and then colour coded for: (i) tumour cluster, (ii) epithelial tissue surrounding the cluster and (iii) dermis. PCAs for two of these areas are presented in Figures 6.2, 6.3 (see Appendix for others). For each case, the scores plots contain a PC that separates dermis from superficial layers and a PC that separates tumour clusters from surrounding tissue.

PCs that separate dermis from superficial layers include features related to collagen

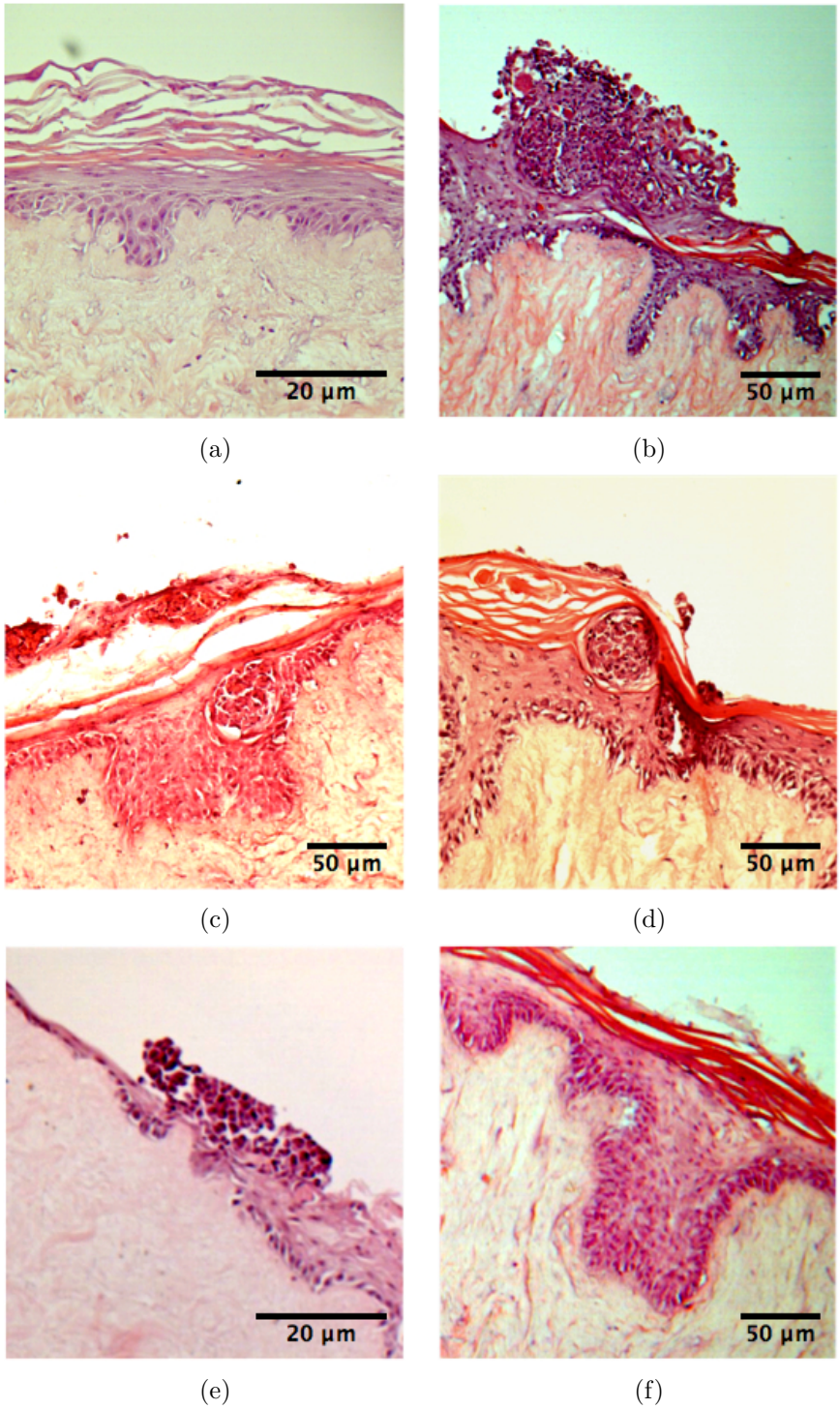

Figure 6.1: H&E of A375SM melanoma models showing three morphological categories: (a) normal HSE, (b-d) A375SM cells in clusters within the epidermis, (e) A375SM cells spread over the surface of the composite, and (f) areas that look almost like normal tissue engineered skin.

(1300-1140 cm^{-1} and 920, 855 cm^{-1}), nucleic acid (NA) residues (1400-1300 cm^{-1}) and lipids (1140-1060 cm^{-1}), Figure 6.2c, 6.3c. Many of these bands have already been discussed in Chapter 5 and bear close resemblance to features that separate these layers in normal skin (Chapter 5, Figure 5.1). Loading plots for PCs separating tumour clusters from surrounding tissue describe variations relating to differences in Amides and lipid phases as well as some significant contributions from glycogen and amino acid (AA) residues. Some of these features are highlighted below.

Differences in protein structure within A375SM clusters: Position of Amide I maxima in normal skin SC and epidermises described predominantly α-helical proteins in these layers and β-sheet proteins in the dermal layer (Chapter 5). For A375SM models, dermis spectra still suggests β-sheet proteins and epithelial layers both surrounding tumour clusters and further away both describe a high percentage of α-helical proteins. A difference is observed in spectra collected from within tumour clusters: Amide I maxima here is suggestive of more unordered and β-sheet conformations instead of α-helix (Figures 6.4a, 6.4b). This is seen consistently in all clear/defined tumour clusters within the viable epidermis, indicating minor conformational alterations in the proteins of these A375SM cell clusters.

Higher percentage of gauche lipids in A375SM models: In normal skin, near equal contribution of both trans and gauche lipids were observed in the viable epidermis of most HSEs (Chapter 5). In contrast to this, contribution from gauche lipids are higher in A375SM clusters, high density A375SM cells spread over the surface (category 2 areas) and in epithelial tissue further away from the clusters (category 3 areas). The biggest difference is observed at the surface where trans-to-gauche ratio is much lower compared to normal skin SC, Figures 6.4c, 6.4d, Table 6.4.

Increased glycogen presence in tissue surrounding A375SM clusters: A notable difference between the epidermis surrounding A375SM clusters in these models and normal skin epidermis is a peak at 481 cm^{-1}, Figure 6.5. This peak represents skeletal deformation of glycogen [Konorov et al. 2011]. It is found in areas around clusters but not in normal looking epidermis spectra far away from clusters or epidermis spectra in areas with A375SM cells spread over the surface. This suggests localised glycogen accumulations in epidermal cells in the vicinity of tumour clusters possibly in response to a foreign body within the area (whole epidermis is not activated). The storage response appears to be active at least to a range of 100 μm from clusters.

Differences in AA residues: Peaks attributed to Tryptophan (Trp), Phenylalanine (Phe) and Tyrosine (Tyr) show apparent sensitivity toward separating tumour areas from surrounding tissue. The differences are summarised in Table 6.1. The ratio I_{1360}/I_{1340} from the Fermi doublet of Trp is considered a marker for its configuration within proteins [Harada, Miura, and Takeuchi 1986, Takeuchi 2003]. It details whether the Trp chains are exposed ($I_{1340} >> I_{1360}$) or folded within the protein ($I_{1340} > I_{1360}$). In normal skin, the ratio is lower in SC compared to epidermis. This reflects hydrophobicity in the SC: Trp chains aren't accessible to water molecules as they are folded within the protein. Tumour clusters exhibit this same configuration even when the cluster is within the viable epidermis. Another Fermi doublet is seen at 850 and 830 cm^{-1} that arises from vibrations of the phenolic ring of Tyr [Siamwiza et al. 1975, Barry, Edwards, and Williams 1992]. Tyr chains are exposed and free to form intra-molecular bonds when the ratio I_{850}/I_{830} is approximately 10:8. Changes to this ratio reflects changes to the ionization state of this AA. Relative intensity of 830 cm^{-1} increases within most cluster areas describing buried Tyr chains. The two AAs together possibly suggest hydrophobic behaviour in clusters of A375SM cells.

Table 6.1: Amino acid peaks of significance in A375SM category 1 areas based on PCA

Peak (cm^{-1})	Assignment	Observed effect
1604	δ(C=C) of Phe, Tyr [Notingher et al. 2002]	Higher inside clusters compared to surrounding tissue.
1360	Ring breathing mode of Trp [Miura, Takeuchi, and Harada 1989]	Higher inside clusters.
1340	Ring breathing mode of Trp [Miura, Takeuchi, and Harada 1989]	Higher in cluster surrounding tissue.
1210	υ(C-C_6H_5) Tyr, Phe, Trp [Nijssen et al. 2002]	Higher inside clusters.
850	Ring breathing mode of Tyr [Notingher et al. 2002]	Higher in cluster surrounding tissue.
830	Ring breathing mode of Tyr [Notingher], υ(O-P-O) [Nijssen et al. 2002]	Higher inside cluster.

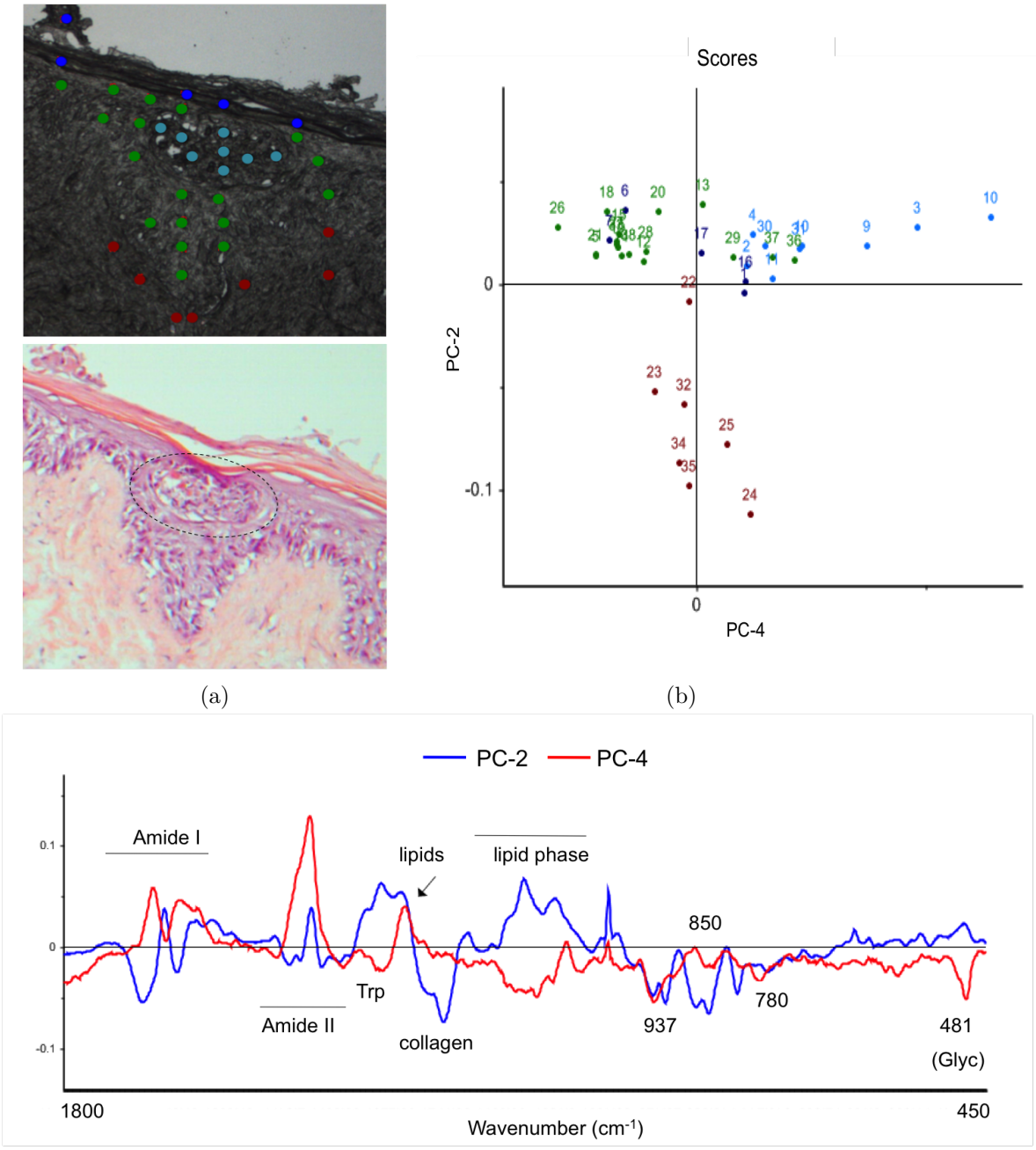

(a) (b)

(c)

Figure 6.2: PCA results of A375SM category (1) areas I: (a) White light and H&E images of PCA area. Dashed circle in H&E image represents A375SM cell cluster. Data points in white light image are colour-coded based on H&E features. (b) Scores plot for the model setup over the region 1800-450 cm^{-1}. The plot has a PC separating dermis spectra (PC2) and a PC that separates inner tumour clusters from surrounding tissue (PC4). (c) Loading plots of PCs from (b). PC loadings that separate tumour from surrounding tissue highlight areas associated with various AAs, lipid phases and Amides.

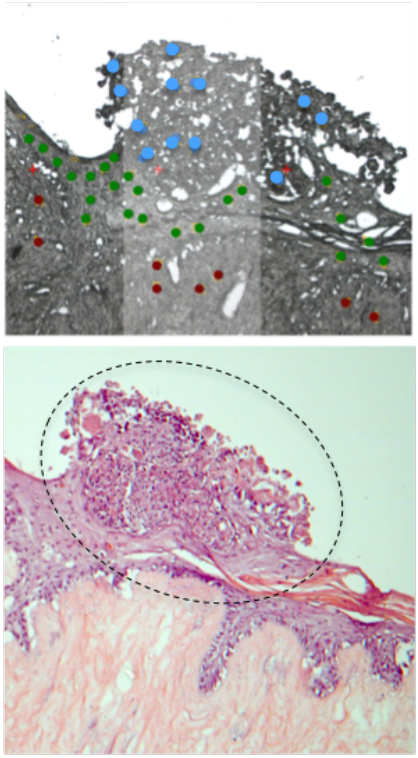

(a)

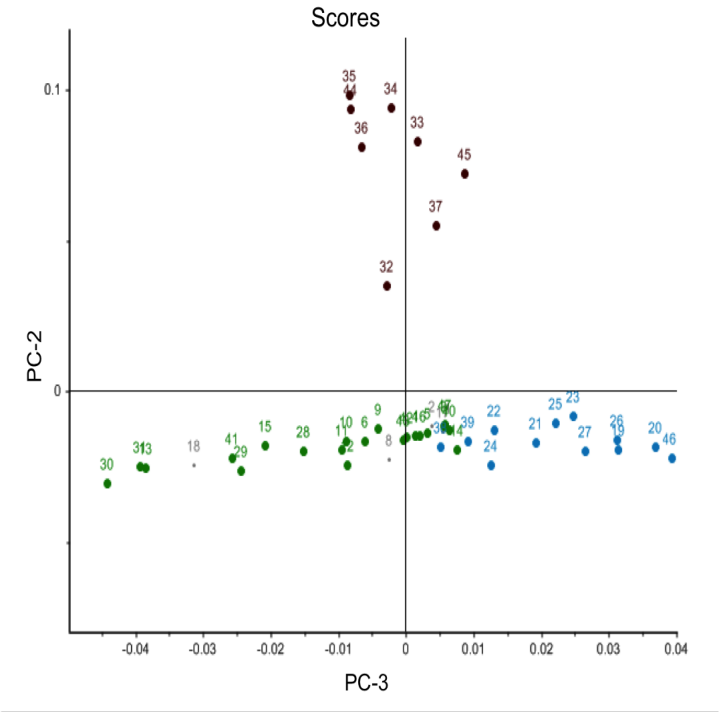

(b)

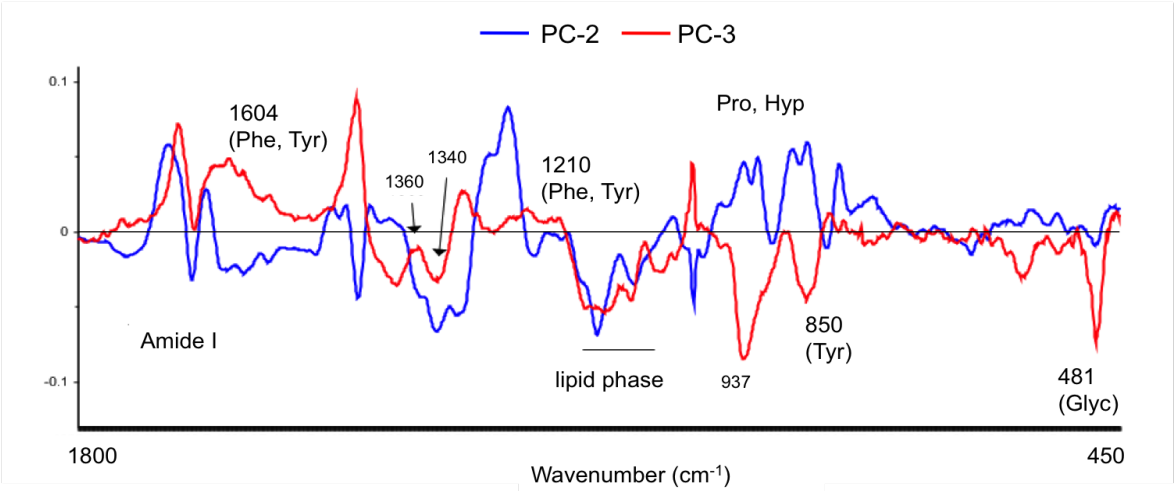

(c)

Figure 6.3: PCA results of A375SM category (1) areas II: (a) White light and H&E images of PCA area. Dashed circle in H&E image represents A375SM cell cluster. Data points in white light image are colour-coded based on H&E features. (b) Scores plot for models setup over the region 1800-450 cm^{-1}. The plot has a PC separating dermis spectra (PC2) and a PC that separates inner tumour clusters from surrounding tissue (PC3). (c) Loading plots of PCs from (b). PC loadings that separate dermal layers are nearly identical in all category (1) area PCAs. PC loadings that separate tumour from surrounding tissue pick out most of the same features as seen in Figure 6.2.

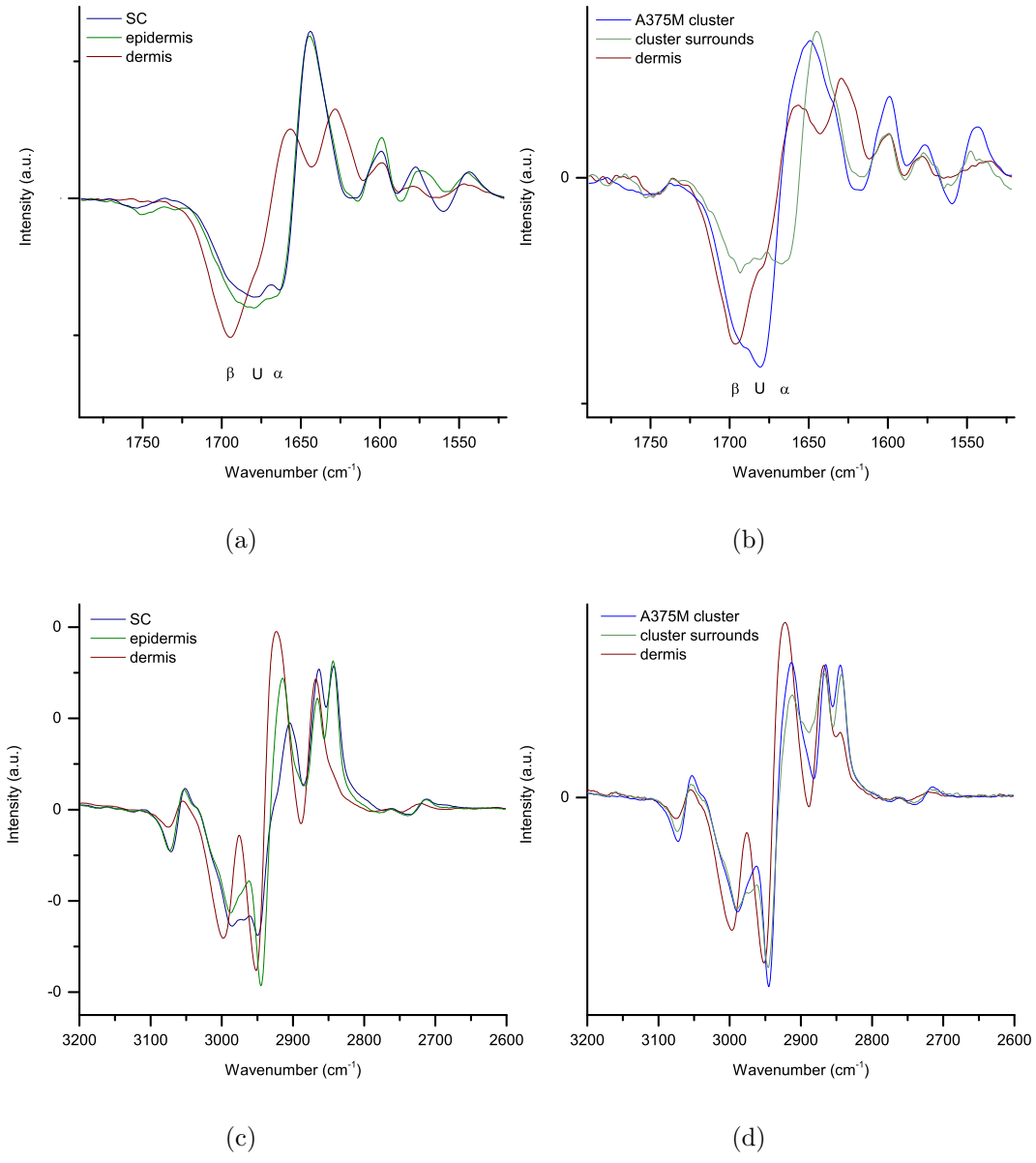

Figure 6.4: Features of A375SM (right) category 1 areas compared to normal HSEs (left): (a,b) 1st derivative spectra of Amide I band. Percent contribution of α-helix, Unordered and β-sheet proteins in melanoma-dense clusters and surrounding epithelial tissue are different. (c,d) 1st derivative spectra of high wavenumber area (3200-2600 cm^{-1}). I_{2840}/I_{2880} ratio suggest a more fluid (gauche) lipid compositioin in A375SM models. Spectra from each colour-code has been averaged over several sample areas.

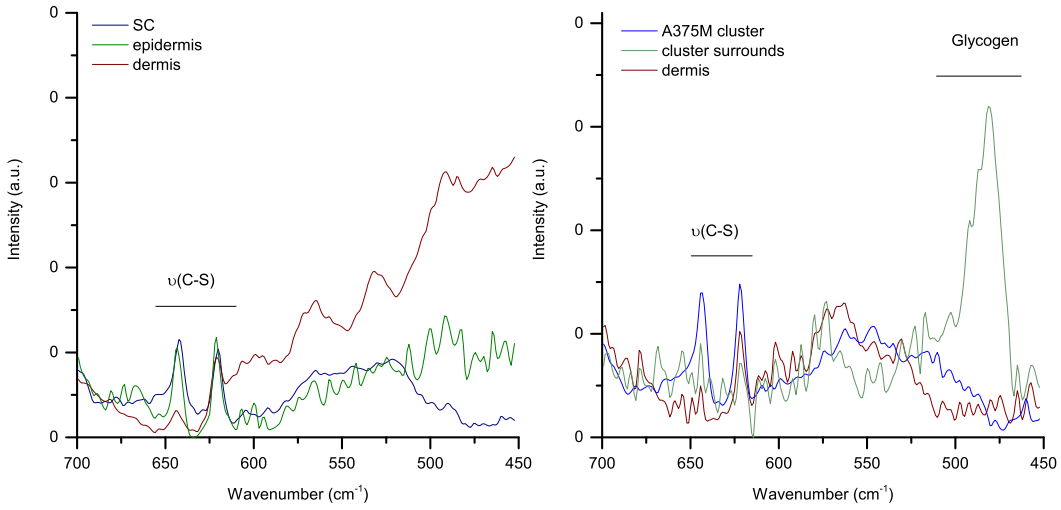

(a) (b)

Figure 6.5: Features of A375SM category 1 areas (b) compared to normal HSEs (a): Raman pectra of spectral range 700-450 cm^{-1} showing the increase in the glycogen peak at 481 cm^{-1} relative to the υ(C-S) peaks at 640 and 620 cm^{-1}. Spectra from each colour-code has been averaged over several sample areas.

6.2.2 C8161 type melanoma composites

Morphological features of C8161 models were found to be more heterogeneous compared to A375SM models. Sample features were divided into four categories to describe different behaviours, Figure 6.6. These were: (1) areas with high densities of C8161 cells spread across the surface, (2) areas where large numbers of C8161 cells had invaded the dermis in close proximity to the basement membrane, (3) areas with clusters of assumed C8161 cells encapsulated within the epidermis and (4) areas with no apparent C8161 cells. Areas of category (1) were nearly always accompanied by large swirls where the epidermis was apparently degrading. This cell line is known to disorganise the epidermis and were seen to aggressively invade the dermis when cultured with keratinocytes and fibroblasts [Eves et al. 2003].

6.2.2.1 Spectral features of Category 1 and 3 areas

PCA loadings (Appendix) indicated AA bands for Tyr and Phe were significantly different in areas dense in C8161 cells versus surrounding tissue. In particular, a peak at 1583 cm^{-1} that represents δ(C=C) vibrations of Phe [Talari et al. 2015] shows apparent

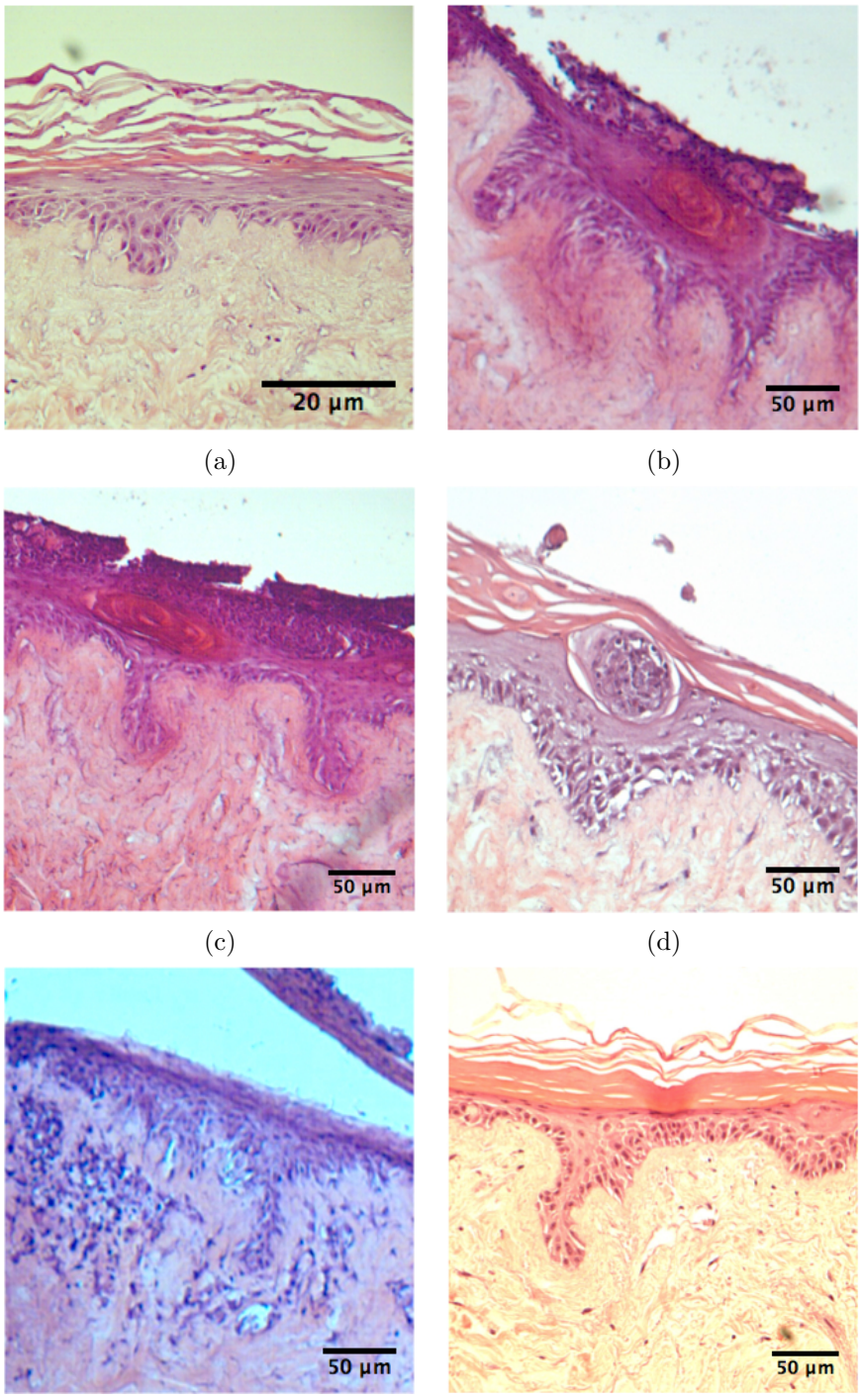

Figure 6.6: H&E of C8161 melanoma models showing four morphological categories: (a) normal HSE, (b-d) Areas with C8161-dense surface layers and areas with clusters of C8161 cells within the epidermis. (e) Areas with C8161 cells invading into dermis. (f) Normal looking areas of C8161 models.

sensitivity to separating the surface C8161 layer from to the rest of the sample areas. Another notable feature that repeated in most of the PCAs was at approximately 781 cm^{-1}. This peak consistently separated the surface layer (where it was the highest) and the epidermal swirls (where it was the lowest) from other surrounding tissues. The peak represents Uracil based ring breathing modes of DNA and RNA [Talari et al. 2015]. It likely points to high cell densities in the surface layer. A number of other spectral changes identified in these areas were similar to those found in A375SM models, Figure 6.8. In Amide I, C8161 clusters again describe a greater number of Unordered proteins. Overall, Unordered and β-sheet proteins appear to be higher compared to normal HSEs even in epithelial tissues further away from C8161 dense areas. Lipid phase of these melanoma-dense areas also appear more fluid and epithelial tissue surrounding clusters show increased glycogen storage. In C8161 models these effects are seen in much larger areas (spread across whole samples) compared to A375SM models (closer to seeding points) but don't appear as distinct from normal skin spectra as A375SM models. This is evidenced especially in the 985-700 cm^{-1} region, Figure 6.9.

The spectral features mentioned in this section are ones that held true for most of the areas in the samples studied. However, it needs to be emphasized that spatial consistency of the epithelial layer between samples was much lower than in A375SM models. A final interesting feature of the surface-spread C8161 layer is a change in the sulphide peaks at 640 and 620 cm^{-1}. There is a major difference in the ratio of these peaks for approximately 75% of the surface-spread spectra, 620 >640 cm^{-1} (Figure 6.8d). This is not seen in any of the other TE skin models made.

6.2.3 Comparison between features of A375SM and C8161 melanoma models

The two melanoma cell lines used in this work to some extent represent two different stages of melanoma that may be found *in situ*. In tissue engineered skin models A375SM cells form clusters and grow larger over time within the epithelial layer with occasional invasion into the dermis: assumed stage II. In constrast C8161 cells are highly invasive and appear to quickly spread across large surface areas and invade into the dermis: assumed stage III or IV (see Appendix for melanoma staging &grading system). Samples were difficult to identify when intact: models constructed with both of these cell lines formed amelanotic samples and C8161 cells have previously been shown to not stain for the two common melanoma antibodies (HMB-45, S100) [Eves 2001]. It

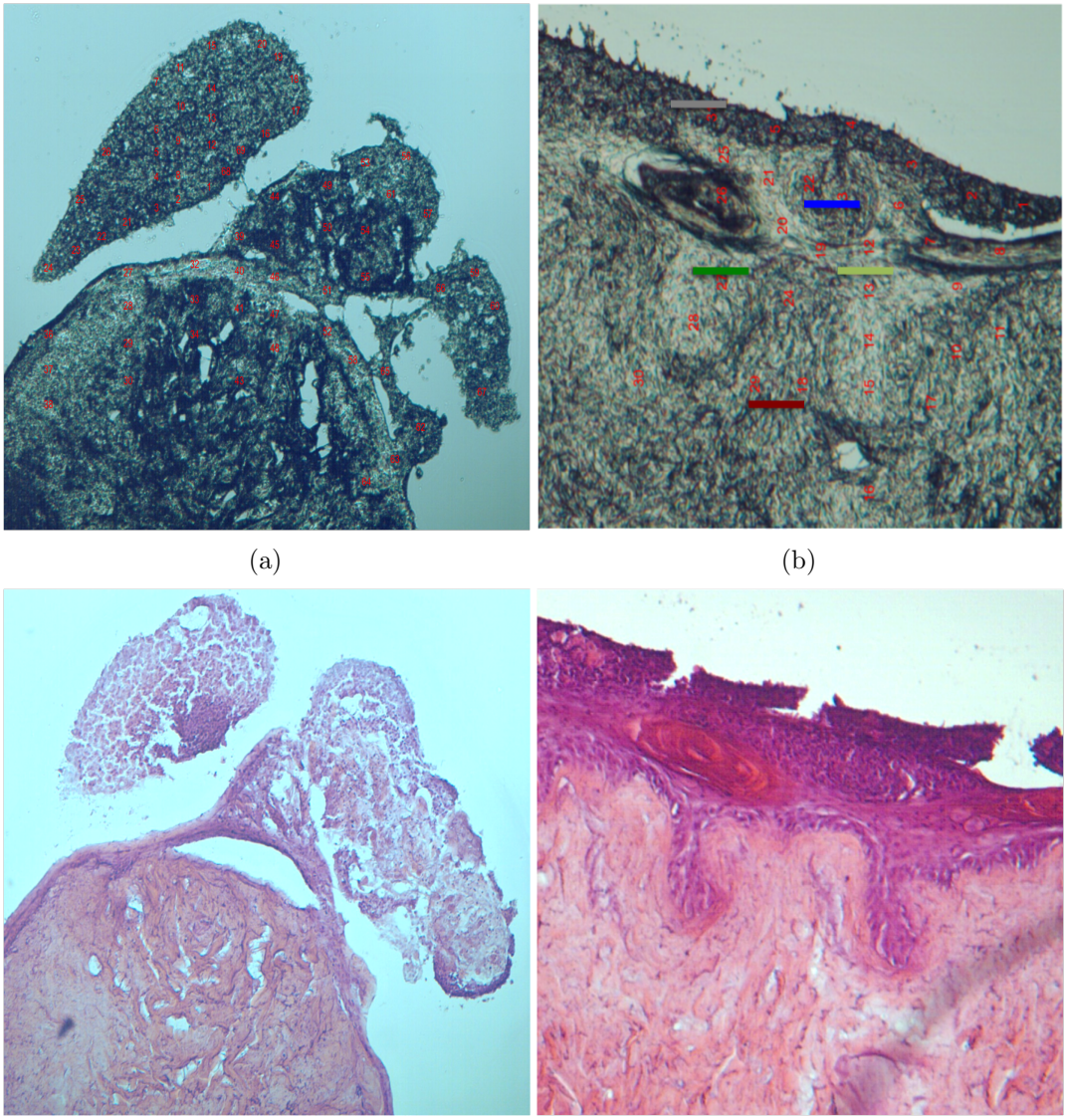

(a) (b)

(c) (d)

Figure 6.7: H&E and white light images of two C8161 model areas from categories 1 and 3 used as part of PCAs. Collection points are seen as red dots. Each point was compared to adjacent H&E stained sections to assign area type. See Appendix for PCA results.

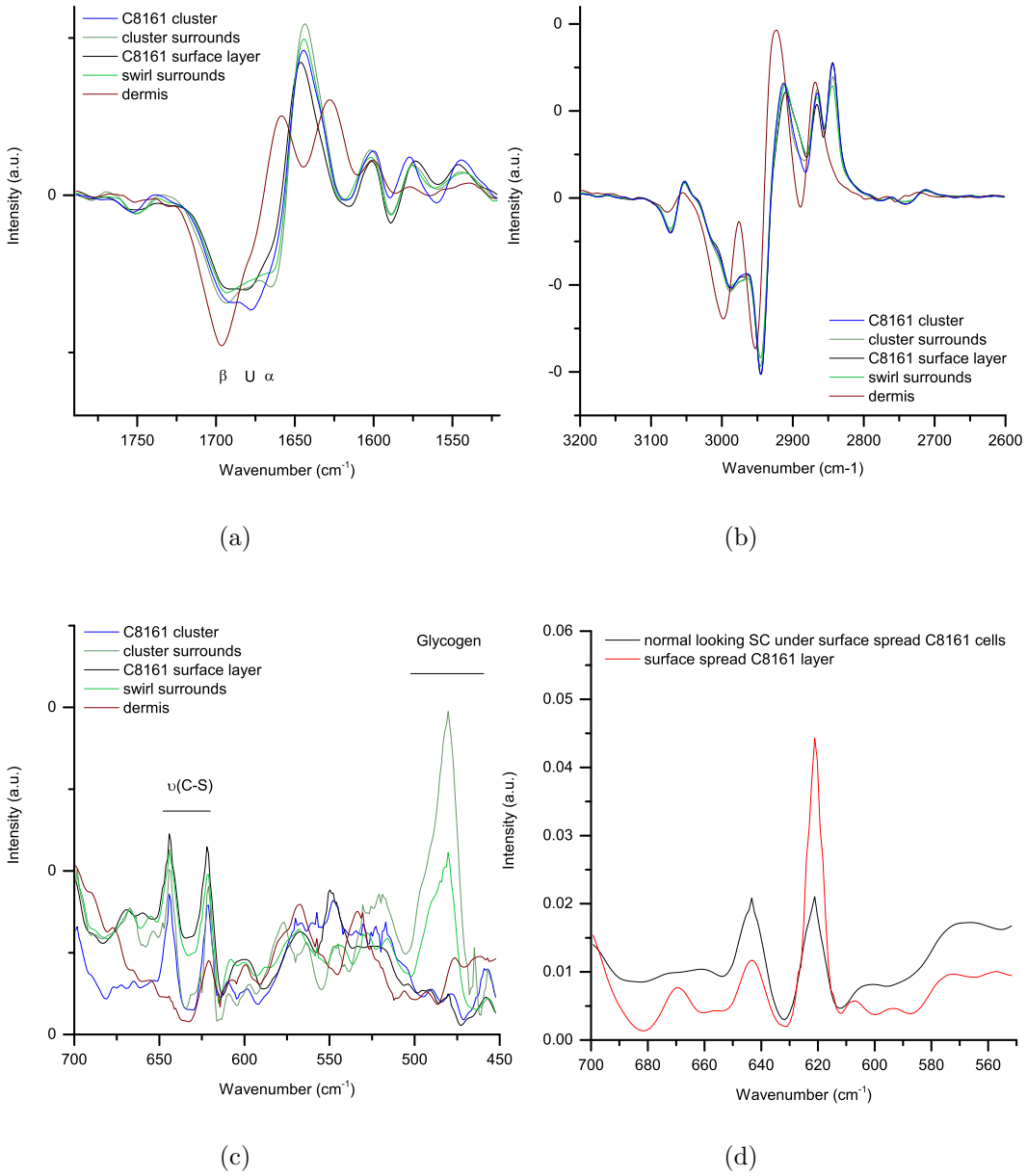

Figure 6.8: Features of C8161 category 1 and 3 areas: (a) 1st derivative spectra of Amide I. There is increased percentage of Unordered and β-sheet proteins compared to normal HSEs. Even the surrounding tissue is much higher in Unordered proteins. (b) 1st derivative spectra of the high wavenumber region (3200-2600 cm^{-1}). As with A375SM models, lipid packing appears to be more fluid in C8161 models compared to normal HSEs. (c) Raman spectra of spectral range 700-450 cm^{-1} showing an increase in Glycogen peak at 481 cm^{-1} relative to υ(C-S) peaks. (d) Difference in the ratio of υ(C-S) vibrations at 640 and 620 cm^{-1} in some surface spread C8161 dense layers.

is of interest to find spectral differences between melanoma models and normal HSEs but also between the two melanoma types because of this vastly different behaviour.

Significant band ratios between A375SM, C8161 and Normal skin models: Several spectral differences between the models are highlighted in Table 6.4. A number of these are protein-specific: (1) There appears to be minor differences in the 2930 cm^{-1} protein band in cancerous tissues. The position of this band was previously attributed to a compact and highly folded protein nature in normal skin SC and epidermis (Chapter 5). The shifts here are small but consistent in all cancer samples and might suggest some disorganisation in protein architecture of whole melanoma composites. (2) Within tumour clusters of both cell types, and surface-spread tumour layers, Amide I position strongly suggests higher percentage of unordered and β-sheet conformation proteins instead of α-helix: Unordered $>\beta$-sheet in clusters but β-sheet >Unordered in surface-spread layers. As it is observed in models with both cell lines, it is possible that the differences in these ratios arise from: (i) requirements of a clustering mechanism versus for proliferation without any boundaries or (ii) an indication of the proliferative state of the melanoma cells. (3) The ratio $I_{1340}/_{1360}$ represents the ratio of surface exposed versus buried Trp moieties within epidermal proteins. In cancer models, there is an increase in the number of buried Trp chains. This likely indicates a more hydrophobic environment but also a change in Trp-mediated processes compared to normal skin. (4) Apart from structural differences, protein-to-lipid ratios within the models also show some variation. The ratio I_{2930}/I_{2840} was previously used to trace lipid-dominant epidermal layer down to protein-dominant dermal layer (Chapter 5). The relative concentration of proteins and lipids appear to be similar between melanoma models and the superficial layers of normal skin. The biggest difference is seen in the surface-spread tumour layer of A375SM models where protein content is markedly decreased and furthermore, whilst the overall lipid content is perhaps the same, the packing order of lipids is not. Compared to normal skin, cancer models show a higher percentage of gauche lipids in areas of every tumour-invaded category.

Both cancer models also showed increased glycogen storage in epithelial tissues surrounding tumour clusters compared to normal skin. The increase was much more prominent in A375SM clusters. Tyr configuration also appears to be different in melanoma-dense clusters, Figure 6.9, Table 6.2. A big difference between A375SM and C8161 models is also at 780 cm^{-1}. This band represents ring breathing vibrations of DNA and RNA bases. It is considerably lower in A375SM models compared to both

C861 and normal skin models.

Classification based on epithelial layer spectra: A LDA model was setup with data from entire epithelial layers of A375SM, C8161 and normal skin models in order to determine if the tissue state could be predicted from Raman spectra despite large biochemical variations within cancer samples, Table 6.3. LDA was setup with three class categories: normal (50), A375SM (80) and C8161 (80). Five random spectra from each class category were left out at each run until a total of 20 spectra (so called non labelled samples) were tested. Specificity was found to be very high and sensitivity to the cancer state was also very high (no melanoma samples have been assigned to Normal class). However, sensitivity to detecting models of the specific melanoma cell lines was much lower.

Table 6.2: Comparison between melanoma and normal HSEs in the spectral range 985-700 cm^{-1}

Tissue	780 cm^{-1}	I_{750}/I_{760}	I_{850}/I_{830}
Normal	High in epidermis, low in SC	High in SC, decreases in epidermis	I_{850} higher in SC and epidermis
A375SM	Very low in all A375SM areas	I_{750} much lower, I_{760} higher compared to normal areas	I_{830} much higher in clusters, similar to normal in surrounds
C8161	High in all areas except clusters	I_{760} higher, I_{750} similar to SC in all areas	I_{830} higher in clusters, similar to normal in surrounds and surface

Table 6.3: Classification results for normal skin and melanoma models. The model was setup over the range 3400-500 cm^{-1} and from spectra collected from all epidermal areas of the melanoma models (clusters, surface spread and epithelial tissue far away from any tumour cluster). Normal state can be identified accurately but the parameters used in this LDA model do not accurately predict models of the different melanoma cell lines.

Predicted **Actual**	Normal	A375SM	C8161
Normal	19	0	0
A375SM	0	7	2
C8161	1	13	18

6.3 Discussion

Raman analysis on tissue engineered melanoma composites built with two melanoma cell lines are presented in this chapter. In studying normal skin layers, spectral features relating to each layer were first assigned via visual observations of location-labelled spectra. Subsequent analysis with MVA methods verified that these features held true for all samples. This approach was taken because normal skin layer composition was assumed already to be quite homogeneous within samples (epidermis, dermis) and the layers were easily identified with H&E staining. Melanoma samples by comparison showed a lot of morphological variation within and between samples. The type of variations were mostly consistent. Sample areas were first divided up into categories representing the commonest morphological features. The approach was then to perform PCA over whole areas and focus on loading features that held true in all areas of a respective category. This worked better in A375SM models. Trends in several spectral bands were observed repeatedly in the loadings separating melanoma-dense areas from surrounding tissues. Here we discuss ones related to glycogen accumulation, lipid disordering and changes to protein configurations. These are unlikely to be characteristic of only melanoma. Many of the spectral changes identified here are also seen in other disease states (e.g. immune disorders such as psoriasis) and in tissues put under stress (e.g. tape stripping, hypoxia). Conjectures about their role in melanoma here are perhaps better considered as stepping stones toward tailoring experiments more appropriate to further define the causes and consequences of the spectral differences.

Glycogen accumulation in tissue surrounding tumour clusters in epidermis: In this study we reported localised glycogen accumulation in the primary surrounds of tumour clusters located within the epidermis. The effect is found to be specific to areas only in the primary vicinity of clusters, not the entire epithelial layer. It is unlikely that the effect arose from culture conditions: Glycogen storage is a stress response. Exposure to UV radiation [Lobitz et al. 1962] or conditions such as psoriasis [Harmon and Phizackerley 1984] cause increased glycogen storage across entire skin areas affected by these conditions. Localisation in these cancer models suggests the stress response more likely arose from changes to microenvironment. It is unclear whether or not the activation is due to a foreign body (melanoma-spheroid) or if the keratinocytes are responding to broader bio-signal specific consequences of the melanoma clusters. Melanoma cells migrate to the SC and spread across surface even though they are added on the same day as keratinocytes. In A375SM models, it was previously reported

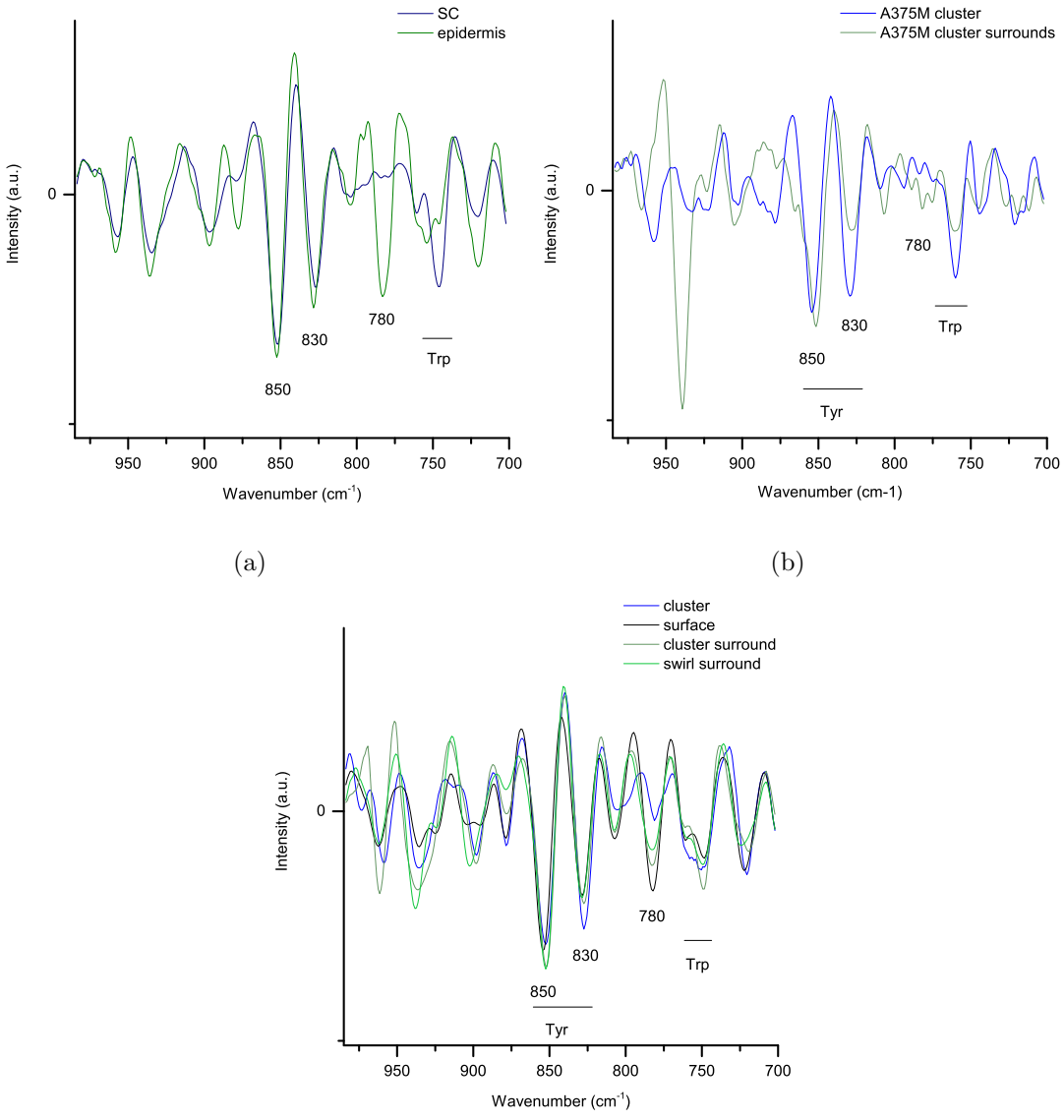

Figure 6.9: Comparison between melanoma and normal HSEs in the spectral range 985-700 cm^{-1}. Highlighting differences in Tyr, Trp and a peak at 780 cm^{-1} in in the 2nd derivative spectra for (a) Normal, (b) A375SM, and (c) C8161 models. Overall, tumour surrounds in C8161 models resemble normal HSE more closely than A375SM models.

Table 6.4: Significant band positions and ratios relating to the form of proteins and lipids in melanoma and normal skin models

Tissue (+area)	2930 cm^{-1} position	I_{1340}/I_{1360}	I_{2930}/I_{2840}	I_{2840}/I_{2880}
Normal skin				
SC	2930.60 (2928.92-2931.53)	1.73 (1.11-2.16)	2.94 (2.52-3.24)	0.58 (0.55-0.64)
epidermis	2930.47 (2925.05-2931.42)	3.66 (1.66-5.49)	2.73 (2.38-3.12)	0.58 (0.56-0.58)
dermis	2939.11 (2927.76-2940.67)	-	6.01 (5.61-6.74)	-
A375SM models				
epidermis (surrounding clusters)	2932.31 (2930.79-2933.44)	1.82 (1.63-1.92)	3.24 (2.41-5.91)	0.53 (0.46-0.59)
A375SM clusters	2933.06 (2931.10-2934.76)	1.99 (1.52-2.08)	2.77 (1.67-3.89)	0.61 (0.49-0.77)
surface A375SM layer	2931.39 (2930.75-2933.40)	1.88 (1.57-2.18)	1.85 (1.53-2.35)	0.79* (0.67-0.87)
dermis	2939.28 (2938.72-2940.28)	-	7.66 (4.90-9.58)	-
C8161 models				
epidermis I (surrounding clusters)	2932.42 (2931.70-2933.20)	1.95(1.51-2.37)	3.04 (2.56-3.35)	0.57 (0.52-0.64)
epidermis II (surrounding swirls)	2932.11 (2931.10-2931.40)	1.88 (1.52-2.24)	3.25 (3.07-3.48)	0.55 (0.51-0.57)
C8161 clusters	2932.16 (2932.12-2932.40)	1.66 (1.53-1.80)	2.48 (2.15-2.80)	0.65 (0.60-0.72)
surface C8161 layer	2932.45 (2931.90-2932.90)	2.38* (1.74-3.36)	2.74 (2.19-3.42)	0.64 (0.54-0.71)
dermis	2938.99 (2936.60-2940.40)	-	6.76 (4.26-8.59)	-

that melanoma clusters -chew- through the epidermal layer [Eves et al. 2003]. The chewing action may activate mechanisms associated with wound healing which is also known to increase glycogen storage in keratinocytes. In wound healing, a gradient of increasing accummulation is observed from the marginal epidermis (x3 normal) to the migrating epithelium (x7-13 normal) [Hoopes and Im 1974]. Stress response is also biphasic. Highest glycogen content is seen approximately 24-48 hours after the stress is induced in the microenvironment and returns to normal 24-48 hours after it is removed [Straseski et al. 2009]. While unlikely to be melanoma-specific, the effect is interesting. And though it was not quantified here, the peak at 481 cm^{-1} has been shown to be a good indicator of glyogen content in tissues on par with Periodic acid Schiff (PAS) staining. Careful calibration of the peak has been shown to quantify glycogen content even in cell cultures [Konorov et al. 2011].

Protein configuration different in tumourous areas: The high wavenumber protein band and Amide I suggest the ratio of α-helix, Unordered and β-sheet proteins are different between cancer models and normal skin. The contrast between the Amide I bands is quite plain but reasons for the change are unclear. Based on this band alone, the conformations of proteins were strictly maintained in normal HSEs (very minor changes to ratio throughout epithelial layers in all samples) whereas it appears that melanoma cells comprehensively cause alterations in protein structures in the system. The ratio is even different between melanoma clusters and surface-spread melanoma layers. This suggests there isn't a single melanoma-specific state of protein expression but that it is dynamic. Expression likely changes depending on the microenvironment and/or the stage. Peaks related to certain AAs also point to structural modifications in proteins.

In these cancer models, three AAs in particular were of interest: Phenylalanine (essential), Tryptophan (essential) and Tyrosine (conditionally non-essential). These AAs belong to a family of proteinogenic AAs. Proteins they build play a critical role in regulating homeostasis via their catabolic products and through their function in key sites for enzyme activation. Quantification of these AAs are difficult due to mode mixing. We report instead that the configuration of Trp and Tyr are different in the cancer models. This likely suggests some changes to the activity of Trp and Tyr mediated products. The exact changes cannot be elucidated based solely on data from these samples but examples of how even minor changes in Trp and Tyr can affect tissues are highlighted below.

Trytophan: I_{1340}/I_{1360} ratios here indicate a higher percentage of proteins with buried Trp chains in cancer samples compared to normal HSEs. Trp is mostly used up through the Kynurenine pathway and its catabolism products are immunoregulatory. Changes to the rate of its breakdown is implicated in several diseases including HIV and neurodegenerative disorders [Schröcksnadel et al. 2006, Ruddick et al. 2006, Campesan et al. 2011] because the catabolism products are thought to facilitate immune tolerance [Moffett and Namboodiri 2003]. The rate limiting step of the breakdown is via the enzymes tryptophan-dioxygenase (TDO) or indolamine-dioxygenase (IDO). TDO and IDO activity is dependent on the hydrophobic pocket formed when the Trp chain is buried within the protein [Thackray, Mowat, and Chapman 2008]. Reducing the hydrophobic nature (thus changing the shape of the activation pocket) has been shown to affect substrate binding [Chauhan et al. 2012]. In all areas of the cancer samples, I_{1340}/I_{1360} ratios suggests hydrophobic pockets exist in a greater number of proteins compared to normal skin. Assuming this means more active TDOs, it could mean increased Trp catabolism in cancer samples. Another theory is that the buried state of Trp chains may be markers for proliferative state. This theory is mostly realised in fluorescence spectroscopy studies. Trp fluorescence increases as Trp moieties are folded into proteins versus when exposed. Using this method, the amount of buried chains are found to increase in skin with UV exposure and after tape stripping of the SC [Brancaleon, Lin, and Kollias 1999] and in the non-involved skin parts of psoriasis patients [Gillies et al. 2000]. These groups report increase in fluorescence correlates with proliferative activity. Based on this theory, proliferation in all areas of A375SM models is greater than in normal skin epidermis. In C8161 models, whilst the epidermis and C8161 cell clusters show very high proliferation, the rate appears to be lower in surface-spread C8161 cells but these initial findings have limited use. 1360 and 1340 cm^{-1} peaks represent the aromatic ring breathing vibrations of Trp where changes to ring orientation within the protein is reflected in the raman spectrum (1360 vs 1340). However, the first step of Trp degradation directly involves the indole ring, Figure 6.10. Vibrations associated with this ring at 1550, 1490 and 1430 cm^{-1} [Miura, Takeuchi, and Harada 1989] are likely to be more informative because this pathway regulates systemic Trp levels. The problem is that, here, these peaks are either very weak (1550 cm^{-1}) or are overpowered by other stronger bands (Amide II in 1490, 1430 cm^{-1}). Trp-specific trends in tissues may be better studied with UV Resonance Raman as Trp peaks are enhanced by several orders of magnitude using this method [Caswell and Spiro 1986, Sweeney and Asher 1990].

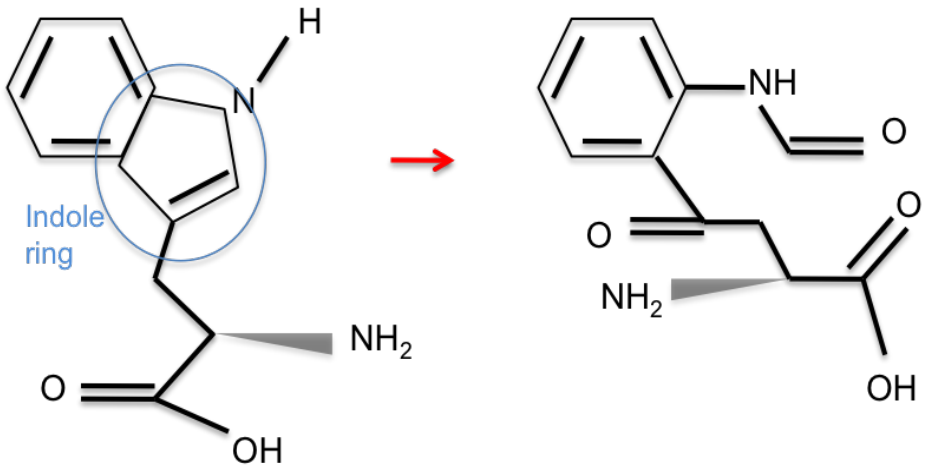

Figure 6.10: First step of the Kynurenine pathway: Trp (left) from IDO is degraded via the indole ring.

Tyrosine: Although I_{850}/I_{830} ratios were not quantified, visual observations and PCA suggest a greater number of buried Tyr chains in the clusters and surface-spread melanoma cells. Tyrosine presents in a large number of proteins involved with signal transduction, such as tyrosine kinases (PTK). Protein kinases are a group of catalytic enzymes that are activated via the phosphorylation reaction with AA residues Serine, Threonine and Tyrosine. They regulate a number of vital metabolic and secretary processes. Kinases share a common fold but differ in terms of the charge and hydrophobicity of AA residues. The shape and form of the hydrophobic pockets arising from these differences influence substrate specificity [Ubersax and Ferrell Jr 2007]. In the case of PTK, a single Tyr chain is phosphorylated for activation. After this, interaction of the Tyr residue with a neighbouring Arginine residue activates PTK by opening up and stabilising a hydrophobic, substrate-binding site [Nagar 2007]. PTK activation in normal cells are very strictly regulated and balanced (on a need basis). Any disruptions to the balance leads to cell transformations and causes unregulated cell growth [Hunter 1998]. Drugs such as Imatinib inhibit this enzyme by binding to the active site, preventing other substrates from binding it. This is an effective treatment in some cancers such as Chronic Myelogenous Leukemia (CML) where PTKs are permantly turned -on- [Nagar 2007]. Changes to the I_{850}/I_{830} ratio compared to normal skin is important because it implies some changes to the location/orientation of Tyr chains within proteins. Markers of Tyr hydrophobicity in particular are interesting because the level of hydrophobicity has been shown to play a critical role in PTK function: Replacing

a buried Tyr chain with polar residues that reduce hydrophobicity also decreases substrate binding [Tadaki and Niyogi 1993]. Interestingly, changes to Trp configuration is seen in the entire cancer samples whereas changes to Tyr configurations are seen nearly exclusively only in melanoma-dense clusters and layers.

Classification: LDA was setup over the full spectral range (3200-400 cm^{-1}) and with spectra from all areas of epidermal layers (clusters, surface spread, tumour surrounds). Model accuracy may improve considerably if setup in narrower spectral ranges more sensitive to differences between the two melanoma cell lines. Such as the amide bands, and 985-700 cm^{-1} region. Here, classification was performed on data collected from *in vitro* sections only. However, *in vivo* data collections were shown to be viable in Chapter 5. This might lend itself to clinical applications. Collecting data from the surface of melanoma models while in culture may be comparable to collecting data from patients in the clinic. Clinical features of melanoma vary greatly depending on subtype and stage. Many benign naevi also exhibit the same symptoms. Changes in the size, shape and colour of a lesion are the main discriminators. The first step of diagnosis is a physical examination. If the doctor considers the lesion suspicious, a biopsy is taken for histological analysis:

- In the first step, the lesion is assessed based on either or both of the ABCDE rule and the Seven-point checklist. Depending on experience, clinicians can be very accurate in detecting melanoma. Sensitivity and specificity is reported to be 90+%, 70+% for dermatologists with 10+ years experience but much lower for 3-5 years of experience at 62%, 46% and even lower for non-dermatologists [Cassileth et al. 1986, Chen et al. 2001]. This experience-dependence is the main problem in this screening step.

- Histopathological analysis of melanoma includes examination of a large number of morphological features. The sensitivity and specificity varies depending on the feature examined. For example, it is 95.8%, 64.4% for Asymmetry, 63.9%, 75.3% for Irregular and confluent nests [Urso et al. 2008]. The method has very high overall accuracy because a combination of features are reported (10+). This diagnosis step is costly and invasive but is allows the staging and grading of melanoma, critical in deciding on treatment course and prognosis.

It is tempting to consider the advantages of RMS for the second step. RMS does not require any stains, has high sensitivity to biochemical composition and has high

resolution. However, it is unlikely that there will be a single raman marker that completely separates melanoma tissues from normal skins due to the dynamic nature of the disease (e.g. receptor expression is different in primary tumours and where it is spread). Indeed, in this work, we have even seen differences in the melanoma-dense areas of clusters and surface-spread layers. What LDA of raman data reports here is a deviation from the normal state of skin tissue. This can lend itself to screening melanoma if classification accuracies found with the *in vitro* sections can be extended to spectra collected *in vivo*. Screening tools need to be objective, simple, non-invasive, reproducible and accurate. RMS may fill all these criteria only if specificity remains high when a larger number of skin conditions are added to classification models. With a critical emphasis on benign conditions that can resemble melanoma.

6.4 Conclusions

In this chapter preliminary data regarding the regional effects of melanoma on skin tissues and the results of predictive tissue classification in identifying melanoma tissues is presented. The same properties that make RMS an effective tool in HSE quality analysis also recommend it for cancer research: its ability to -see- many different biochemical aspects of the tissue. Because whilst genetics can clearly help in searching for the underlying cause and in treatment (BRAF inhibitor drugs in melanomas with BRAF mutations), larger-scale properties of melanoma tissues may be more efficient in understanding its routes of progression. We show here for example, that in TE melanoma models, melanoma cells induce changes in the surrounding tissue that are also common to other diseases. This opens up the possibility of looking into concepts on the management of these other diseases; controlling progression via control of the microenvironment. In a field governed with reductionism, tools that can quantify the whole system with larger-scale properties like this should be explored and encouraged.

Chapter 7

Conclusions and Future work

This study has demonstrated the applicability of RS data to evaluate the quality of tissue engineered skin models while still in culture. Where quality has been assessed in relation to epidermal thickness and barrier properties. Estimation of these properties have produced good results with no adverse effect to the culture conditions or tissue. For depth profiling work, there is much interest in current literature in tracking topically applied products on skin tissues. The purpose of such work is tracing penetration of the much stronger signals of drug formulations against the much weaker and often overlooked tissue signals. Here, we tried to obtain depth profiles with skin spectra that contains sufficient detail and resolution for qualitative information to be extracted. The next stage of this work would likely be to compare and optimise the methods for assessment of these properties with fiber optic probes for remote sampling. This would favour both pharmaceutical testing of tissues and be of clinical interest as it may be suitable for monitoring tissue transplants post implantation.

Where the option of remote access makes RS attractive for normal skin monitoring, its ability to extract information from tissue sections independent from any stains and dyes make it attractive for melanoma research. A big disadvantage is the lack of reference data. Raman spectra are information rich but interpretation requires references. For example, we are able to infer the position of Trp in proteins from the aromatic ring peaks because these peaks have already been studied under conditions that expose and bury chains in a number of protein derivatives. The same is not true for the indole ring of Trp which hinders our interpretation of Trp breakdown.

Most of the RS work on melanoma in literature is done on biopsies. A large per-

centage of these compare averaged spectra and then perform LDA on a set of biopsies usually including some other types of skin cancers and a benign condition. Their context is nearly always to show the accuracy RS data for screening. The applications make use of predictive chemometric methods to determine the state of interest but offer little attention to the nature/reason of changes. Biopsies are hard to come by and scientists are typically reliant on whatever biopsies are made available to them by the hospitals. This is in big contrast to having samples from carefully controlled experiments to answer very specific questions. Proof-of-concept studies for screening serve as good options in light of limitations related to sample access. Tissue engineered models can be a big advantage in this respect as they allow scientists to design their own experiments.

A number of investigations that would validate some results of this thesis could not be carried out due to lack of time. These include the following:

- Immunohistochemical staining of melanoma samples. S-100 antibodies should preferentially stain A375SM dense areas validating intra-epidermal clusters and surface-spread tumour layers.
- PAS staining of melanoma tissues would validate glycogen accumulation in tissue surrounding tumour-dense areas. Further to this, it might be of interest to quantify glycogen using the 481 cm^{-1} peak. This might then be compared to wound healing models to measure how similar the epithelial response is.
- RS on melanoma models fixed at different time points to study progression. This might reveal spectral features that switch on or off during early and late stages of growth.
- **It is suggested that changes to the microenvironment may direct initial transformation and promote progression and invasion following transformation [Bissell and Radisky 2001, Tlsty and Coussens 2006].** (Chapter 6). It would therefore be of interest to also look at benign or precancerous nevi (especially if the samples are known to have progressed onto cancer) to see if any of the features identified switch on at any particular point.
- We have not claimed any of the findings in Chapter 6 to be melanoma specific. These need to be validated first on patient biopsies. This could include different subtypes but *should* include benign melanocytic nevi to see if any of the features hold true for melanoma but not for benign nevi.

- Addition of a full spectrum of skin pathologies is also likely to improve interpretation. This is important on two fronts: (i) For comparing pathologies such as psoriasis or other inflammatory diseases that are known to show similar spectral differences with melanoma compared to normal skin. This may help in understanding stromal response (rate, triggers, mechanism) in melanoma. (ii) To compare pathologies that are commonly mistaken for melanoma. In literature, predictions of tissue state using only Raman data are shown to be typically >85% accurate in data sets that contain up to five pathologies such as melanoma, BCC, SK. Addition of more is likely to cause sensitivity and specificity to drop but as long as the separation keeps for benign versus malignant states, this can lend itself to screening very well.

- Tracking identified spectral features after drug treatment of melanoma models.

And on a final note, the multidisciplinary nature of these kinds of studies should be considered in future work. This type of project spans areas of spectroscopy, tissue culture, immunohistochemistry, cancer biology and chemometrics. Working teams should reflect this and include a collaboration between clinicians, pathologists and scientists of different fields.

Chapter 8

Appendix

8.1 Melanoma statistics

Geographic region	Cancer type	Incidence per year (2012)	Mortality per year (2012)
World	Commonest cancer: Breast	1671149	521907
	Melanoma (15th most common)	111481	24098
Europe	Commonest cancer: Breast	494076	142979
	Melanoma (8th most common)	55011	10785
UK	Commonest cancer: Breast	52399	11679
	Melanoma(5th most common)	7545	950

Table 8.1: Incidence and mortality from commonest cancer type and melanoma for women (recreated from [Globocan 2012]).

Geographic region	Cancer type	Incidence per year (2012)	Mortality per year (2012)
World	Commonest cancer: Lung	1241601	1098702
	Melanoma (16th most common)	120649	31390
Europe	Commonest cancer: Prostate	419915	101419
	Melanoma (16th most common)	49181	12723
UK	Commonest cancer: Prostate	45406	10595
	Melanoma (4th most common)	6900	1245

Table 8.2: Incidence and mortality from commonest cancer type and melanoma for men (recreated from [Globocan 2012]).

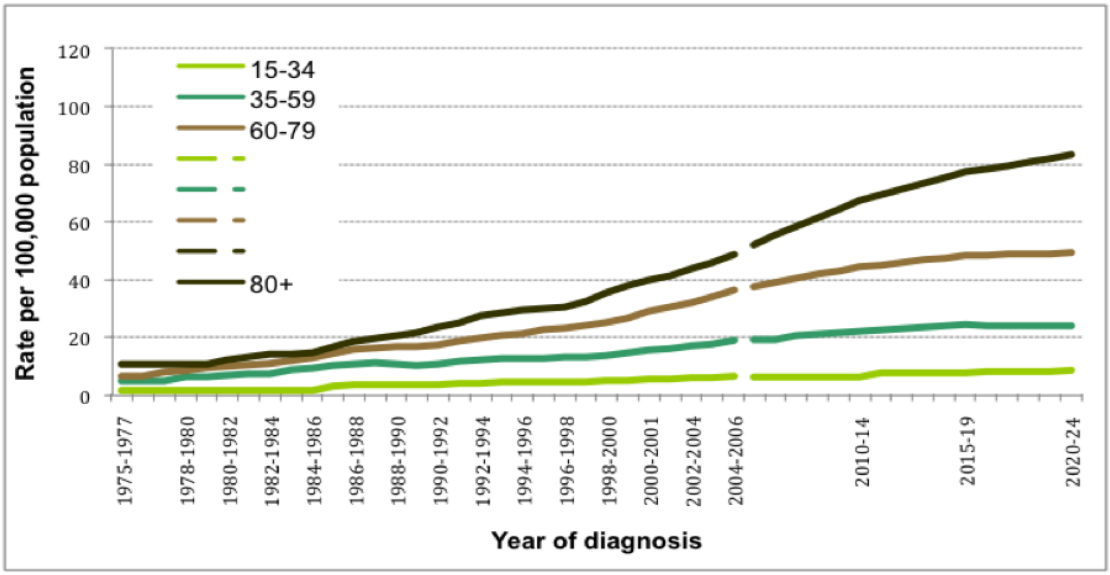

Figure 8.1: Age specific incidence rates of melanoma in the UK [CancerResearch 2011]. The greatest increase is seen in the age group 60-79 with a gender averaged increase of 546%.

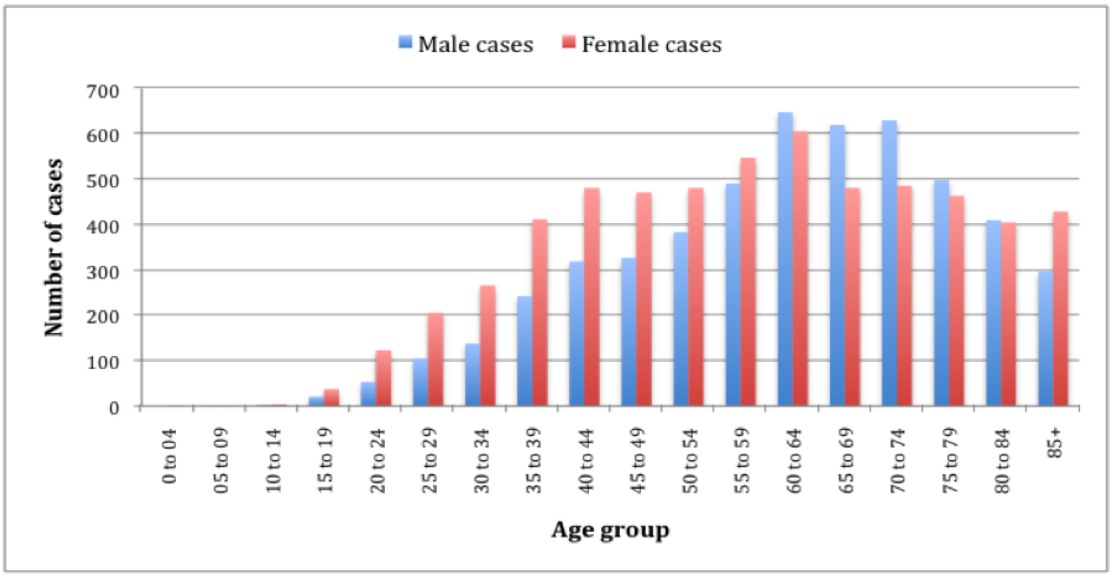

Figure 8.2: Age and gender specific incidence rates of melanoma in the UK (recreated from [CancerResearch 2011]). While the total number of diagnosed melanoma cases are similar for males and females, there is a high percentage of women under 50, and men over 60 that are being diagnosed.

Table 8.3: Melanoma subtypes as listed by WHO [LeBoit et al. 2006].

Ten recognised subtypes of melanoma
Lentigo Maligna Melanoma
Superficial Spreading Melanoma
Nodular Melanoma
Acral Lentiginous Melanoma
Desmoplastic Melanoma
Melanoma arising from blue naevus
Melanoma arising in giant congenital naevi
Childhood Melanoma
Naevoid Melanoma
Persistent Melanoma

Table 8.4: Example markers of melanoma (from [LeBoit et al. 2006, Larson, Konat, and Alani 2009]).

Marker	Type
Melan-A	Differentiation
S-100	Differentiation
TRP-1	Differentiation
Cyclin A and B1	Progression (upregulated during proliferative state)
p16	Progression (downregulated in proliferative state)
E-Cadherin	Progression (downregulated, independent marker for metastasis)
MMP-1, 2 and 9	Progression (upregulated)
MAP2	Differentiation (independent prognostic marker of metastatic recurrence)

8.2 Melanoma classification

TNM and AJCC systems are used to classify melanoma. The systems enable clinicians to estimate a patient's prognosis and decide on treatment. It also allows therapeutic responsiveness to be evaluated post-treatment and for comparisons to be made between different centres. The systems supersede the morphological subtype classification.

TNM system is presented in Table 8.5. Each letter of the system reflects one of three ways cancer spreads. T - extent of invasion into surrounding **T**issue. N - extent of invasion into lymph **N**odes. M - extent of **M**etastasis through blood. A number is then added to each letter to describe extent of invasion. Overall, the system presents an evaluation of: the size of the primary tumour (T), the degree of regional spread (N) and the range of distant metastasis (M).

After TNM classification, the evolutionary level of the disease is described by the AJCC system. This system allocates a stage from 0 to IV depending on invasive capacity of the tumour, with 0 being defined as melanoma in situ, and IV as developed distant metastasis. TNM classifications corresponding to AJCC stages are presented in Table 8.6.

Table 8.5: TNM classification system for melanoma with corresponding AJCC stage (recreated from [Edge and Compton 2010]).

STAGE	TNM CLASSIFICATION
STAGE 0	Tis, N0, M0
STAGE IA	T1a, N0, M0
STAGE IB	T1b or T2a, N0, M0
STAGE IIA	T2b or T3a, N0, M0
STAGE IIB	T3b or T4a, N0, M0
STAGE IIC	T4b, N0, M0
STAGE IIIA	T1a to T4a, N1a or N2a, M0
STAGE IIIB	T1b to T4b, N1a or N2a, M0
	T1a to T4a, N1b or N2b, M0
	T1a to T4a, N2c, M0
STAGE IIIC	T1b to T4b, N1b or N2b, M0
	T1b to T4b, N2c, M0
STAGE IV	Any T, any N, M1(a,b or c)

Table 8.6: AJCC system for melanoma with corresponding levels of invasion (recreated from [Edge and Compton 2010]).

Stage	Primary tumour (T)	Lymph nodes (N)	Metastases (M)
Stage IA	<1mm, no ulceration, mitoses <1 mm^{-2}		
Stage IB	<1mm, with ulceration or mitoses 1 mm^{-2}		
Stage IIA	1.01-2mm, with ulceration 2.01-4mm, no ulceration		
Stage IIB	2.01-4mm, with ulceration >4mm, no ulceration		
Stage IIC	>4mm, with ulceration		
Stage IIIA	Any Breslow thickness, no ulceration	Micrometastases, 1-3 nodes	
Stage IIIB	Any Breslow thickness, with ulceration	Micrometastases, 1-3 nodes	
	Any Breslow thickness, no ulceration	1-3 palpable metastatic nodes	
	Any Breslow thickness, no ulceration	No nodes, but in-transit or satellite metastasis(es)	
Stage IIIC	Any Breslow thickness, with ulceration	Up to three palpable lymph nodes	
	Any Breslow thickness, with or without ulceration	Four or more nodes or matted nodes or in-transit disease + lymph nodes	
	Any Breslow thickness, with ulceration	No nodes, but in-transit or satellite metastasis(es)	
Stage IV, M1a			Skin, subcutaneous or distant nodal disease
Stage IV, M1b			Lung metastases
Stage IV, M1c			All other sites or any other sites of metastases with raised lactate dehydrogenase

8.3 Cell and Tissue culture consumables

Table 8.7: List of cell and tissue culture consumables and their suppliers.

Material	Supplier
Trypsin	Sigma Aldrich, UK
Fetal calf serum (FCS)	Sigma Aldrich, UK
Dimethyl sulphoxide (DMSO)	Sigma Aldrich, UK
Dulbeccos modified eagle's medium (DMEM)	Biosera, UK
Ham's F12 medium	Labtech International, UK
Epidermal growth factor (EGF)	Sigma Aldrich, UK
Hydrocortisone	Sigma Aldrich, UK
Adenine	Sigma Aldrich, UK
Transferrin	Sigma Aldrich, UK
Insulin	Sigma Aldrich, UK
Glutamine	Sigma Aldrich, UK
Tri-iodothyramine	Sigma Aldrich, UK
Amphotericin B	Sigma Aldrich, UK
Penicillin/Streptomycin	Sigma Aldrich, UK
Cholera toxin	Sigma Aldrich, UK
Difco trypsin	Difco Labs, USA
Collagenase A	Sigma Aldrich, UK
Eagle's modified essnetial medium (EMEM)	Biosera, UK
Fungizone	Sigma Aldrich, UK
Calcium fluoride slides and windows	Crystran, UK
Magnesium fluoride slides	Crystran, UK
Quartz slides	UCG Optics, UK
Sapphire and Calcium fluoride cover slips	UCG Optics, UK

8.4 Tissue culture protocols

Table 8.8: Schedule for the Leica TP1020 tissue processor. 18 hours in total.

Step	Time
70% IMS (x2)	1 hour each
80% IMS	1.5 hour
85% IMS	1.5 hour
90% IMS	1.5 hour
95% IMS	1.5 hour
100%IMS (x2)	1.5 hour each
Xylene (x2)	1.5 hour each
Paraffin wax (x2)	2 hour each

Table 8.9: Schedule for H&E staining of wax and cryo embedded sections.

Step	Time
Wax embedded	
Xylene (x2)	3 min each
100% IMS	1 min
70% IMS	30 sec
Distilled water	1 min
Haematoxylin	1.5 min
Tap water	4 min
Eosin	5 min
Tap water (x2)	dunk each
70% IMS	dunk
100% IMS	30 sec
Xylene	dunk
Cryo embedded	
PBS (x10)	<30 sec
Haemotoxylin	1.5 min
Water rinse	4 min
Eosin	3 min
Water rinse (x2)	dunk
70% alcohol	dunk
90% alcohol	dunk

8.5 PCA of A375SM models

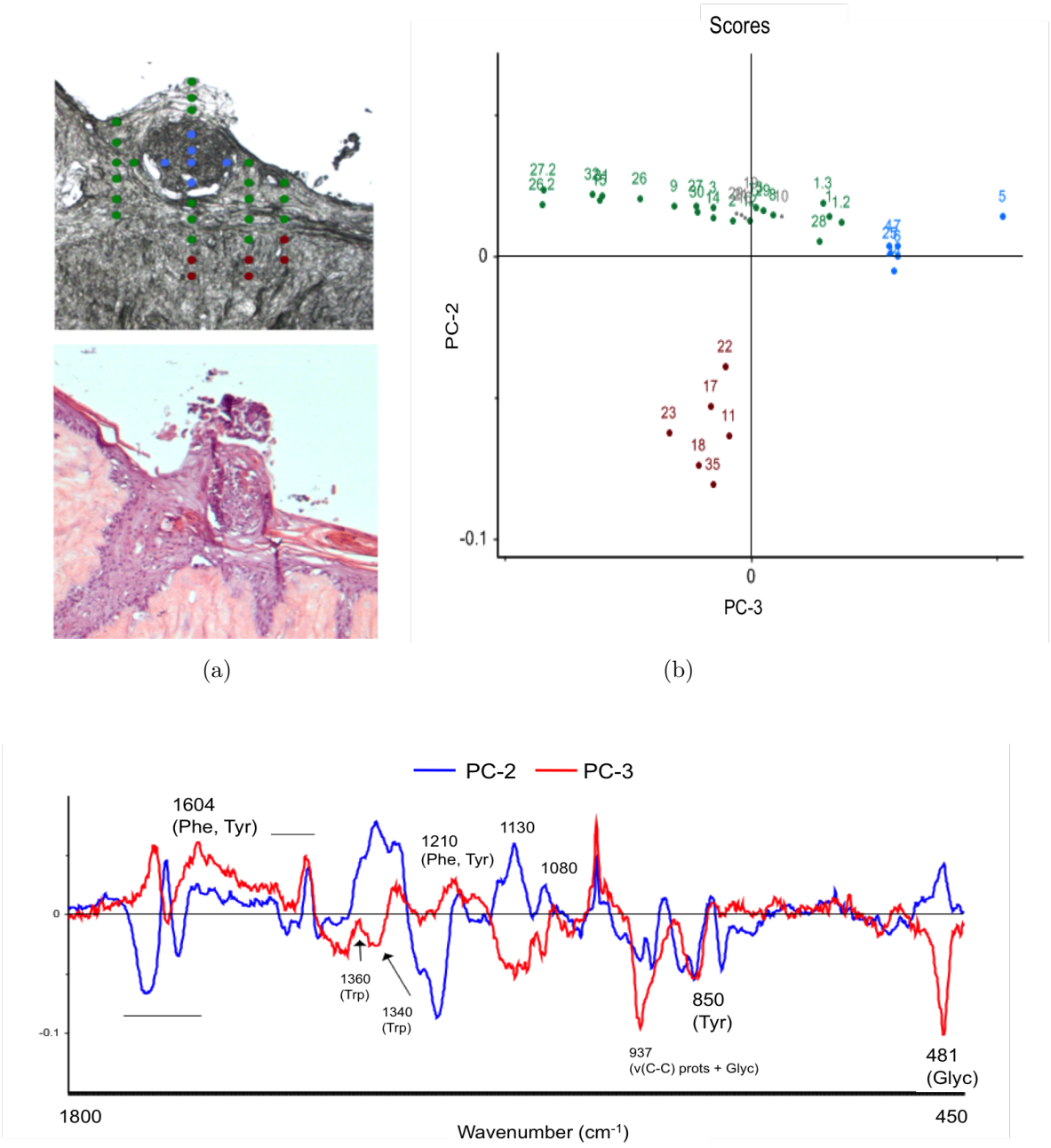

(a) (b)

(c)

Figure 8.3: PCA results for category 1 areas of A375SM models over the spectral range 1800-450 cm^{-1}. Spectral features associated with Phe, Trp, Tyr, Glyc, lipids and Amides are powering the separation between clustering and surrounding regions. Data points are colour coded: Blue=cluster, Green=surrounding tissue, Red=dermis (Chapter 6).

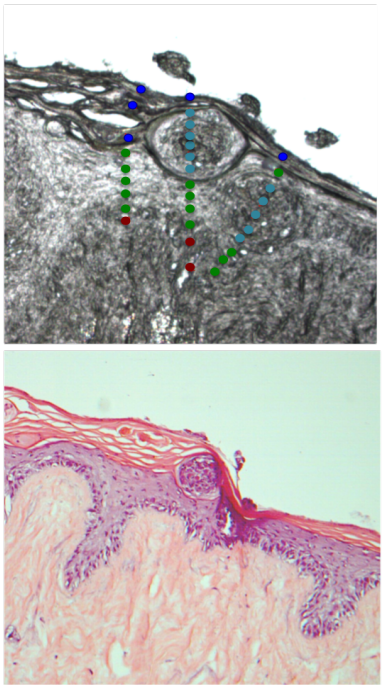

(a)

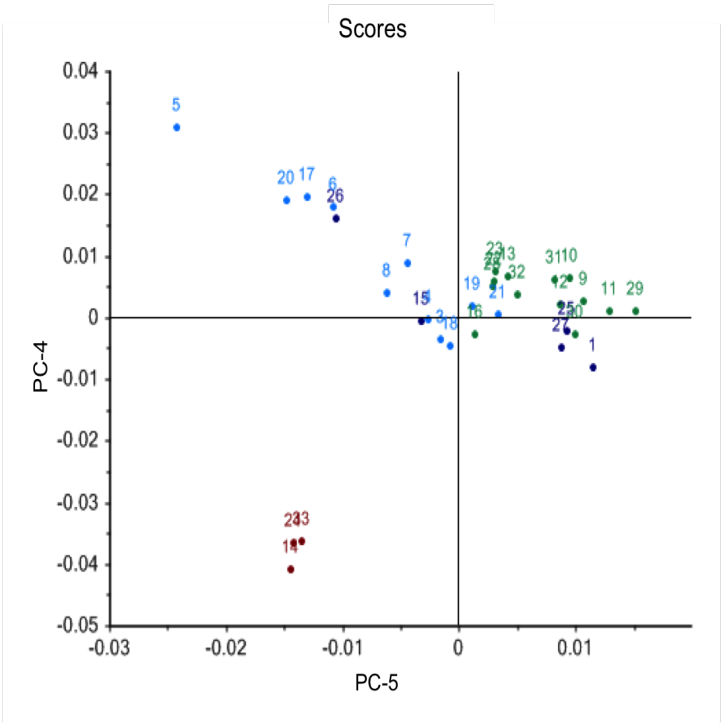

(b)

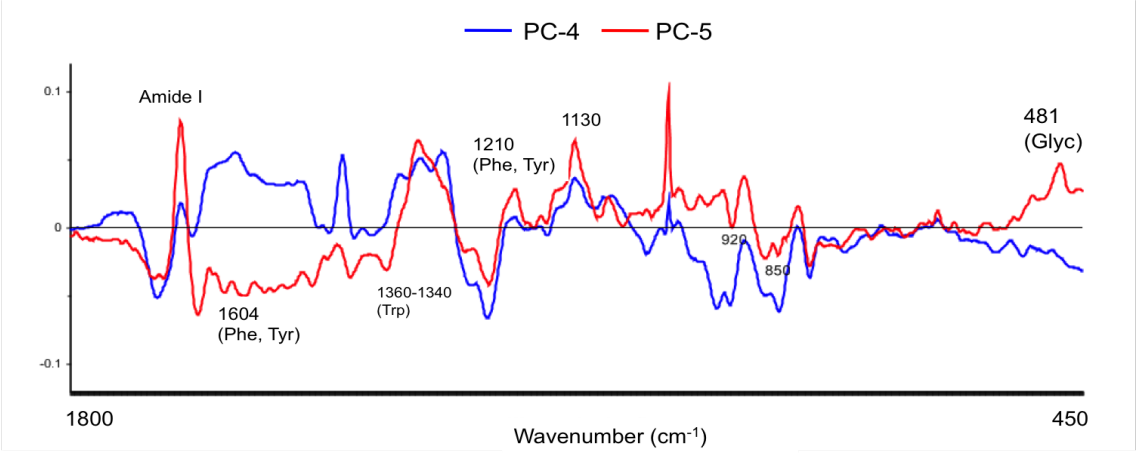

(c)

Figure 8.4: PCA results for category 1 areas of A375SM models over the spectral range 1800-450 cm^{-1}. Spectral features associated with the same areas as for Figure 8.3 are again powering separation between cluster and surrounding regions. Data collection points on the white light image are seen in (a). Data points in PCA correspond to Blue=cluster, Green=surrounding tissue, Red=dermis (Chapter 6).

8.6 PCA of C8161 models

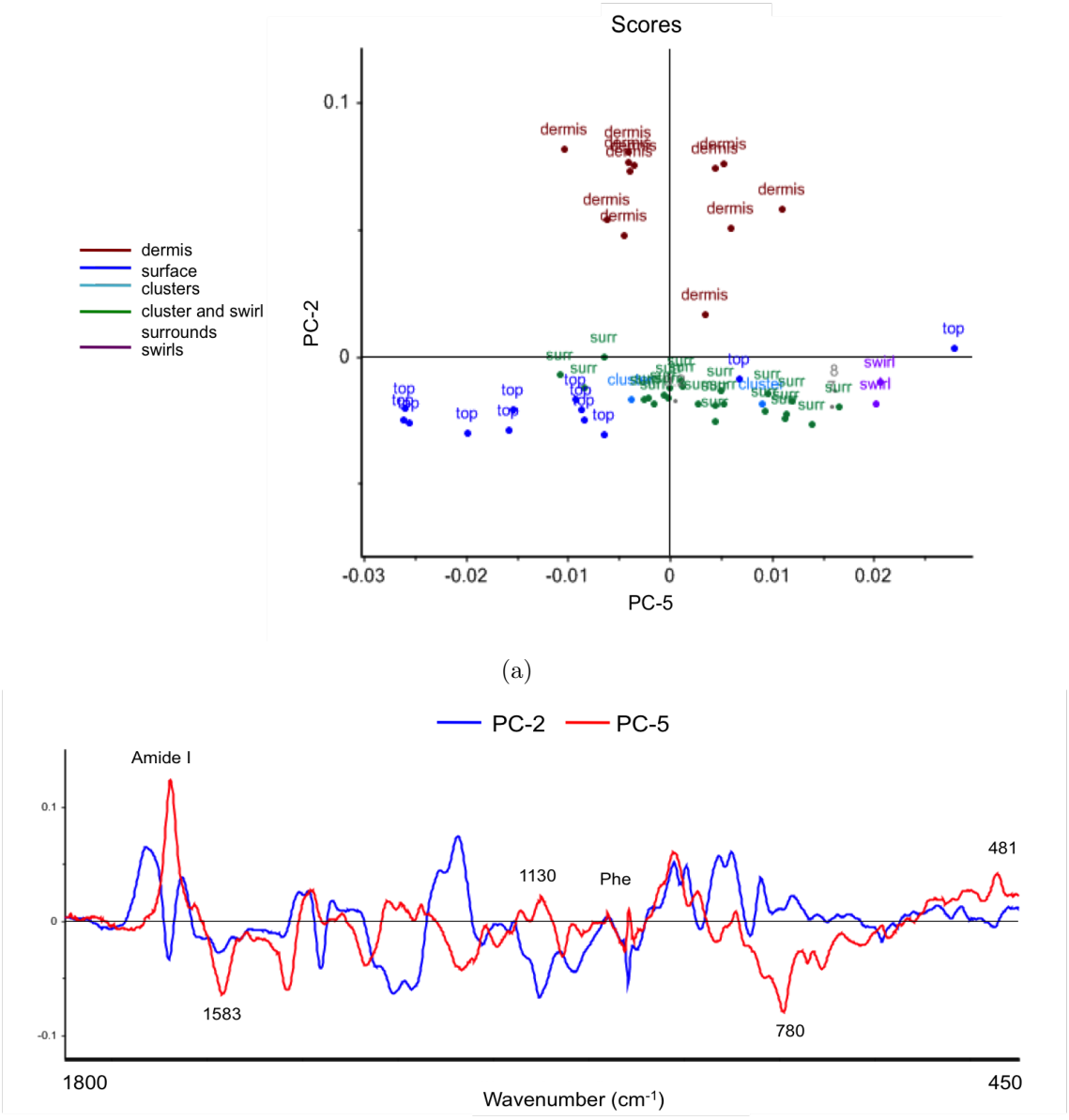

(a)

(b)

Figure 8.5: PCA results of C8161 models over various category areas and the range 1800-450 cm^{-1}. The scores plot contains spectra from two large sample areas. Loadings plot (b) corresponds to scores plot (a). Data points are labelled according to the sample area they were collected from. Blue=cluster, DarkBlue=surface, Green=surrounding tissue, Red=dermis. Features separating surface layers are discussed in Chapter 6.

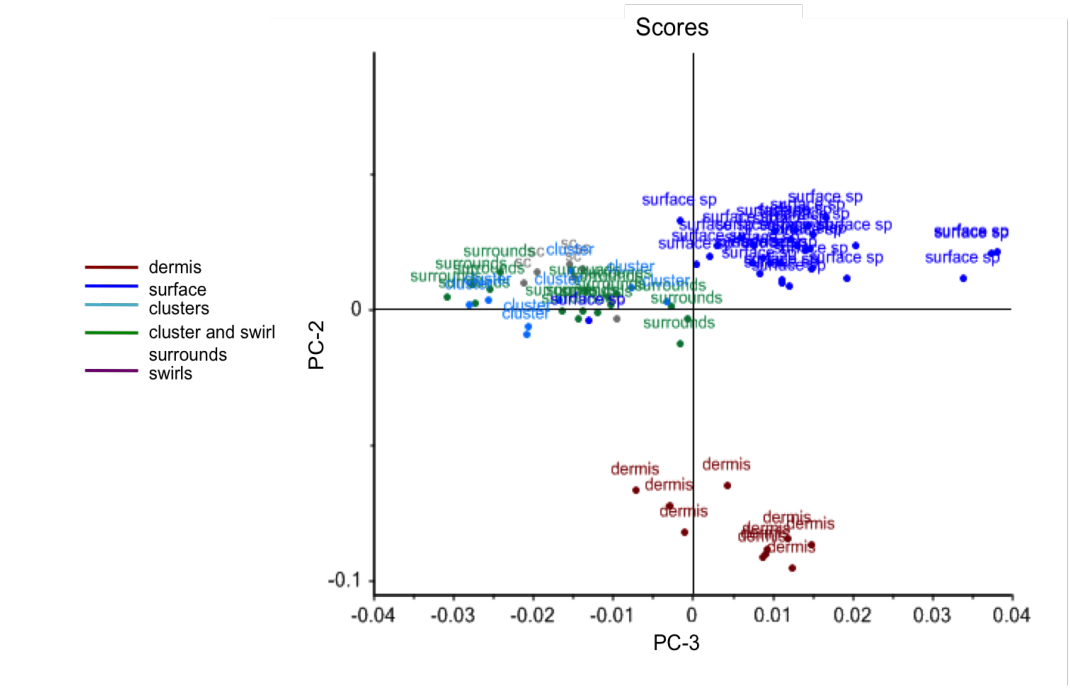

(a)

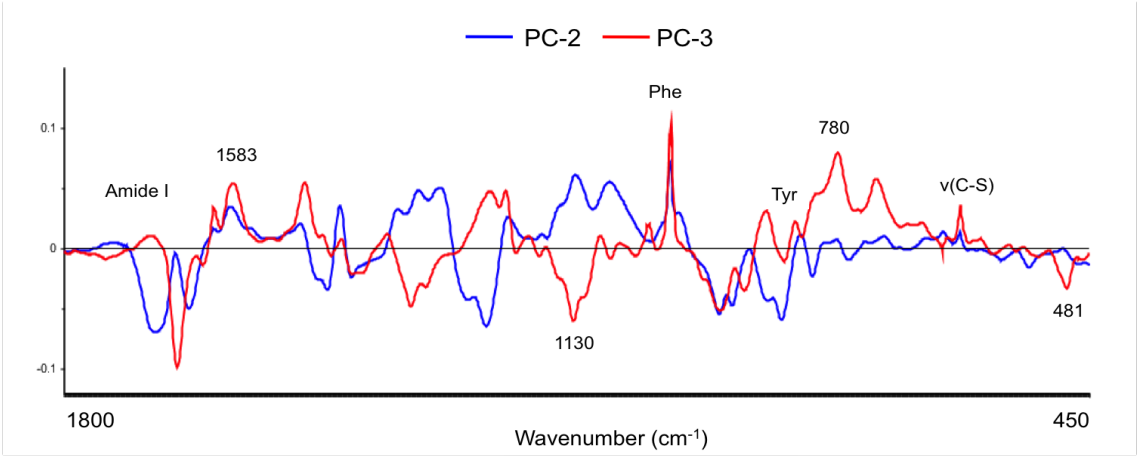

(b)

Figure 8.6: PCA results of C8161 models over various category areas and the range 1800-450 cm^{-1}. The scores plot contains spectra from two large sample areas. Loadings plot (b) corresponds to scores plot (a). Data points are labelled according to the sample area they were collected from. Blue=cluster, DarkBlue=surface, Green=surrounding tissue, Red=dermis. Features separating surface layers are discussed in Chapter 6.

8.7 List of Publications

Surface modification of Aramid fibres by graphene oxide nano sheets for multi scale polymer composites. *Surf Coat Technol* 2014, 258:458-466.
S Hussain, C Yorucu, I Ahmed, R Hussain, B Chen, MB Khan, NA Siddique, IU Rehman.

Quantitative determination of tolfenamic acid and its pharmaceutical formulation using FTIR and UV spectrometry. *C Eur J Chem* 2013, 11(9):1533-1541.
S Ahmed, MA Sheraz, C Yorucu, IU Rehman.

In vivo Raman analysis of HSEs in culture: observations on skin maturity. in preparation
C Yorucu, IU Rehman, S MacNeil.

Raman Spectroscopy detects melanoma and the tissue surrounding melanoma using tissue engineered melanoma models. submitted
C Yorucu, K Lau, S Mittar, NH Green, A Raza, IU Rehman, S MacNeil.

Raman spectroscopy can discriminate between normal, dysplastic and cancerous oral mucosa: a tissue-engineering approach. submitted
S Mian, M Ullah, C Yorucu, IU Rehman, H Colley.

Bibliography

Abu-Absi, Nicholas R et al. (2011). "Real time monitoring of multiple parameters in mammalian cell culture bioreactors using an in-line Raman spectroscopy probe". In: *Biotechnology and bioengineering* 108.5, pp. 1215–1221.

Alberts, Bruce et al. (2013). *Essential cell biology*. Garland Science.

Ali, SM et al. (2013a). "Raman spectroscopic mapping for the analysis of solar radiation induced skin damage". In: *Analyst* 138.14, pp. 3946–3956.

Ali, Syed M et al. (2013b). "Raman spectroscopic analysis of human skin tissue sections ex-vivo: evaluation of the effects of tissue processing and dewaxing". In: *Journal of biomedical optics* 18.6, pp. 061202–061202.

Ali, Syed Mehmood et al. (2013c). "A comparison of Raman, FTIR and ATR-FTIR micro spectroscopy for imaging human skin tissue sections". In: *Analytical Methods* 5.9, pp. 2281–2291.

Baek, Seong-Joon et al. (2006). "Detection of basal cell carcinoma by automatic classification of confocal raman spectra". In: *Computational Intelligence and Bioinformatics*. Springer, pp. 402–411.

Banks-Schlegel, Susan and Howard Green (1981). "Involucrin synthesis and tissue assembly by keratinocytes in natural and cultured human epithelia." In: *The Journal of cell biology* 90.3, pp. 732–737.

Barry, BW, HGM Edwards, and AC Williams (1992). "Fourier transform Raman and infrared vibrational study of human skin: assignment of spectral bands". In: *Journal of Raman Spectroscopy* 23.11, pp. 641–645.

Barth, Andreas and Christian Zscherp (2002). "What vibrations tell about proteins". In: *Quarterly reviews of biophysics* 35.04, pp. 369–430.

Bella, Jordi, Barbara Brodsky, and Helen M Berman (1995). "Hydration structure of a collagen peptide". In: *Structure* 3.9, pp. 893–906.

Belsey, Natalie A et al. (2014). "Evaluation of drug delivery to intact and porated skin by coherent Raman scattering and fluorescence microscopies". In: *Journal of Controlled Release* 174, pp. 37–42.

Berjot, M, J Marx, and AJP Alix (1987). "Determination of the secondary structure of proteins from the Raman amide I band: the reference intensity profiles method". In: *Journal of Raman spectroscopy* 18.4, pp. 289–300.

Bishnoi, Sandra W et al. (2006). "All-optical nanoscale pH meter". In: *Nano letters* 6.8, pp. 1687–1692.

Bishop, Julia Newton et al. (2007). "The prevention, diagnosis, referral and management of melanoma of the skin: concise guidelines". In: *Clinical medicine* 7.3, pp. 283–290.

Bissell, Mina J and Derek Radisky (2001). "Putting tumours in context". In: *Nature Reviews Cancer* 1.1, pp. 46–54.

Blank, Irvin H (1952). "Factors Which Influence the Water Content of the Stratum Corneum1". In: *Journal of Investigative Dermatology* 18.6, pp. 433–440.

Bodanese, Benito et al. (2012). "Discrimination of basal cell carcinoma and melanoma from normal skin biopsies in vitro through Raman spectroscopy and principal component analysis". In: *Photomedicine and laser surgery* 30.7, pp. 381–387.

Boelsma, Esther et al. (2000). "Characterization and comparison of reconstructed skin models: morphological and immunohistochemical evaluation". In: *Acta Dermatovenereologica - Stockholm* 80.2, pp. 82–88.

Bonnier, Franck et al. (2011). "In vitro analysis of immersed human tissues by Raman microspectroscopy". In: *Journal of Raman spectroscopy* 42.5, pp. 888–896.

Bonnier, Franck et al. (2012). "Analysis of human skin tissue by Raman microspectroscopy: dealing with the background". In: *Vibrational Spectroscopy* 61, pp. 124–132.

Bonnist, EYM et al. (2011a). "Measuring the penetration of a skin sensitizer and its delivery vehicles simultaneously with confocal Raman spectroscopy". In: *Skin pharmacology and physiology* 24.5, pp. 274–283.

Bonnist, EYM et al. (2011b). "Measuring the penetration of a skin sensitizer and its delivery vehicles simultaneously with confocal Raman spectroscopy". In: *Skin pharmacology and physiology* 24.5, p. 274.

Brancaleon, Lorenzo, Gloria Lin, and Nikiforos Kollias (1999). "The in vivo fluorescence of tryptophan moieties in human skin increases with UV exposure and is a marker for epidermal proliferation". In: *Journal of investigative dermatology* 113.6, pp. 977–982.

Broding, Horst Christoph et al. (2011). "In vivo Monitoring of epidermal absorption of hazardous substances by confocal Raman micro-spectroscopy". In: *JDDG: Journal der Deutschen Dermatologischen Gesellschaft* 9.8, pp. 618–627.

Broekaert, Sigrid et al. (2010). "Genetic and morphologic features for melanoma classification". In: *Pigment cell & melanoma research* 23.6, pp. 763–770.

Campesan, Susanna et al. (2011). "The kynurenine pathway modulates neurodegeneration in a Drosophila model of Huntington's disease". In: *Current Biology* 21.11, pp. 961–966.

CancerResearch (2011). *Cancer Research UK Skin Cancer Statistics*. http://www.cancerresearchuk.org/health-professional/cancer-statistics/statistics-by-cancer-type/skin-cancer/incidence#heading-Zero.

Carlson, Mark W et al. (2008). "Three-Dimensional Tissue Models of Normal and Diseased Skin". In: *Current Protocols in Cell Biology*, pp. 19–9.

Caspers, Peter J et al. (2001). "In vivo confocal Raman microspectroscopy of the skin: noninvasive determination of molecular concentration profiles". In: *Journal of Investigative Dermatology* 116.3, pp. 434–442.

Caspers, PJ, GW Lucassen, and GJ Puppels (2003). "Combined in vivo confocal Raman spectroscopy and confocal microscopy of human skin". In: *Biophysical journal* 85.1, pp. 572–580.

Caspers, PJ et al. (1998). "In vitro and in vivo Raman spectroscopy of human skin." In: *Biospectroscopy* 4, S31–9.

Cassileth, Barrie R et al. (1986). "How well do physicians recognize melanoma and other problem lesions?" In: *Journal of the American Academy of Dermatology* 14.4, pp. 555–560.

Caswell, Debra S and Thomas G Spiro (1986). "Ultraviolet resonance Raman spectroscopy of imidazole, histidine, and Cu (imidazole) 42+: implications for protein studies". In: *Journal of the American Chemical Society* 108.21, pp. 6470–6477.

Chauhan, Nishma et al. (2012). "How is the distal pocket of a heme protein optimized for binding of tryptophan?" In: *FEBS Journal* 279.24, pp. 4501–4509.

Chen, Suephy C et al. (2001). "A comparison of dermatologists' and primary care physicians' accuracy in diagnosing melanoma: a systematic review". In: *Archives of dermatology* 137.12, pp. 1627–1634.

Choi, Junghyun et al. (2005). "Direct observation of spectral differences between normal and basal cell carcinoma (BCC) tissues using confocal Raman microscopy". In: *Biopolymers* 77.5, pp. 264–272.

Chowdary, MVP et al. (2006). "Discrimination of normal, benign, and malignant breast tissues by Raman spectroscopy". In: *Biopolymers* 83.5, pp. 556–569.

Chrit, L et al. (2005). "In vivo chemical investigation of human skin using a confocal Raman fiber optic microprobe". In: *Journal of biomedical optics* 10.4, pp. 044007–044007.

Clark, Wallace H et al. (1989). "Model predicting survival in stage I melanoma based on tumor progression". In: *Journal of the National Cancer Institute* 81.24, pp. 1893–1904.

De Faria, DLA and MA De Souza (1999). "Raman spectra of human skin and nail excited in the visible region". In: *Journal of Raman spectroscopy* 30.3, pp. 169–171.

Dêbniak, Tadeusz (2004). "Familial malignant melanoma-overview." In: *Hereditary cancer in clinical practice* 2.3, pp. 123–129.

Devpura, Suneetha et al. (2012). "Diagnosis of head and neck squamous cell carcinoma using Raman spectroscopy: tongue tissues". In: *Journal of Raman Spectroscopy* 43.4, pp. 490–496.

Dickson, Paxton V and Jeffrey E Gershenwald (2011). "Staging and prognosis of cutaneous melanoma". In: *Surgical oncology clinics of North America* 20.1, pp. 1–17.

Downes, Andrew and Alistair Elfick (2010). "Raman spectroscopy and related techniques in biomedicine". In: *Sensors* 10.3, pp. 1871–1889.

Ebell, Mark (2008). "Clinical diagnosis of melanoma." In: *American family physician* 78.10, pp. 1205–1208.

Edge, Stephen B and Carolyn C Compton (2010). "The American Joint Committee on Cancer: the 7th edition of the AJCC cancer staging manual and the future of TNM". In: *Annals of surgical oncology* 17.6, pp. 1471–1474.

Edwards, HGM, AC Williams, and BW Barry (1995). "Potential applications of FT-Raman spectroscopy for dermatological diagnostics". In: *Journal of molecular structure* 347, pp. 379–387.

Elder, DE et al. (1983). "Invasive malignant melanomas lacking competence for metastasis." In: *The American Journal of dermatopathology* 6, pp. 55–61.

Engelhart, Karin et al. (2005). "In vitro reproduction of clinical hallmarks of eczematous dermatitis in organotypic skin models". In: *Archives of dermatological research* 297.1, pp. 1–9.

Ermakov, Igor V et al. (2005). "Resonance Raman detection of carotenoid antioxidants in living human tissue". In: *Journal of biomedical optics* 10.6, pp. 064028–064028.

Evans, Conor L et al. (2005). "Chemical imaging of tissue in vivo with video-rate coherent anti-Stokes Raman scattering microscopy". In: *Proceedings of the National Academy of Sciences of the United States of America* 102.46, pp. 16807–16812.

Eves, Paula et al. (2003). "Melanoma invasion in reconstructed human skin is influenced by skin cells–investigation of the role of proteolytic enzymes". In: *Clinical & experimental metastasis* 20.8, pp. 685–700.

Eves, Paula Clare (2001). "Human melanoma invasion and the antiinvasive and immunomodulatory role of α-melanocyte stimulating hormone (α-MSH)." PhD thesis. University of Sheffield.

Faoláin, Eoghan Ó et al. (2005). "Raman spectroscopic evaluation of efficacy of current paraffin wax section dewaxing agents". In: *Journal of Histochemistry & Cytochemistry* 53.1, pp. 121–129.

Farmer, Evan R, René Gonin, and Mark P Hanna (1996). "Discordance in the histopathologic diagnosis of melanoma and melanocytic nevi between expert pathologists". In: *Human pathology* 27.6, pp. 528–531.

Fendel, S and B Schrader (1998). "Investigation of skin and skin lesions by NIR-FT-Raman spectroscopy". In: *Fresenius' journal of analytical chemistry* 360.5, pp. 609–613.

Fernandez, Emmy M and Klaus F Helm (2004). "The diameter of melanomas". In: *Dermatologic surgery* 30.9, pp. 1219–1222.

Flach, Carol R and David J Moore (2013). "Infrared and Raman imaging spectroscopy of ex vivo skin". In: *International journal of cosmetic science* 35.2, pp. 125–135.

Förster, Matthias et al. (2011). "Ingredients tracking of cosmetic formulations in the skin: a confocal Raman microscopy investigation". In: *Pharmaceutical research* 28.4, pp. 858–872.

Förster, Matthias et al. (2012). "Confocal Raman microspectroscopy of the skin". In: *European Journal of Dermatology* 21.6, pp. 851–863.

Friedrich, Rossana B et al. (2015). "Skin penetration behavior of lipid-core nanocapsules for simultaneous delivery of resveratrol and curcumin". In: *European Journal of Pharmaceutical Sciences* 78, pp. 204–213.

Fullwood, Leanne M et al. (2014). "Effect of substrate choice and tissue type on tissue preparation for spectral histopathology by Raman microspectroscopy". In: *Analyst* 139.2, pp. 446–454.

Gaber, Bruce P and Warner L Peticolas (1977). "On the quantitative interpretation of biomembrane structure by Raman spectroscopy". In: *Biochimica et Biophysica Acta (BBA)-Biomembranes* 465.2, pp. 260–274.

Galli, Roberta et al. (2014). "Effects of tissue fixation on coherent anti-Stokes Raman scattering images of brain". In: *Journal of biomedical optics* 19.7, pp. 071402–071402.

Gandini, Sara et al. (2005a). "Meta-analysis of risk factors for cutaneous melanoma: I. Common and atypical naevi". In: *European Journal of Cancer* 41.1, pp. 28–44.

Gandini, Sara et al. (2005b). "Meta-analysis of risk factors for cutaneous melanoma: II. Sun exposure". In: *European Journal of Cancer* 41.1, pp. 45–60.

Gandini, Sara et al. (2005c). "Meta-analysis of risk factors for cutaneous melanoma: III. Family history, actinic damage and phenotypic factors". In: *European Journal of Cancer* 41.14, pp. 2040–2059.

Garlick, Jonathan A and Lorne B Taichman (1994). "Effect of TGF-β1 on re-epithelialization of human keratinocytes in vitro: an organotypic model". In: *Journal of investigative dermatology* 103.4, pp. 554–559.

Gasior-glogowska, MARLENA et al. (2010). "Structural alteration of collagen fibres–spectroscopic and mechanical studies". In: *strain* 19, p. 20.

Gawkrodger, David and Michael R Ardern-Jones (2012). *Dermatology: an illustrated colour text*. Elsevier Health Sciences.

Georgakoudi, Irene et al. (2008). "Optical spectroscopy and imaging for the noninvasive evaluation of engineered tissues". In: *Tissue Engineering Part B: Reviews* 14.4, pp. 321–340.

Gessner, R et al. (2004). "Identification of biotic and abiotic particles by using a combination of optical tweezers and in situ Raman spectroscopy". In: *ChemPhysChem* 5.8, pp. 1159–1170.

Gillies, Robert et al. (2000). "Fluorescence excitation spectroscopy provides information about human skin in vivo". In: *Journal of Investigative Dermatology* 115.4, pp. 704–707.

Globocan (2012). *The Globocan Project. Estimated cancer incidence, mortality and prevalence worlwide in 2012*. http://globocan.iarc.fr/Pages/fact_sheets_population.aspx.

Gniadecka, Monika et al. (1997). "Diagnosis of basal cell carcinoma by Raman spectroscopy". In: *Journal of Raman spectroscopy* 28.23, pp. 125–129.

Gniadecka, Monika et al. (1998). "Structure of water, proteins, and lipids in intact human skin, hair, and nail". In: *Journal of Investigative Dermatology* 110.4, pp. 393–398.

Gniadecka, Monika et al. (2004). "Melanoma diagnosis by Raman spectroscopy and neural networks: structure alterations in proteins and lipids in intact cancer tissue". In: *Journal of Investigative Dermatology* 122.2, pp. 443–449.

Harada, Issei, Takashi Miura, and Hideo Takeuchi (1986). "Origin of the doublet at 1360 and 1340 cm- 1 in the Raman spectra of tryptophan and related compounds". In: *Spectrochimica Acta Part A: Molecular Spectroscopy* 42.2, pp. 307–312.

Harmon, CS and PJ Phizackerley (1984). "Glycogen metabolism in psoriatic epidermis and in regenerating epidermis". In: *Clin Sci* 67.3, pp. 291–8.

Hata, Tissa R et al. (2000). "Non-invasive Raman spectroscopic detection of carotenoids in human skin". In: *Journal of Investigative Dermatology* 115.3, pp. 441–448.

Hoath, Steven B, Reiko Tanaka, and Steven T Boyce (1993). "Rate of stratum corneum formation in the perinatal rat". In: *Journal of investigative dermatology* 100.4, pp. 400–406.

Hoopes, John E and Michael JC Im (1974). "Glycogen metabolism in epidermal wound healing". In: *Journal of surgical oncology* 6.5, pp. 409–412.

Hsu, Mei-Yu et al. (1998). "Adenoviral gene transfer of $\beta 3$ integrin subunit induces conversion from radial to vertical growth phase in primary human melanoma". In: *The American journal of pathology* 153.5, pp. 1435–1442.

Huang, Sui, Ingemar Ernberg, and Stuart Kauffman (2009). "Cancer attractors: a systems view of tumors from a gene network dynamics and developmental perspective". In: *Seminars in cell & developmental biology*. Vol. 20. 7. Elsevier, pp. 869–876.

Hunter, Tony (1998). "The Croonian Lecture 1997. The phosphorylation of proteins on tyrosine: its role in cell growth and disease". In: *Philosophical Transactions of the Royal Society of London B: Biological Sciences* 353.1368, pp. 583–605.

Hüsing, Bärbel, Bernhard Bührlen, and Sibylle Gaisser (2003). *Human Tissue Engineered Products: Today's Markets and Future Prospects*. Fraunhofer Institute for Systems and Innovation Research Karlsruhe, Germany.

Integra (2009). *IntegraIntegra©Dermal Regeneration Template*. Available at http://www.integralife.com/products%2Fpdfs%2F634199956311907893_IDRT_Treatment_Guidelines_ER3341.pdf.

Jones, Teresa P, Patricia E Boiko, and Michael W Piepkorn (1996). "Skin biopsy indications in primary care practice: a population-based study". In: *The Journal of the American Board of Family Practice* 9.6, pp. 397–404.

Kämmer, Evelyn et al. (2014). "A new calibration concept for a reproducible quantitative detection based on SERS measurements in a microfluidic device demonstrated

on the model analyte adenine". In: *Physical Chemistry Chemical Physics* 16.19, pp. 9056–9063.

Kim, Jong-Ho et al. (2006). "Nanoparticle probes with surface enhanced Raman spectroscopic tags for cellular cancer targeting". In: *Analytical chemistry* 78.19, pp. 6967–6973.

Konorov, Stanislav O et al. (2011). "Absolute quantification of intracellular glycogen content in human embryonic stem cells with Raman microspectroscopy". In: *Analytical chemistry* 83.16, pp. 6254–6258.

Krafft, Christoph et al. (2005). "Identification of organelles and vesicles in single cells by Raman microspectroscopic mapping". In: *Vibrational spectroscopy* 38.1, pp. 85–93.

Kramers, Hendrik A and Werner Heisenberg (1925). "Über die Streuung von Strahlung durch Atome". In: *Zeitschrift für Physik A Hadrons and Nuclei* 31.1, pp. 681–708.

Kunz, Manfred (2014). "Oncogenes in melanoma: an update". In: *European journal of cell biology* 93.1, pp. 1–10.

Landsberg, Gr (1928). "Eine neue Erscheinung bei der Lichtzerstreuung in Krystallen". In: *Naturwissenschaften* 16, p. 558.

Larraona-Puy, Marta et al. (2009). "Development of Raman microspectroscopy for automated detection and imaging of basal cell carcinoma". In: *Journal of biomedical optics* 14.5, pp. 054031–054031.

Larson, Allison R, Eliz Konat, and Rhoda M Alani (2009). "Melanoma biomarkers: current status and vision for the future". In: *Nature Clinical Practice Oncology* 6.2, pp. 105–117.

LeBleu, Valerie S, Brian MacDonald, and Raghu Kalluri (2007). "Structure and function of basement membranes". In: *Experimental biology and medicine* 232.9, pp. 1121–1129.

LeBoit, Philip E et al. (2006). *World Health Organization Classification of Tumours. Pathology and genetics of skin tumours*. Lyon: IARC.

Li, Boyan et al. (2010). "Rapid characterization and quality control of complex cell culture media solutions using Raman spectroscopy and chemometrics". In: *Biotechnology and bioengineering* 107.2, pp. 290–301.

Li, Mengqiu et al. (2012). "Single cell Raman spectroscopy for cell sorting and imaging". In: *Current opinion in biotechnology* 23.1, pp. 56–63.

Lieber, Chad A, Hubert E Nethercott, and Mustafa H Kabeer (2010). "Cancer field effects in normal tissues revealed by Raman spectroscopy". In: *Biomedical optics express* 1.3, pp. 975–982.

Lieber, Chad A et al. (2008a). "In vivo nonmelanoma skin cancer diagnosis using Raman microspectroscopy". In: *Lasers in surgery and medicine* 40.7, pp. 461–467.

Lieber, Chad A et al. (2008b). "Raman microspectroscopy for skin cancer detection in vitro". In: *Journal of biomedical optics* 13.2, pp. 024013–024013.

Lobitz, WC et al. (1962). "Glycogen response in human epidermal basal cell". In: *Archives of dermatology* 86.2, pp. 207–211.

Longo, Caterina et al. (2011). "De novo melanoma and melanoma arising from pre-existing nevus: in vivo morphologic differences as evaluated by confocal microscopy". In: *Journal of the American Academy of Dermatology* 65.3, pp. 604–614.

Lorincz, Attila et al. (2004). "Raman spectroscopy for neoplastic tissue differentiation: a pilot study". In: *Journal of pediatric surgery* 39.6, pp. 953–956.

Lui, Harvey et al. (2012). "Real-time Raman spectroscopy for in vivo skin cancer diagnosis". In: *Cancer research* 72.10, pp. 2491–2500.

MacNeil, Sheila (2007). "Progress and opportunities for tissue-engineered skin". In: *Nature* 445.7130, pp. 874–880.

Mansbridge, Jonathan N and Merrill Knapp (1987). "Changes in keratinocyte maturation during wound healing". In: *Journal of Investigative Dermatology* 89.3, pp. 253–263.

Mansfield, Jessica et al. (2013). "Chemically specific imaging and in-situ chemical analysis of articular cartilage with stimulated Raman scattering". In: *Journal of biophotonics* 6.10, pp. 803–814.

Marsden, JR et al. (2010). "Revised UK guidelines for the management of cutaneous melanoma 2010". In: *British Journal of Dermatology* 163.2, pp. 238–256.

Martin, Airton A et al. (2004). "Principal components analysis of FT-Raman spectra of ex vivo basal cell carcinoma". In: *Biomedical Optics 2004*. International Society for Optics and Photonics, pp. 198–204.

Massi, Guido and Philip E LeBoit (2013). *Histological diagnosis of nevi and melanoma*. Springer Science & Business Media.

McCarthy, Stanley W and Richard A Scolyer (2010). "Pitfalls and important issues in the pathologic diagnosis of melanocytic tumors". In: *The Ochsner Journal* 10.2, pp. 66–74.

McCreery, Richard L (2005). *Raman spectroscopy for chemical analysis*. Vol. 225. John Wiley & Sons.

McGovern, Thomas W and Mark S Litaker (1992). "Clinical predictors of malignant pigmented lesions". In: *The Journal of dermatologic surgery and oncology* 18.1, pp. 22–26.

Metcalfe, Anthony D and Mark WJ Ferguson (2007). "Tissue engineering of replacement skin: the crossroads of biomaterials, wound healing, embryonic development, stem cells and regeneration". In: *Journal of the Royal Society Interface* 4.14, pp. 413–437.

Mian, Salman Aziz (2015). "Raman spectroscopic analysis of normal, abnormal and irradiated oral mucosa: A tissue engineered and ex vivo approach". PhD thesis. University of Sheffield.

Miura, Takashi, Hideo Takeuchi, and Issei Harada (1989). "Tryptophan Raman bands sensitive to hydrogen bonding and side-chain conformation". In: *Journal of Raman spectroscopy* 20.10, pp. 667–671.

Moffett, John R and MA ARYAN Namboodiri (2003). "Tryptophan and the immune response". In: *Immunology and cell biology* 81.4, pp. 247–265.

Moretto, Justin et al. (2011). "Raman-Process Raman Spectroscopy for In-Line CHO Cell Culture Monitoring". In: *American Pharmaceutical Review* 14.3, p. 18.

Myshakina, Nataliya S, Zeeshan Ahmed, and Sanford A Asher (2008). "Dependence of amide vibrations on hydrogen bonding". In: *The Journal of Physical Chemistry B* 112.38, pp. 11873–11877.

Nagar, Bhushan (2007). "c-Abl tyrosine kinase and inhibition by the cancer drug imatinib (Gleevec/STI-571)". In: *The Journal of nutrition* 137.6, 1518S–1523S.

Nakagawa, Noriaki, Masayuki Matsumoto, and Shingo Sakai (2010). "In vivo measurement of the water content in the dermis by confocal Raman spectroscopy". In: *Skin Research and Technology* 16.2, pp. 137–141.

Netzlaff, Frank et al. (2005). "The human epidermis models EpiSkin®, SkinEthic® and EpiDerm®: an evaluation of morphology and their suitability for testing phototoxicity, irritancy, corrosivity, and substance transport". In: *European Journal of Pharmaceutics and Biopharmaceutics* 60.2, pp. 167–178.

Neubert, Reinhard et al. (1997). "Structure of stratum corneum lipids characterized by FT-Raman spectroscopy and DSC. II. Mixtures of ceramides and saturated fatty acids". In: *Chemistry and physics of lipids* 89.1, pp. 3–14.

Nguyen, TT et al. (2012). "Characterization of type I and IV collagens by Raman microspectroscopy: Identification of spectral markers of the dermo-epidermal junction". In: *Journal of Spectroscopy* 27.5-6, pp. 421–427.

Nijssen, Annieke et al. (2002). "Discriminating basal cell carcinoma from its surrounding tissue by Raman spectroscopy". In: *Journal of Investigative Dermatology* 119.1, pp. 64–69.

Nijssen, Annieke et al. (2007). "Discriminating basal cell carcinoma from perilesional skin using high wave-number Raman spectroscopy". In: *Journal of biomedical optics* 12.3, pp. 034004–034004.

Nolte, CJM et al. (1993). "Development of a stratum corneum and barrier function in an organotypic skin culture". In: *Archives of dermatological research* 285.8, pp. 466–474.

Notingher, I et al. (2002). "In situ characterisation of living cells by Raman spectroscopy". In: *Journal of Spectroscopy* 16.2, pp. 43–51.

O'Regan, Gráinne M et al. (2010). "Raman profiles of the stratum corneum define 3 filaggrin genotype–determined atopic dermatitis endophenotypes". In: *Journal of Allergy and Clinical Immunology* 126.3, pp. 574–580.

Ortonne, J-P (2002). "Photoprotective properties of skin melanin". In: *British Journal of Dermatology* 146.s61, pp. 7–10.

Owen, Chris A et al. (2006). "In vitro toxicology evaluation of pharmaceuticals using Raman micro-spectroscopy". In: *Journal of cellular biochemistry* 99.1, pp. 178–186.

Pascut, Flavius C et al. (2013). "Non-invasive label-free monitoring the cardiac differentiation of human embryonic stem cells in-vitro by Raman spectroscopy". In: *Biochimica et Biophysica Acta (BBA)-General Subjects* 1830.6, pp. 3517–3524.

Percot, Aline and Michel Lafleur (2001). "Direct observation of domains in model stratum corneum lipid mixtures by Raman microspectroscopy". In: *Biophysical journal* 81.4, pp. 2144–2153.

Pereira, Riziene d MF et al. (2004). "Diagnosis of squamous cell carcinoma of human skin by Raman spectroscopy". In: *Biomedical Optics 2004*. International Society for Optics and Photonics, pp. 106–112.

Philipsen, PA et al. (2013). "Diagnosis of malignant melanoma and basal cell carcinoma by in vivo NIR-FT Raman spectroscopy is independent of skin pigmentation". In: *Photochemical & Photobiological Sciences* 12.5, pp. 770–776.

Ponec, Maria et al. (1997). "The formation of competent barrier lipids in reconstructed human epidermis requires the presence of vitamin C". In: *Journal of investigative dermatology* 109.3, pp. 348–355.

Pudlas, Marieke et al. (2011). "Raman spectroscopy: a noninvasive analysis tool for the discrimination of human skin cells". In: *Tissue Engineering Part C: Methods* 17.10, pp. 1027–1040.

Qian, Weili, Noemi G Mirkin, and Samuel Krimm (1999). "A spectroscopically effective molecular mechanics model for the intermolecular interactions of the hydrogen-

bonded N-methylacetamide dimer". In: *Chemical Physics Letters* 315.1, pp. 125–129.

Rajaram, Narasimhan et al. (2010). "Pilot clinical study for quantitative spectral diagnosis of non-melanoma skin cancer". In: *Lasers in surgery and medicine* 42.10, pp. 876–887.

Raman, Chandrasekhara Venkata (1928). "A new radiation". In: *Indian Journal of physics* 2, pp. 387–398.

Rigel, Darrell S, Julie Russak, and Robert Friedman (2010). "The evolution of melanoma diagnosis: 25 years beyond the ABCDs". In: *CA: a cancer journal for clinicians* 60.5, pp. 301–316.

Rowe, DAN E, RAYMOND J Carroll, and CALVIN L Day (1989). "Long-term recurrence rates in previously untreated (primary) basal cell carcinoma: implications for patient follow-up". In: *The Journal of dermatologic surgery and oncology* 15.3, pp. 315–328.

Ruddick, Jon P et al. (2006). "Tryptophan metabolism in the central nervous system: medical implications". In: *Expert reviews in molecular medicine* 8.20, pp. 1–27.

Saar, Brian G et al. (2010). "Video-rate molecular imaging in vivo with stimulated Raman scattering". In: *Science* 330.6009, pp. 1368–1370.

Sarna, Tadeusz and Harold A Swartz (1988). "The physical properties of melanins". In: *The Pigmentary System: Physiology and Pathophysiology, Second Edition*, pp. 311–341.

Schallreuter, Karin U et al. (1996). "Oxybenzone oxidation following solar irradiation of skin: photoprotection versus antioxidant inactivation". In: *Journal of investigative dermatology* 106.3, pp. 583–586.

Schröcksnadel, Katharina et al. (2006). "Monitoring tryptophan metabolism in chronic immune activation". In: *Clinica Chimica Acta* 364.1, pp. 82–90.

Shim, Martin G and Brian C Wilson (1996). "The Effects of ex vivo Handling Procedures on the Near-Infrared Raman Spectra of Normal Mammalian Tissues". In: *Photochemistry and photobiology* 63.5, pp. 662–671.

Shimanouchi, Takehiko (1972). *Tables of Molecular Vibrational Frequencies Consolidated. Volume I.* Tech. rep. DTIC Document.

Siamwiza, Mwindaace N et al. (1975). "Interpretation of the doublet at 850 and 830 cm-1 in the Raman spectra of tyrosyl residues in proteins and certain model compounds". In: *Biochemistry* 14.22, pp. 4870–4876.

Silva, CL et al. (2006). "Study of human stratum corneum and extracted lipids by thermomicroscopy and DSC". In: *Chemistry and physics of lipids* 140.1, pp. 36–47.

Silveira, Landulfo et al. (2012). "Discriminating model for diagnosis of basal cell carcinoma and melanoma in vitro based on the Raman spectra of selected biochemicals". In: *Journal of biomedical optics* 17.7, pp. 077003–077003.

Smekal, Adolf (1923). "Zur quantentheorie der dispersion". In: *Naturwissenschaften* 11.43, pp. 873–875.

Stewart, Bernard W, Paul Kleihues, International Agency for Research on Cancer, et al. (2003). *World cancer report*. Vol. 57. IARC press Lyon.

Straseski, Joely A et al. (2009). "Oxygen deprivation inhibits basal keratinocyte proliferation in a model of human skin and induces regio-specific changes in the distribution of epidermal adherens junction proteins, aquaporin-3, and glycogen". In: *Wound repair and regeneration* 17.4, pp. 606–616.

StrataTech (2014). *StrataGraft skin tissue*. Available at http://stratatechcorp.com/products/index.php.

Swain, RJ and MM Stevens (2007). "Raman microspectroscopy for non-invasive biochemical analysis of single cells". In: *Biochemical Society Transactions* 35.3, pp. 544–550.

Sweeney, Joyce A and Sanford A Asher (1990). "Tryptophan UV resonance Raman excitation profiles". In: *Journal of Physical Chemistry* 94.12, pp. 4784–4791.

Tadaki, Douglas K and SK Niyogi (1993). "The functional importance of hydrophobicity of the tyrosine at position 13 of human epidermal growth factor in receptor binding." In: *Journal of Biological Chemistry* 268.14, pp. 10114–10119.

Takeuchi, Hideo (2003). "Raman structural markers of tryptophan and histidine side chains in proteins". In: *Biopolymers* 72.5, pp. 305–317.

Talari, Abdullah Chandra Sekhar et al. (2015). "Raman Spectroscopy of Biological Tissues". In: *Applied Spectroscopy Reviews* 50.1, pp. 46–111.

Teh, SK et al. (2008). "Diagnostic potential of near-infrared Raman spectroscopy in the stomach: differentiating dysplasia from normal tissue". In: *British journal of cancer* 98.2, pp. 457–465.

Tfaili, Sana et al. (2012). "Shedding light on the laser wavelength effect in Raman analysis of skin epidermises". In: *Analyst* 137.18, pp. 4241–4246.

Tfayli, A, O Piot, and M Manfait (2008). "Confocal Raman microspectroscopy on excised human skin: uncertainties in depth profiling and mathematical correction applied to dermatological drug permeation". In: *Journal of biophotonics* 1.2, pp. 140–153.

Tfayli, Ali et al. (2012). "Molecular interactions of penetration enhancers within ceramides organization: a Raman spectroscopy approach". In: *Analyst* 137.21, pp. 5002–5010.

Tfayli, Ali et al. (2013). "Hydration effects on the barrier function of stratum corneum lipids: Raman analysis of ceramides 2, III and 5". In: *Analyst* 138.21, pp. 6582–6588.

Thackray, Sarah J, Christopher G Mowat, and Stephen K Chapman (2008). "Transition Metals in Biochemistry: Exploring the mechanism of tryptophan 2, 3-dioxygenase". In: *Biochemical Society Transactions* 36.Pt 6, p. 1120.

Thakoersing, Varsha S et al. (2011). "Unraveling barrier properties of three different in-house human skin equivalents". In: *Tissue Engineering Part C: Methods* 18.1, pp. 1–11.

Tlsty, Thea D and Lisa M Coussens (2006). "Tumor stroma and regulation of cancer development". In: *Annu. Rev. Pathol. Mech. Dis.* 1, pp. 119–150.

Torkian, Behrooz A et al. (2004). "Modeling aberrant wound healing using tissue-engineered skin constructs and multiphoton microscopy". In: *Archives of facial plastic surgery* 6.3, pp. 180–187.

Tosato, Maira G et al. (2012). "Raman spectroscopic investigation of the effects of cosmetic formulations on the constituents and properties of human skin". In: *Photomedicine and laser surgery* 30.2, pp. 85–91.

Ubersax, Jeffrey A and James E Ferrell Jr (2007). "Mechanisms of specificity in protein phosphorylation". In: *Nature reviews Molecular cell biology* 8.7, pp. 530–541.

Uribe, Pablo, Ignacio I Wistuba, and Sergio González (2003). "BRAF mutation: a frequent event in benign, atypical, and malignant melanocytic lesions of the skin". In: *The American journal of dermatopathology* 25.5, pp. 365–370.

Urso, Carmelo et al. (2008). "Sensitivity and specificity of histological criteria in the diagnosis of conventional cutaneous melanoma". In: *Melanoma research* 18.4, pp. 253–258.

Uzunbajakava, N et al. (2003). "Nonresonant confocal Raman imaging of DNA and protein distribution in apoptotic cells". In: *Biophysical journal* 84.6, pp. 3968–3981.

Väisänen, Anne et al. (1998). "Prognostic value of MMP-2 immunoreactive protein (72 kD type IV collagenase) in primary skin melanoma". In: *The Journal of pathology* 186.1, pp. 51–58.

Verma, Surendra P and Donald FH Wallach (1977). "Raman spectra of some saturated, unsaturated and deuterated C 18 fatty acids in the HCH-deformation and CH-stretching regions". In: *Biochimica et Biophysica Acta (BBA)-Lipids and Lipid Metabolism* 486.2, pp. 217–227.

Wagner, Jeffrey D et al. (2003). "Patterns of initial recurrence and prognosis after sentinel lymph node biopsy and selective lymphadenectomy for melanoma." In: *Plastic and reconstructive surgery* 112.2, pp. 486–497.

Walsh, Scott TR et al. (2003). "The hydration of amides in helices; a comprehensive picture from molecular dynamics, IR, and NMR". In: *Protein Science* 12.3, pp. 520–531.

Wang, Zhuyuan et al. (2008). "Biological pH sensing based on surface enhanced Raman scattering through a 2-aminothiophenol-silver probe". In: *Biosensors and Bioelectronics* 23.6, pp. 886–891.

Ward, Kevin R et al. (2007). "Oxygenation monitoring of tissue vasculature by resonance Raman spectroscopy". In: *Analytical chemistry* 79.4, pp. 1514–1518.

Weatherhead, SC, M Haniffa, and CM Lawrence (2007). "Melanomas arising from naevi and de novo melanomasdoes origin matter?" In: *British Journal of Dermatology* 156.1, pp. 72–76.

Wegener, Matthias et al. (1996). "Structure of stratum corneum lipids characterized by FT-Raman spectroscopy and DSC. I. ceramides". In: *International journal of pharmaceutics* 128.1, pp. 203–213.

— (1997). "Structure of stratum corneum lipids characterized by FT-Raman spectroscopy and DSC. III. Mixtures of ceramides and cholesterol". In: *Chemistry and physics of lipids* 88.1, pp. 73–82.

Wolf, IH et al. (1998). "Sensitivity in the clinical diagnosis of malignant melanoma." In: *Melanoma research* 8.5, pp. 425–429.

Wood, Bayden R et al. (2008). "Shedding new light on the molecular architecture of oocytes using a combination of synchrotron Fourier transform-infrared and Raman spectroscopic mapping". In: *Analytical chemistry* 80.23, pp. 9065–9072.

Yee, Vivian SK et al. (2005). "Outcome in 846 cutaneous melanoma patients from a single center after a negative sentinel node biopsy". In: *Annals of surgical oncology* 12.6, pp. 429–439.

Yu, Guo et al. (2013). "Vibrational spectroscopy and microscopic imaging: novel approaches for comparing barrier physical properties in native and human skin equivalents". In: *Journal of biomedical optics* 18.6, pp. 061207–061207.

Zhang, Zheng and Bozena B Michniak-Kohn (2012). "Tissue engineered human skin equivalents". In: *Pharmaceutics* 4.1, pp. 26–41.

Zhao, Jianhua et al. (2008). "Real-time Raman spectroscopy for non-invasive skin cancer detection-preliminary results". In: *Engineering in Medicine and Biology Soci-*

ety, 2008. EMBS 2008. 30th Annual International Conference of the IEEE. IEEE, pp. 3107–3109.